DEUTSCHES ELEKTRONEN-SYNCHROTRON
Ein Forschungszentrum der Helmholtz-Gemeinschaft

DESY-THESIS-2017-038
September 2017

Measurement of the Total and Differential b Cross Sections at HERA and CMS Tracker Alignment at LHC

by

Nazar Stefaniuk

ISSN 1435-8085

NOTKESTRASSE 85 - 22607 HAMBURG

To be sure that your reports and preprints are promptly included in the HEP literature database
send them to (if possible by air mail):

DESY
Zentralbibliothek
Notkestraße 85
22607 Hamburg
Germany

DESY
Bibliothek
Platanenallee 6
15738 Zeuthen
Germany

Measurement of the total and differential b cross sections at HERA and CMS tracker alignment at LHC

Dissertation

zur Erlangung des Doktorgrades
an der Fakultät für
Mathematik, Informatik und Naturwissenschaften
Fachbereich Physik
der Universität Hamburg

vorgelegt von

Nazar Stefaniuk

aus Iv.-Frankivsk/Kiew (Ukraine)

Hamburg , 2017

Gutachter in/der Dissertation:	PD Dr. Achim Geiser Prof. Dr. Elisabetta Gallo
Mitglieder der Prüfungskommission:	PD Dr. Achim Geiser Prof. Dr. Elisabetta Gallo Prof. Dr. Caren Hagner Prof. Dr. Gudrid Moortgat-Pick Dr. Katarzyna Wichmann
Tag der Disputation:	08 May 2017
Vorsitzender des Prüfungskommission:	Prof. Dr. Caren Hagner
Vorsitzender des Promotionsausschusses:	Prof. Dr. Wolfgang Hansen
Dekan des MIN-Fakultät:	Prof. Dr. Heinrich Graener

Abstract

This thesis is logically divided into two main parts. The first part present a ZEUS analysis which was performed on the data obtained from electron-proton collisions measured by the ZEUS detector for the 2003-2007 running period. The full HERA-II integrated luminosity of 376 pb^{-1} is used. The ZEUS detector is sensitive to the full phase space of beauty production, since it has cylindrical geometry, covers a wide rapidity range and was able to measure low transverse momentum muons. In this part a measurement of beauty production was studied via the process $ep \to e'b\bar{b}X \to e'\mu\mu X$. Making full use of the HERA-II detector upgrade, secondary vertex information was used to constrain the beauty and charm contribution to this process. The result of this analysis is the measurement of the total, visible and differential cross sections for beauty production. The cross sections are compared to next-to-leading order QCD calculations.

Similar to the beauty events, instanton or instanton-induced events involving heavy flavour can also be a source for non-isolated, both like- and unlike-sign muon pairs. In this analysis, instantons were studied with using QCDINS predictions. The data show no indication for instanton-induced events.

The second part is related to CMS tracker alignment. It uses collision and cosmic data samples obtained by the CMS detector at the Large Hadron Collider in 2012. This part consists of studies of the CMS tracker alignment weak modes and a detailed study of the "z-rescaling" weak mode. The CMS tracker alignment weak mode study includes the simulation of the weak modes, and the alignment implementation on top of such simulation. This study shows that the alignment procedure of the CMS tracker is stable with regard to the three weak modes: "Twist, Sagitta and Telescope" which stand for three types of systematic shifts of the CMS tracker. The "z-rescaling" weak mode shows a strong and unexpected shift of some tracker detector components in the z direction. To study the issue, a significant number of tests such as "high level structure" alignment only, alignment with fixed end caps, impact of the p_T dependence of the tracks on the alignment procedure, the simulation of cosmic data as collision data, introducing TID , TEC end cap disk constraints and other important tests were performed. Even though this issue was not yet fully solved, the studies performed in this thesis show consistent and detailed steps that help to better understand the issue and solve it in the future.

The track helix parametrisation of both the ZEUS and CMS experiments was studied. A checked, detailed description of such parametrisation as well as its transformation from the CMS format into the ZEUS format is performed. In addition, a CMS physics analyses of $B \to J/\psi K$ decays was started. These studies were performed with the CMS "open data" for the 2010 time period. Logically this can be seen as a first step towards a measurement of the total beauty cross section in CMS in the same spirit as the one performed with the ZEUS data.

Kurzfassung

Die Doktorarbeit ist in zwei inhaltlich getrennte Bereiche gegliedert. Im Ersten werden Analysen von ZEUS Daten präsentiert. Die Daten stammen von Elektron-Proton-Kollisionsmessungen, die mit dem ZEUS Detektor in den Jahren 2003 bis 2007 aufgenommen wurden. Es wurde die volle integrierte Luminosität von HERA-II von 376 pb^{-1} verwendet. Der ZEUS-Detektor ist sensitiv auf die Entstehung von Beauty-Endzuständen, da der Detektor eine zylindrische Geometrie besitzt und in der Lage war, Myonen mit geringen transversalen Impulsen nachzuweisen. In diesem Teil der Arbeit werden Messungen der Beauty-Produktion anhand des Prozesses $ep \to e'bbX \to e'\mu\mu X$ untersucht. Dank des HERA-II Detektor-Upgrades konnten Sekundärvertex-Informationen genutzt werden, um die Beauty- und Charm-Anteile des Prozesses eindeutig identifizieren zu können. Durch die Analyse war es möglich, den totalen, sichtbaren und differentiellen Wirkungsquerschnitt für die Beauty-Produktion in diesem Prozess aus den Daten zu extrahieren. Die Wirkungsquerschnitte werden mit QCD-Rechnungen in nächstführender Ordnung verglichen.

Neben den Beauty-Ereignissen können auch Instanton-Ereignisse oder durch Instantonen ausgelöste Ereignisse mit Schweren Quarks ursächlich für nicht isolierte Myon-Paare mit gleichem oder ungleichem Vorzeichen sein. Die hier gezeigte Datenanalyse schloss Instantonen auf Basis der QCDINS Vorhersagen mit ein. Die analysierten Daten enthielten keinerlei Hinweise auf Instanton-induzierte Ereignisse.

Der Schwerpunkt im zweiten Teil der Analyse ist die Ausrichtung der Komponenten des CMS-Spurdetektors. Die verwendeten Daten stammen von Kosmischen Datensätzen, die vom CMS-Detektor am Large Hadron Collider im Jahr 2012 aufgenommen wurden. In diesem Teil werden Messungen der schwachen Moden ("weak modes") zur Ausrichtung des Spurdetektors besprochen, sowie detaillierte Untersuchungen zum "z-rescaling" vorgestellt. Die Untersuchungen beinhalten auch die Simulation dieser schwachen Moden, sowie die Implementierung der Ausrichtungsprozedur Anhand der Simulationsergebnisse. Aus den hier gezeigten Ergebnissen ist ersichtlich, dass die Ausrichtungsprozedur für den CMS-Spurdetektor stabil ist gegenüber den drei schwachen Moden: "Twist, Sagitta und Telescope", was für drei Typen systematischer Abweichungen der CMS-Spurdetektorgeometrie steht. Das "z-rescaling" zeigt starke unerwartete Verschiebungen einiger Detektorkomponenten in z-Richtung. Um dieses Problem näher zu untersuchen, wurde eine signifikante Anzahl an Tests durchgeführt, unter anderem: Nur "high level"-Ausrichtung, Ausrichtung mit fixierten Endkappen, Einfluss der p_T-Abhängigkeit der Spuren auf die Ausrichtungsprozedur, Simulation von kosmischen und Kollisionsereignissen, Beschränkungen auf die Position der TID, TEC Endkappen-Scheiben und einige andere Tests. Obwohl dies leider nicht genügte, um die Problematik vollständig zu lösen, waren die Untersuchungen, die Teil der hier vorgestellten Doktorarbeit sind, in sich konsistente und wichtige Schritte, die das Problem besser beschreiben und als Grundlage dienen, diese Probleme in der Zukunft lösen zu können.

Die Spur-Helix-Parametrisierung sowohl der ZEUS-, wie auch CMS-Daten wurde untersucht. Eine detaillierte Beschreibung der Parametrisierung, wie auch der Transformation des

CMS Formats ins ZEUS-Format wird vorgestellt. Zusätzlich wurde eine Analyse der CMS Daten zum $B \to J/\psi K$ Zerfall begonnen. Die Analyse wurde mit den öffentlichen Daten des CMS-Experiments aus dem Jahr 2010 durchgeführt. Dies kann als erster Schritt hin zu einer Messung des totalen Beauty-Wirkungsquerschnittes bei CMS, auf Basis der Erkenntnisse der hier vorgestellten Datenanalyse der ZEUS-Messungen, gesehen werden.

Contents

Introduction

Kobayashi and Maskawa have predicted in 1973 the existence of a third generation of quarks, the top and bottom quarks [14]. After the theoretical prediction, the bottom quark was experimentally discovered in 1977 [1]. The heavy mass of the b quark provides a hard scale. Because of the confinement effect beauty quarks are studied via B-mesons.

A unique opportunity to study beauty quarks is realised on the pp collider LHC and the ep collider HERA. The Large Hadron Collider (LHC) creates the possibility to study gluon-gluon fusion in processes with very high luminosity. In turn collisions of electrons with protons occur by photon exchange and are thus determined by an interaction of photons and protons. In the context of the HERA collider the interacting photons have a continuous range of energies. Moreover, selecting events with electrons scattered at a large angle, the experimenters are able to study the interaction of highly virtual photons. Thus, the data obtained at the HERA collider, allow to study a wide range of reactions such the interaction of real or quasi-real photons (photoproduction) and deep inelastic interaction of photons with a high degree of virtuality.

This thesis presents measurements of the total and differential cross sections of beauty production at HERA. For the measurement of the total and differential cross sections secondary vertex information was used. The cross sections are in agreement with Next-to-Leading Order (NLO) QCD calculations.

While the CMS experiment at the LHC covers a large spectrum of physics and is focused on the search for new phenomena in the TeV range it needs to have a perfect tracking performance, which requires the detector calibration and alignment of the tracking detectors to be done with a high precision. In order to make a contribution to the detector calibration and alignment study, a significant part of my work was connected to CMS tracker alignment studies. The effect from weak modes of the alignment procedure is studied.

This thesis has the following structure. **Chapter 1** provides an introduction to the theory behind the measurements which were provided in this analysis. It gives the needed information about the Standard Model theory and beauty quark production at ep and pp collisions. **Chapter 2** gives a description of the experimental setup used to obtain the data for this analysis. It starts from the LHC and HERA colliders and explains the main parts of the CMS and ZEUS detectors. **Chapter 3** explains the general selection cuts which where used for the ZEUS analysis. **Chapter 4** contains the reconstruction description of the kinematic variable, muons, tracks and vertices. **Chapter 5** contains the description of the general measurement procedure

and determination of all processes contributing to the HERA analysis and contains a detailed description of the cross section measurements. **Chapter 6** presents the total and differential cross section measurement results. **Chapter 7** contains the information about the CMS tracker alignment studies in particular the weak modes study and a study of the z-rescaling weak mode. An outlook of the thesis and summary are provided in **Chapter 8**.
The track helix parametrization in the CMS exeriment is described in **Appendix A**. **Appendix B** contains the information about the track helix parametrisation in the ZEUS experiment, and contains a description of the transformation of the track paramters from the CMS into ZEUS formats. **Appendix C** contains a study of $B \to J/\psi K$ decays based on "Minimum Bias" and "Muon" open data samples released by the CMS experiment in the context of the of CMS Open Data project.

Chapter 1

Theoretical Overview

1.1 The Standard Model

The modern understanding of the physics of elementary particles is contained in the Standard Model (SM). The Standard Model of particle physics is based on quantum chromodynamics and electroweak interactions. Quantum electrodynamics (QED), a part of electroweak interactions [5] is a high precision theory which describes the processes occurring under the action of electromagnetic forces. QED has been studied with a high degree of accuracy. Quantum chromodynamics (QCD) describes the processes of strong interactions, constructed by analogy with QED. The main provisions of the Standard Model [3] are:

- All matter consists of 12 fundamental quantum spin $\frac{1}{2}$ fields, corresponding to fundamental particles, which can be grouped into three generations of fermions: 6 leptons (electron, muon, tau lepton, the electron neutrino, muon neutrino and tau neutrino) and 6 quarks (u, d, s, c, b, t) and the 12 corresponding antiparticles. Figure 1.1 shows a diagram of those particles.

– u, c, d quarks have a charge of $+2/3$, while d, s, b quarks have $-1/3$ of the electron charge. Up, charm, and top quarks are collectively referred to as up-type quarks, while down, strange, and bottom quarks are down-type quarks.

- There are four fundamental interactions: gravity, weak, electromagnetic and strong. Gravity is not included in the SM.

- All three types of interactions occur as a consequence of the postulate that our world is symmetric with respect to the three types of gauge transformations. The particles that transmit interactions are bosons:

  – 8 gluons for the strong interaction (symmetry group SU(3));

  – fundamental vector bosons for the electroweak interaction (W^+, W^-, W^0, B) are arranged into an initially massless isovector triplet (for SU(2)) and a massless isosinglet (for U(1)) [5];

  - As a result of spontaneous symmetry breaking, caused by the Higgs mechanism, three bosons (W^+, W^-, Z^0) acquire mass, and one (γ) remains massless.

- In contrast to the electromagnetic and strong interaction, the weak interaction can mix different generations of fermions, which leads to instability of all particles except for the lightest, and to such effects as violation of CP-invariance and neutrino oscillations.

- Quarks participate in the strong, weak and electromagnetic interactions.

- Charged leptons (electron, muon, tau lepton) participate in weak and electromagnetic interactions, while the neutrino only feels the weak interaction.

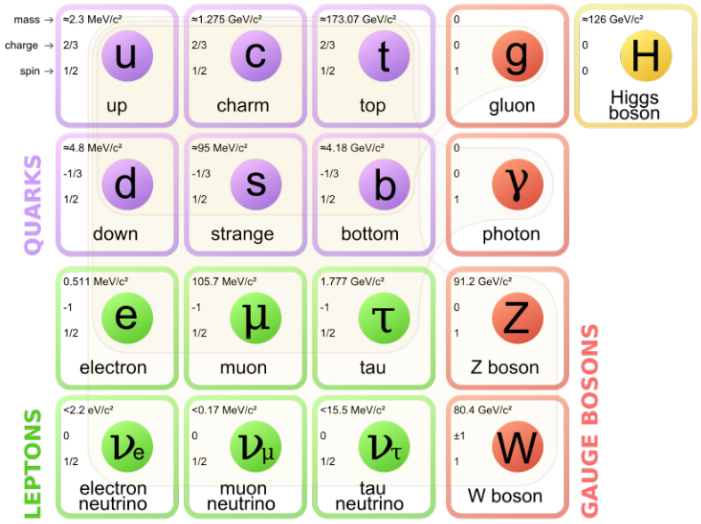

Figure 1.1: Standard model of elementary particles: the 12 fundamental fermions and 4 fundamental bosons. The light yellow-grey area indicates which bosons (red color) couple to which fermions (purple and green). The Higgs boson is shown in the fifth column (yellow color). The image is taken from [6].

- Hadrons are composed of quarks and gluons (partons). Quarks are fermions with spin 1/2 and a mass $m \neq 0$, while gluons are bosons with spin 1 and mass $m = 0$.

- Hadrons are separated into baryons which are made of three quarks and mesons which contain one quark and one antiquark.

- Quarks are classified according to two criteria: flavor and color. There are six known quark flavors and three color (SU(3)) charges for each quark. The flavor is a characteristic conserved in strong interactions.

- Gluons have both color and anticolour and all other quantum numbers except spin equal to zero. When a quark emits a gluon it changes the color but not the flavor. There are eight different gluons.

- Only color singlets may exist in the form of free particles.

- Quarks can not be separated from hadrons, a phenomenon called confinement. In other words, color charged particles (such as quarks) cannot be isolated singularly, and therefore cannot be observed as free particles. They can however be observed as pointlike constituents of hadrons.

- Between the quarks an attractive force is present with two unusual features:

  – asymptotic freedom [19] at very small distances. It states that the interaction between particles become asymptotically weaker with decreasing distance or with increasing energy. At high energies, quarks interact relatively weakly while at low energies quarks interact very strongly preventing the unbinding of baryons and mesons.

  – infrared slavery - confinement due to the fact that the effective potential energy of the interaction $V(r)$ increases indefinitely with increasing distance between the quarks.

- External parameters of the Standard Model are:

  – The masses of leptons (3 parameters, neutrinos are assumed to be massless) and quarks (6 parameters) are interpreted as interactions of their fields with the constant part (vacuum expectation value) of the Higgs field,

  – The CKM-matrix parameters of the quark mixing - three mixing angles and one complex phase that violates CP-symmetry,

  – two parameters of the Higgs field, which are uniquely associated with its vacuum expectation value and the mass of the Higgs boson,

  – three coupling constants, respectively, associated with the gauge groups U(1), SU(2) and SU(3), which characterize the relative strength of the electromagnetic, weak and strong interactions.

Quantum Chromodynamics.

Quantum chromodynamics is the quantum field theory of the strong interaction of colored gluon and quark fields. It is built on the principle of local gauge invariance under transformations in three-color complex space. QCD is also the basis for describing the strong interaction between hadrons and is responsible for the forces that bind quarks and gluons into hadrons. Together with the electroweak theory, QCD is the established theoretical base of particle physics.

In analogy to electric charge in quantum electrodynamics, in QCD there is a quark property which is called color. QCD colored quarks couple to 8 kinds of color gluon fields which are vector gauge fields of SU(3) Yang-Mills theory [3]. The gluon field, unlike the electromagnetic field, has color charge. Therefore it can itself generate gluon fields, and gluons interact which each other. The emission and absorption of gluons by quarks can change their color, but do not change the flavor.

QCD is a non-abelian gauge theory with symmetry group SU(3). Any matrix of the SU(3) group can be written in terms of its 8 generators, t^a. Hence, the number of possible types of

gluons is eight.

$$U = exp\{-ig\sum_a \theta_a t^a\}, \\ \text{where } a\ \epsilon\ (1-8), \text{and } [t^a, t^b] = if^{abc}t^c. \tag{1.1}$$

where g is the coupling strength, f^{abc} are the SU(3) structure constants, θ_a are coefficients which characterise the strength of each gluon field.
The t^a matrices are expressed by the Gell-Mann matrices [2]. The gluon field strength tensor $G_{\mu\nu,a}$ is :

$$G_{\mu\nu,a} = \partial_\mu A_{\nu a} - \partial_\nu A_{\mu a} - g\sum_{bc} f_{abc}A_{\mu b}A_{\nu c} \\ D_{\mu,ij} = \partial_\mu \delta_{ij} + igA_{\mu a}t^a_{ij} \tag{1.2}$$

where the $A_{\mu a}$ define the individual gluon fields, while $A_\mu \equiv \sum_{a=1}^{8} A_{\mu a}t_a$ is a matrix which describes all 8 gluon fields at once.

In QCD the requirement of local gauge invariance leads to the need to introduce the 8 vector boson gluon fields that interact. The requirement of local gauge invariance allows to uniquely construct the form of the Lagrangian of the Yang-Mills fields. As a result the locally gauge invariant QCD Lagrangian has the form [4]:

$$L_{QCD} = \sum_{f=1}^{n_f}\sum_{\alpha,\beta=1}^{4}\sum_{i,j=1}^{N_c} \bar{\psi}_{f,\beta,j}[i\gamma^\mu_{\beta,\alpha}D_{\mu,ji} - m_f\delta_{\beta\alpha}\delta_{ji}]\psi_{f,\alpha,i} - \frac{1}{4}\sum_{\mu,\nu}^{4}\sum_{a=1}^{N_c^2-1} G^a_{\mu\nu}G^{\mu\nu}_a \tag{1.3}$$

Where the number of colors, N_c is 3 for QCD, ψ_f is the quark field with indices f running through the quark flavors with n_f is number of flavors, and i, j are running over the three color indices, α, β are Dirac field indices. The γ^μ are the Dirac matrices. The constants m and g are the quark mass and coupling constants of the theory.

The gauge invariance implies that one and the same coupling constant describes the interactions of quarks and gluons and the self-interaction of the latter. The gluon self-interaction fundamentally distinguishes QCD from QED, although the interaction of quarks with gluons are in many respects similar to the interaction of electrons with photons.

The quark-parton picture of strong interactions for composed objects is the basis for the analysis and interpretation of experimental data involving the proton. The property of asymptotic freedom of quantum chromodynamics (QCD), a phenomenon occurring at large momentum transfers, allows a quantitative analysis and interpretation of observations using perturbation theory.

Perturbative quantum chromodynamics (pQCD) is a technique to calculate cross sections by an expansion in powers of the strong coupling constant, $\alpha_s = \frac{g^2}{4\pi}$. To use perturbative methods α_s should be much smaller than one. In case it is of order one, non-perturbative methods have to be used to investigate the theory. Perturbative QCD can provide calculations to different orders in α_s. The lowest order process is called the leading order (LO). Higher order calculations are "next-to" and the order. For example a calculation one step higher than

the leading order is called next-to-leading order (NLO). The same logic is used for NNLO and N^3LO.

A higher order calculation includes quark and gluon loops, so-called virtual corrections, which introduce divergences. In order to take care of these divergences the so-called renormalisation procedure has to be applied. It introduces an unphysical parameter, the renormalisation scale μ_r. This leads to the fact that in quantum field theory the interaction constant is not a constant but depends on the renormalisation scale. The formula (1.4) shows the leading order dependence of α_s on the renormalisation scale:

$$\alpha_s(\mu) = \frac{12\pi}{(33 - 2n_f)ln(\mu/\Lambda^2_{QCD})}, \tag{1.4}$$

where n_f is the number of quark flavors with mass less than μ_r. Λ_{QCD} is the scale paramter of QCD. Λ_{QCD} directly establishes a boundary for the usage of pQCD.

Figure 1.2 nicely shows the runnig of the strong coupling constant α_s. Thus for large

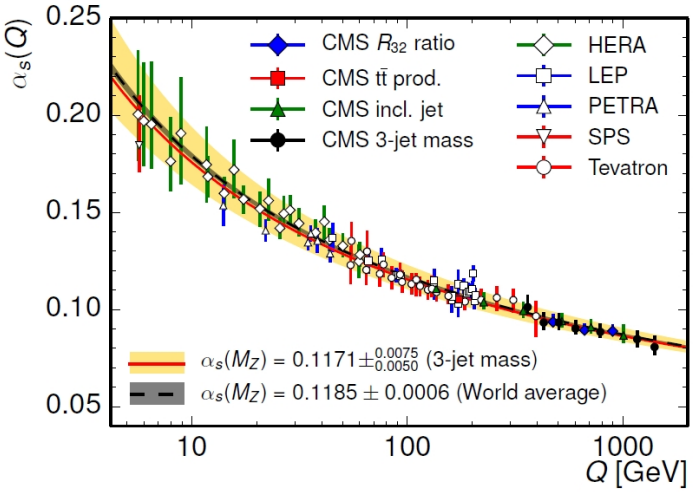

Figure 1.2: The running of the strong coupling constant $\alpha_S(Q)$ measured at different world experiments including results from HERA and CMS, as a function of the energy scale Q. The different symbols show results from different experiments. The image is taken from [7].

relevant energy/momentum scale μ_r or at short distances, the coupling constant of the strong interaction is reduced and quarks behave as quasi free particles. This phenomenon is called asymptotic freedom. With increasing distance or at low momentum scale values, the strong coupling constant α_s increases, which provides an indication of the inability to separate colored quarks to infinite distance because of the creation of quark-antiquark pairs and gluons. This phenomenon is called confinement and mathematically not yet fully resolved at the moment.

To calculate cross sections, integration over the virtual and real particles has to be performed. The integration process introduces infrared and ultraviolet divergences. Some of these divergences come from the emission of collinear gluons of the partons. The factorization theorem[20], introduces parton density functions (PDFs). The factorisation scale μ_f divides a process into hard and soft processes. While the hard process which includes the interaction of high energy particles, can be calculated with pQCD, a soft process is not covered by pQCD

and has to be treated by other means.
Because of factorisation, a PDF measurement at one scale, μ_f, allows the prediction of their evolution for another factorisation scale in the case when α_s is small. This evolution of the parton density functions is described by the Dokshitzer-Gribov-Lipatov-Altarelli-Parisi (DGLAP) equations [21].

1.2 Electron-proton and proton-proton cross section

1.2.1 Kinematic variable definitions for Electron-Proton Scattering at HERA

Electron-proton scattering at HERA is divided into neutral and charged current scattering, depending on the interaction process between the electron and proton. Figure 1.3 shows a

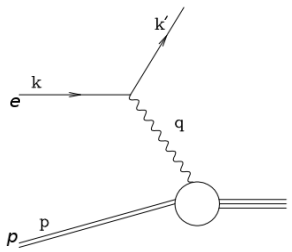

Figure 1.3: Lepton-proton scattering via exchange of boson.

sketch of the electron-proton interaction where either a virtual photon (γ) or a boson Z^0 is exchanged, in the case of neutral current interactions, or a $W^{\pm}$ boson in case of charged current scattering. The incoming electron with four-momentum k interacts with an incoming proton with four-momentum P, while the k' is the four-momentum of the scattered electron or neutrino. The exchanged boson has four-momentum q, which is defined as:

$$q = k - k'. \tag{1.5}$$

General parameters that describe electron-proton scattering at HERA are defined below.
The centre of mass energy s is given by:

$$s = (k + P)^2. \tag{1.6}$$

The inelasticity of the interaction, y with its physical range is given by:

$$y = \frac{P \cdot q}{P \cdot k}, \quad 0 \leq y \leq 1. \tag{1.7}$$

The inelasticity is the fraction of the electron momentum in the rest frame of the proton carried by the exchanged boson. The negative four-momentum transfer squared, or the virtuality of

the exchanged boson is defined as:

$$Q^2 = -q^2 = -(k - k')^2, \quad 0 \leq Q^2 \leq s. \tag{1.8}$$

The squared centre-of-mass energy of the boson-proton system is obtained as:

$$W^2 = (p + q)^2. \tag{1.9}$$

The Bjorken variable x is defined as:

$$x = \frac{Q^2}{2P \cdot q}, \quad 0 \leq x \leq 1. \tag{1.10}$$

The kinematic variables s, y, Q^2, x are Lorentz invariant.
The virtuality of the exchanged boson, Q^2 defines two kinematic regions: Deep Inelastic Scattering (DIS), and Photoproduction(PHP).

- $Q^2 \gtrsim 1\ GeV^2$: deep inelastic scattering (DIS),
- $Q^2 \approx 0\ GeV^2$: photoproduction (PHP).

1.2.2 Neutral and charged current differential cross section for DIS

Electron proton interactions can be divided into two types depending on the exchanged electroweak boson. The first type is the neutral current (NC) with the exchange of a neutral γ or Z^0 boson. In the case of the exchange of a charged $W^{\pm}$ boson the interactions are called charged current (CC). The general form for the double differential cross section for neutral current DIS at high energy can be expressed by the formula:

$$\begin{aligned} &\frac{d^2\sigma^{NC}(ep)}{dxdQ^2} = \frac{2\pi\alpha_{em}^2}{Q^4 x} \cdot [Y_+(y)F_2^{NC}(x, Q^2) - y^2 F_L^{NC}(x, Q^2) \mp Y_-(y)xF_3^{NC}(x, Q^2)], \\ &Y_{\pm} = 1 \pm (1 - y)^2, \end{aligned} \tag{1.11}$$

where F_L is the longitudinal structure function, and the $Y_{\pm}$ are expressed via the inelasticity variable. $F_2(x, Q^2)$ is a form factor which is called structure function. Including the γ/Z^0 interference, an additional structure function $F_3(x, Q^2)$ is introduced [9]. In case of integration over the hard and soft processes, the "cross section" (structure function) F_2 can be represented as a combination of perturbative and non-perturbative parts,

$$F_2 = \sum_a \int_x^1 C_2^a \left(\frac{x}{\xi}, \frac{Q^2}{\mu^2}, \frac{\mu_f^2}{\mu^2}, \alpha_s(\mu) \right) f_a(\xi, \mu_f^2, \mu^2) d\xi \tag{1.12}$$

where a means the sum over quarks, gluons and antiquarks, C_2^a are the hard-scattering functions (the coefficient functions), μ_f is the factorisation scale, ξ is the momentum fraction of the parton and f_a are the PDFs. For CC DIS scattering, the double differential cross section formula is

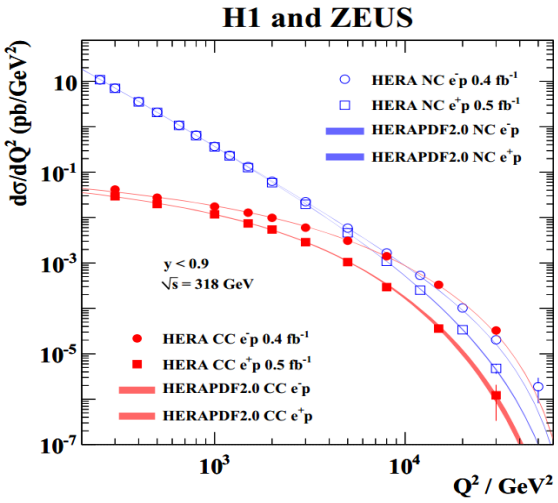

Figure 1.4: Comparison of the NC and CC differential cross sections in ep scattering. Different symbol types show the results from $e^{\pm}p$ experiments. The image is taken from [18].

written as:

$$\frac{d^2\sigma^{CC}(ep)}{dxdQ^2} = \frac{G_F^2}{4\pi x}\left(\frac{M^2}{Q^2+M_{W^\pm}^2}\right)^2 \cdot [Y_+(y)F_2^{CC}(x,Q^2) - y^2F_L^{CC}(x,Q^2) \mp Y_-(y)xF_3^{CC}(x,Q^2)], \tag{1.13}$$

where G_F is the Fermi constant. One can see, that for the low Q^2 region the $W^\pm$ and Z^0 exchanges are suppressed

$$\begin{aligned} &\frac{\sigma\,(W^\pm)}{\sigma(\gamma,Z^0)} \sim \frac{Q^4}{(Q^2+M_{Z^0,W^\pm}^2)^2}. \\ &\frac{\sigma^{CC}}{\sigma^{NC}} \sim \frac{Q^4}{M_{W^\pm}^4}, for\ Q^2 \ll M_W^2. \end{aligned} \tag{1.14}$$

Equation (1.14) shows that for the low Q^2 region the neutral current DIS process is dominant. The theoretical conclusion nicely agrees with the experimental results from the H1 and ZEUS experiments shown on Figure 1.4. The equation 1.11 shows that the electron proton DIS cross section dependence is $1/Q^4$. Thus the main cross section contribution will come from the photon exchange with a very low Q^2.

1.2.3 Heavy-Quark Production in ep collisions

DIS heavy quark cross section

The inclusive heavy-quark cross section in DIS is given in analogy to the equation (1.11) [10]:

$$\frac{d^2\sigma^{qq}(ep)}{dxdQ^2} = \frac{2\pi\alpha_{em}^2}{Q^4x} \cdot [Y_+(y)F_2^{qq}(x,Q^2) - y^2F_L^{qq}(x,Q^2)], \tag{1.15}$$

where the part with the structure function F_3 is very small for not too high Q^2 regions.
The heavy flavour structure functions ($F_{2,L}^{qq}$) are calculated in pQCD using the factorisation approach [12] (Eq. 1.12). In order to produce a $q\bar{q}$ pair the centre-of-mass energy of the photon

gluon system should be larger than the mass of the $q\bar{q}$ pair:

$$\widehat{s} = (\gamma^* + g)^2 > (2m_q)^2 \tag{1.16}$$

Figure 1.5(a) shows the BGF process which represents the dominant contribution to the ep beauty cross section. In BGF, the cross section of a beauty quark-antiquark pair is defined as [15, 99]:

$$\widehat{\sigma}^{BGF} = \frac{\pi e_q^2 \alpha_{em} \alpha_s}{\widehat{s}} \cdot \left((2 + 2\omega - \omega^2) ln \frac{1+\chi}{1-\chi} - 2\chi(1+\chi) \right) \tag{1.17}$$

where $\widehat{s} = (p_b + p_{\bar{b}})^2$ is the squared energy of the $b\bar{b}$ pair, $\omega = 4m_b^2/\widehat{s}$, $\chi = \sqrt{1-\omega}$. The cross section of charm quark-antiquark pair production is defined with the same formula (1.17), but with the appropriate charge and mass for the charm quark. Because of the higher mass and because the electric charge (e_b) of the b-quark is less (Sec. 1.1) than the c-quark electric charge the coefficient $\frac{e_q^2}{\widehat{s}}$ is significantly less for b-quarks which results in a smaller beauty cross section comparing to the charm cross section.

Photoproduction cross section

The photon in the Standard Model is a color-neutral particle but it can fluctuate into $q\bar{q}$ pairs. The lifetime of such fluctuations depends on Q^2 and increases with decreasing Q^2. At HERA, an electron scattered at very low angles can produce an almost real photon (with very low virtuality, Q^2), thus this type of ep reaction can be considered as γp collision. The photoproduction cross section can be expressed as [16]:

$$\frac{d^2\sigma^{ep}}{dydQ^2} \sim f^T_{e\to\gamma}(y, Q^2) \sigma^{\gamma p}_{tot}(y, Q^2), \tag{1.18}$$

where y is the inelasticity and the transverse photon flux , $f^T_{e\to\gamma}(y, Q^2)$ is defined as:

$$f^T_{e\to\gamma}(y, Q^2) = \frac{\alpha}{2\pi Q^2} \left[\frac{1 + (1-y)^2}{y} - 2\frac{1-y}{y} \frac{Q^2_{min}}{Q^2} \right], \quad Q^2_{min} = \frac{m_e^2 y^2}{1-y}, \tag{1.19}$$

and Q^2_{max} is an upper kinematic limit of the experiment. By integration over Q^2 in the range (Q^2_{min}, Q^2_{max}) the γp expression looks like [17]:

$$f^T_{e\to\gamma}(y) = \frac{\alpha}{2\pi} \left[\frac{1 + (1-y)^2}{y} - 2\frac{1-y}{y} ln \frac{Q^2_{max}}{Q^2_{min}} - 2\frac{1-y}{y} \left(1 - \frac{Q^2_{max}}{Q^2_{min}} \right) \right]. \tag{1.20}$$

Such an equation is known as Weizsäcker-Williams approximation.

1.2.4 Direct and resolved photoproduction

In the case of direct photoproduction, all the energy of the photon is transferred to the parton.

(a) (b)

Figure 1.5: Illustration for leading order Boson-Gluon Fusion direct photoproduction a) and resolved photoproduction b). Figures are taken from [23].

In resolved processes, the photons are considered as a source of partons. One of these partons is interacting with the proton's parton. Figure 1.5 illustrates the example of the leading order Boson-Gluon Fusion direct photoproduction (left) and resolved photoproduction (right) processes.

1.2.5 Hadronisation and Parton showers

Because of the confinement effect it is not possible to observe a single free quark. The formation process of mesons or baryons consist of two parts. The first part is perturbative, where in the scattering process additional partons are emitted from the heavy quark or from the initial parton and the quark parton showering takes place. The second part is non-perturbative, which is related to the hadronisation or fragmentation which is described with phenomenological methods, and describes hadron formation from the partons.

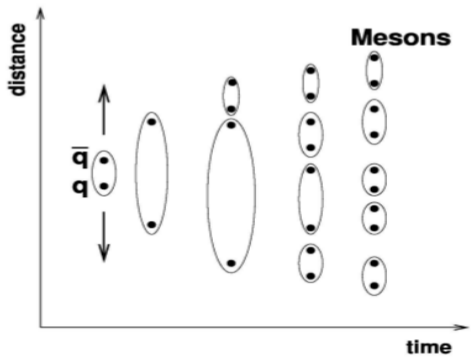

Figure 1.6: The string fragmentation model illustration.

The parton shower process describes the fact that partons can emit gluons or a gluon can split into a quark-antiquark pair. While the hadronisation process can not be calculated with pQCD methods, in this analysis Monte-Carlo generators were used, which use the string fragmentation model [42] to describe it (Fig. 1.6). In this model, the string is a $q\bar{q}$ pair connected by a color tube. Such a string has a uniform energy which corresponds to a linear quark confining potential. The potential rises when the distance between the quarks increases. It rises until the potential energy is enough to produce an additional $q\bar{q}$ pair, and the string then breaks. The string fragments are forming into hadrons.

1.2.6 Heavy-Quark Production in pp collisions

Heavy quarks, charm, beauty and top have a mass significantly larger than the light quarks (u,d,s). The heavy mass of these quarks provides a hard scale, such that the value of the strong coupling constant is low enough to use pQCD. This makes beauty quark production an important physical process to test pQCD. The heavy-quark production cross section in pp collisions is calculated in pQCD in a similar way to the ep collisions (Eq. (1.12), with using the factorisation approach:

$$\sigma^{Q\bar{Q}} = \sum_{i,j} \int_0^1 \int_0^1 dx_1 dx_2 f_i(x_1, \mu_f^2) f_j(x_2, \mu_f^2) \widehat{\sigma}_{ij \to Q\bar{Q}}(x_1, x_2, \mu_f^2) \tag{1.21}$$

where i, j means the sum over all partons, f_i, f_j are the PDFs for two protons and the perturbative part of the cross section is $\widehat{\sigma}_{ij \to Q\bar{Q}}(x_1, x_2, \mu_f^2)$ and μ_f is the factorisation scale.
At leading order two processes lead to heavy-quark production:

$$gg \to Q\bar{Q},\ q\bar{q} \to Q\bar{Q}. \tag{1.22}$$

Figure 1.7 shows the Feynman diagrams which are corresponding to these two processes.

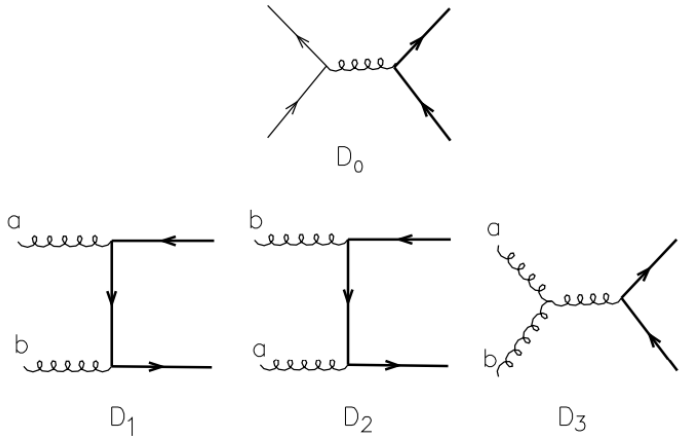

Figure 1.7: Leading-order diagrams for heavy-quark pair production. The image is taken from [22].

In $q\bar{q} \to Q\bar{Q}$, the $Q\bar{Q}$ pair is always in a colour-octet state. In $gg \to Q\bar{Q}$ both colour-singlet and octet are allowed. The process $q\bar{q} \to Q\bar{Q}$ is similar to $e^+e^- \to \mu^+\mu^-$. For the LO the total production cross-section for heavy quarks is finite even before renormalisation [22].

1.3 Beauty hadrons and their decay

Table 1.1 shows all the beauty and charm hadrons which are stable with respect to strong and electromagnetic interactions. The same table is valid for its antiparticles where quarks are exchanged with their antiquarks. It shows that the masses of the beauty hadrons are significantly higher than the charm hadron masses. The lifetime is longer for the b-hadrons as well. This can be explained with the Cabibbo-Kobayashi-Maskawa (CKM) matrix [14]. The

Hadron	Quark content	Mass, *MeV*	I (J^p)	Decay length $c\tau$, μm
B^+	$\bar{b}u$	5279.31 ± 0.15	½ (0^-)	491.1
B^0	$\bar{b}d$	5279.62 ± 0.15	½ (0^-)	455.7
B^0_s	$\bar{b}s$	5366.82 ± 0.22	0 (0^-)	452.7
Λ^0_b	bud	5619.51 ± 0.23	0 ($½^+$)	439.5
D^+	$c\bar{d}$	1869.58 ± 0.09	½ (0^-)	311.8
D^0	$c\bar{u}$	1864.83 ± 0.08	½ (0^-)	122.9
D^+_s	$c\bar{s}$	1968.27 ± 0.05	0 (0^-)	149.9
Λ^+_c	cud	2286.46 ± 0.14	0 ($½^+$)	59.9

Table 1.1: Recent PDG information of beauty and charm hadrons [13]. The values I is isospin, J is spin and p is parity of hadrons.

transition probability between two quarks is given by the CKM matrix element. The matrix values $V_{cb} \approx 0.04$ and $V_{cs} \approx 0.97$ result in a longer lifetime for the b-hadrons.

1.3.1 Semileptonic beauty decays

For this analysis an important ingredient is semimuonic decays. In this section this type of semileptonic decays will be discussed. The beauty quark weakly decays into a virtual $W^\pm$ boson and a charm quark. The $W^\pm$ boson then decays into muon $\mu^\pm$ and muon neutrino, $\nu_\mu(\bar{\nu}_\mu)$. Since the probability of the b-quark weak decay into a charm quark is more than one order higher than the probability of the decay $b \to u$, the predominant process is the decay of beauty hadrons via the production of an intermediate charm quark. Figure 1.8 shows an illustration of such a beauty weak decay. In turn after the weak decay of the b-quark, the

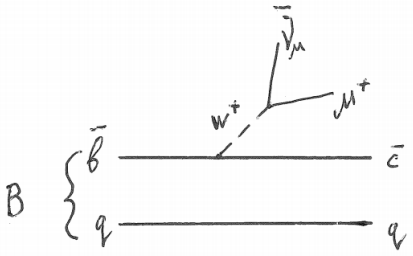

Figure 1.8: A beauty quark weak decay. The image is taken from [117].

charm quark may weakly decay into a $W^\pm$ boson and a strange quark. Such a process is called a weak cascade decay and is shown on Fig. 1.9. The b-hadrons are identified by their decay products which can be measured by the detector.
The probability of the muonic decay of the W-boson is equal to [13]:

$$p(W \to \mu\nu) = (10.63 \pm 0.15)\%. \tag{1.23}$$

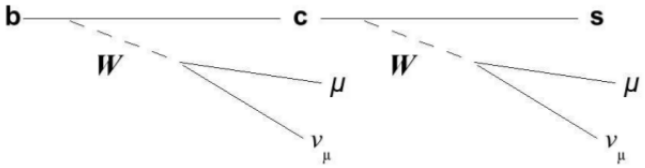

Figure 1.9: A beauty quark weak cascade decays. The image is taken from [117].

1.4 Muon pair sources in *ep* collisions

In this analysis beauty events are determined via the dimuon signature. However only muons which are coming from direct or cascade beauty quark decays are treated as signal events while the muons which come from the primary vertex are considered as a background. This section describes all possible physical processes which take place in this analysis and are treated later either as signal or background events.

1.4.1 Signal processes

All processes where a b-hadron decays into muons are treated as signal processes.

Muons from beauty decays

Muons from beauty decays can come directly from the beauty quark because of the weak decay $b \to Wc, W \to \mu\nu$. In turn the charm quarks can weakly decay as well, $c \to Ws$ with $W \to \mu\nu$. In the case when the muon is coming from the c-quark which comes from the beauty decay the process is called cascade beauty decay. The idea is to cover and consider all possible cases, which will help to understand the real muon source and hence the physical results. Figure 1.10 shows a sketch with direct and cascade beauty decays.

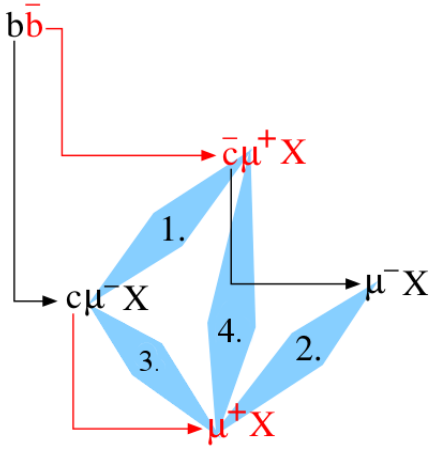

Figure 1.10: A sketch with direct and cascade beauty decays. The image is taken from [117].

The combination of two muons in the final state for the different cases shown on Fig. 1.10 gives a dimuon combination of either like- or unlike-sign. In addition, $B^0 - \bar{B}^0$ oscillations [118, 117] may lead to direct like-sign muon pairs when one of both B mesons has oscillated. This process takes place when a beauty quark oscillates into a antibeauty and vice versa. As shown on the

figure, a signal muon pair can be produced in four cases, from which only one combination may give like-sign pairs:

1. The direct beauty decay, where both beauty quarks semileptonically decay into charm quarks with producing the unlike-sign muon pair.

2. The cascade decay of both b-quarks, where both charm quarks decay with producing unlike-sign ($\mu^-\mu^+$) muon pair and s-quarks.

3. The case where information about the decay of one beauty quark is not directly measured, and both muons are prodced from the same b-quark. It produces an unlike-sign muon pair in the final state.

4. The case where the first beauty quark performs a direct decay while the second beauty quark makes a cascade decay. In such a case a like-sign muon pair is produced ($\mu^-\mu^-$, or $\mu^+\mu^+$).

1.4.2 Background processes

Quarkonium decays.
A source of unlike-sign muon pairs is the muonic decay of quarkonia states. Figure 1.11 (left) shows the decay of the charmonium state J/ψ (and the same for ψ') into a dimuon pair. Beauty (Υ) and lighter quarkonia states can decay in the same way. In general they are considered as background.

Figure 1.11: Feynman diagram with the decay of J/ψ and Υ mesons. The images are taken from [130].

The relevant charm $c\bar{c}$ states are referred to as J/ψ and ψ' mesons. Muons from the decays $b \to J/\Psi X \to \mu\mu X$ are considered as signal muons. Muons can also come from the light flavour quarkonia states such as $\phi, \rho^0, \omega, \eta, \eta'$ with low probabilities due to the different $\mu\mu$ branching ratio values. Because of the low mass these states can be removed from the analysis with a lower cut on the dimuon mass. The branching ratio and masses of the J/ψ- and ψ'-mesons are given from the PDG tables [13]:

$m_{J/\psi} = 3096.9 \pm 0.006\ MeV$ $\quad$ $BR_{J/\psi\to\mu^+\mu^-} = 5.961 \pm 0.033\ \%$

$m_{\psi'} = 3686.097 \pm 0.025\ MeV$ $\quad$ $BR_{\psi'\to\mu^+\mu^-} = 0.79 \pm 0.09\ \%$

The beauty quark states also relevant for this work are referred to an $\Upsilon(1S), \Upsilon(2S), \Upsilon(3S)$ mesons. The branching ratio and their masses are given from the PDG tables [13]:

$$m_{\Upsilon(1S)} = 9460.30 \pm 0.26\ MeV \qquad BR_{\Upsilon(1S)\to\mu^+\mu^-} = 2.48 \pm 0.05\ \%$$
$$m_{\Upsilon(2S)} = 10023.26 \pm 0.31\ MeV \qquad BR_{\Upsilon(2S)\to\mu^+\mu^-} = 1.93 \pm 0.17\ \%$$
$$m_{\Upsilon(3S)} = 10355.2 \pm 0.5\ MeV \qquad BR_{\Upsilon(3S)\to\mu^+\mu^-} = 2.18 \pm 0.21\ \%$$

The Υ-mesons produce unlike-sign di-muons (Fig. 1.11) which are not accompained by hadronic activity. In this analysis the three states of the Υ-meson listed above are considered as background processes.

Drell-Yan and Bethe-Heitler processes

There are two processes, Bethe-Heitler ($\gamma\gamma$ interaction) and Drell-Yan ($q\bar{q}$ annihilation) which can produce isolated muon pairs without limitation on the dimuon invariant mass.

(a) (b)

Figure 1.12: LO Feynman diagrams for Bethe-Heitler (a) and Drell-Yan (b) lepton production. The images are taken from [117].

Figure 1.12 shows LO Feynman diagrams for Bethe-Heitler and Drell-Yan lepton production. The Drell-Yan process with muon production is an electroweak process in which the boson comes from $q\bar{q}$ annihilation. Due to the requirement of the resolved photon (as a source for quarks), such process has a small cross section and is strongly suppressed at HERA. The boson-boson fusion process is called the Bethe-Heitler process and is the dominating process for the production for exclusive dimuon final states at the HERA experiments. In this analysis, these processes are considered as background processes and are separated from the signal events with a muon isolation requirement.

Open charm production

Charm meson, D , D^0 , D , D_s, may be directly produced at the ep collision point.

Figure 1.13 (a,b) shows D^0 and D^+ meson decays with producing muon and neutrino in the final state. Figue 1.13(c) shows charm production diagram. Such decays produce non-prompt muon pairs which are treated as background in this analysis.

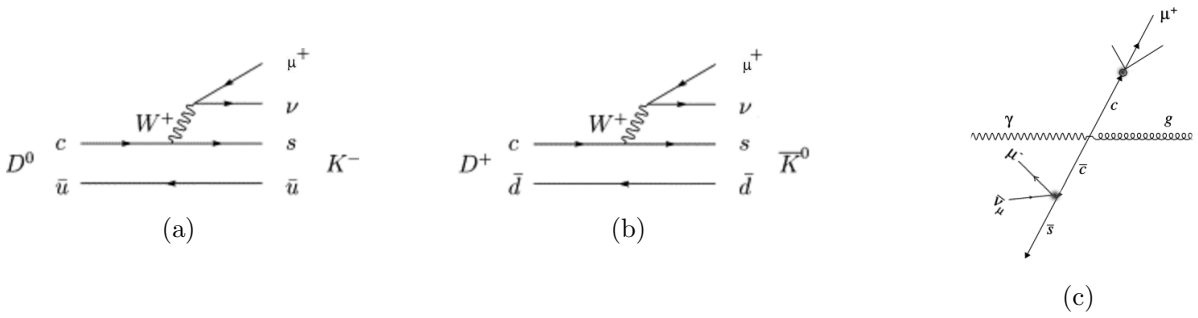

Figure 1.13: D-meson decays (a,b) and charm production diagram (c).

1.5 Monte-Carlo Simulation

In general Monte-Carlo simulation (MC) means calculations done by simulation programs based on MC methods. In this analysis the MC generators PYTHIA [39] and RAPGAP [40] were used to calculate the efficiencies and acceptances for *ep* cross section measurements as well as to describe signal and charm background distributions. But in general MC programs in high energy physics are used widely for different proposes such as checking of the detector perfomance, alignment of the detector or some its part etc. The PYTHIA and RAPGAP event generators use LO calculations and parton showers (LO, PS). The simulation of the particle collisions is done in two steps. The first step provided by PYTHIA and RAPGAP is an event simulation or generation. This step provides a list of particles in the final state with known parameters. The second step passes such events through a detector simulation.

Event generation

An *ep* collision event can be separated into a few steps as shown on Fig.(1.14) for a BGF process. This separation is possible because [99] LO + PS Monte-Carlos generators use the factorisation theorem.

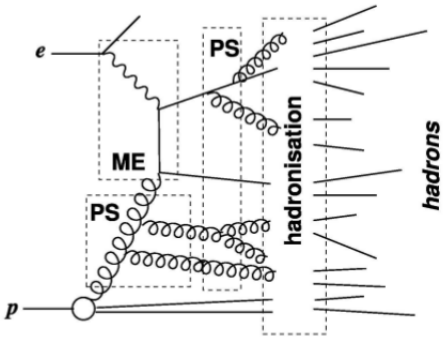

Figure 1.14: Structure of an event generated by a BGF process in *ep* collisions. The image is taken from [117].

Different steps in the event generation are [99]:

- **Hard subprocess.** The main part of the event simulation. It describes the interaction between the photon emitted by the electron and a parton extracted from the proton, e.g a gluon (Fig. 1.14). The momentum and flavour of the incoming parton are chosen

according to the chosen PDFs and are used as an input to the calculations. This part of the process can be calculated in a fixed order perturbative expansion since it involves a hard scale.

- **Initial and final state radiation.** Since the LO hard subprocess does not include parton showering (Sec. 1.2.5), this part of the event generation uses QCD based models. It describes real higher order corrections such as radiation of photons or gluons and gluon splitting into $q\bar{q}$ pairs.

- Hadronisation. In this process the formation of hadrons out of quarks and gluons takes place (Sec. 1.2.5).

- Particle decay. On this stage hadrons decay according to their branching ratios.

NLO calculations

There are different orders of the QCD calculations. The main difference of NLO compared to LO calculations is taking into account the radiation of hard gluons and including virtual (loop) corrections. Figure 1.15 schematically shows the difference between the LO and NLO calculations. Massive and massless schemes can be considered. In the massive scheme, the

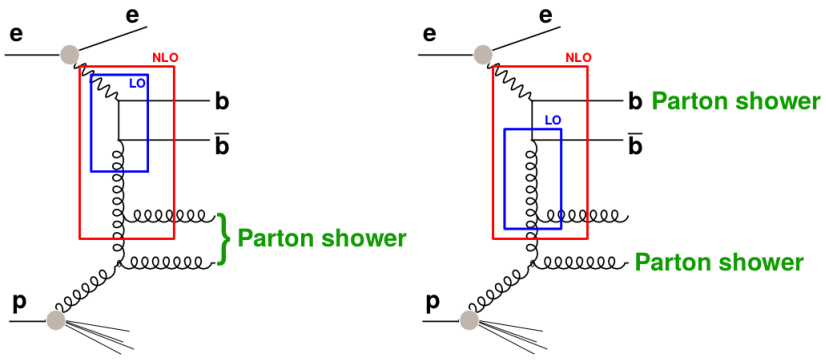

Figure 1.15: Leading order, Next-to-Leading Order in $b\bar{b}$ production. The image is taken from [117].

hadronic substructure of the proton and photon contains only the three quarks u, d and s as active flavours. Heavy quarks are produced only in the hard subprocess and have masses. In case of the massless scheme, the heavy quarks are considered as active flavours in the photon and proton and are massless [99]. In this analysis for NLO QCD calculations the FMNR $\otimes$ PYTHIA interface [41] was used for the calculation of differential cross section. It is based on the massive scheme and in photoproduction events it gives cross section predictions based on the Weizsäcker-Williams approximation (see Sec. 1.20). NLO predictions of the total cross section may be found at [41]. The value for the total cross section which is used in this analysis is: $\sigma^{NLO}_{total} = 7.5 \pm^{+4.5}_{-2.1} \ (syst.) \ nb$.

Chapter 2

Experimental Setup

2.1 The LHC and HERA Colliders

LHC collider

The LHC is constructed in the 27-km LEP tunnel at CERN in the Geneva region [79]. It provides the collisions of two proton (ion) beams of 7 TeV (2.75 TeV per nucleon, in 2010-2013) each, with a design luminosity of $10^{34} cm^{-2} s^{-1}$. One of the prime motivations of the LHC is to explain the nature of electroweak symmetry breaking for which the Higgs mechanism is supposed to be responsible. The beam energy and the design luminosity of the LHC have been chosen in order to study physics at the TeV energy scale. An event rate of approximately 10^9 inelastic events/s is observed for the general-purpose detectors like the CMS detector [69].

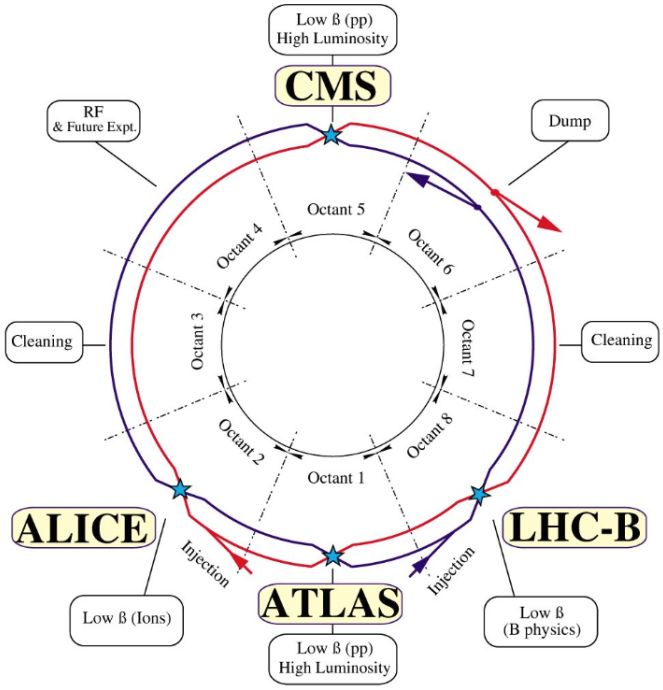

Figure 2.1: Overview of the LHC accelerator complex. It contains 4 main experiments (detectors): ALICE[74], CMS[76], LHC-B[77] and ATLAS[75]. The image is taken from [68].

At the LHC 4 big detectors were installed. These are the ALICE, CMS, LHC-B and ATLAS

detectors [69]. Figure 2.1 shows how they are positioned at the LHC ring.

HERA collider

The Deutsches Elektronen-Synchrotron (DESY) is a national research center in Germany that operates particle accelerators used to investigate the structure of matter. It was founded in 1959 in Hamburg. DESY's function is to conduct fundamental research. It specializes in:

- Construction, operation and development of particle accelerators.
- Research in particle and astroparticle physics to study the fundamental characteristics of matter and forces.
- Research in photon science including surface physics, chemistry, material science, and more.

The research with elementary particles started since 1960. DESY has famous ring accelerators such as PETRA [43], which is used as a synchrotron source since 2007 and the HERA (Hadron Elektron Ring Anlage) [44] operated until 2007. It has also the free electron laser (FLASH [45]) accelerator and its next generation, the XFEL [46].

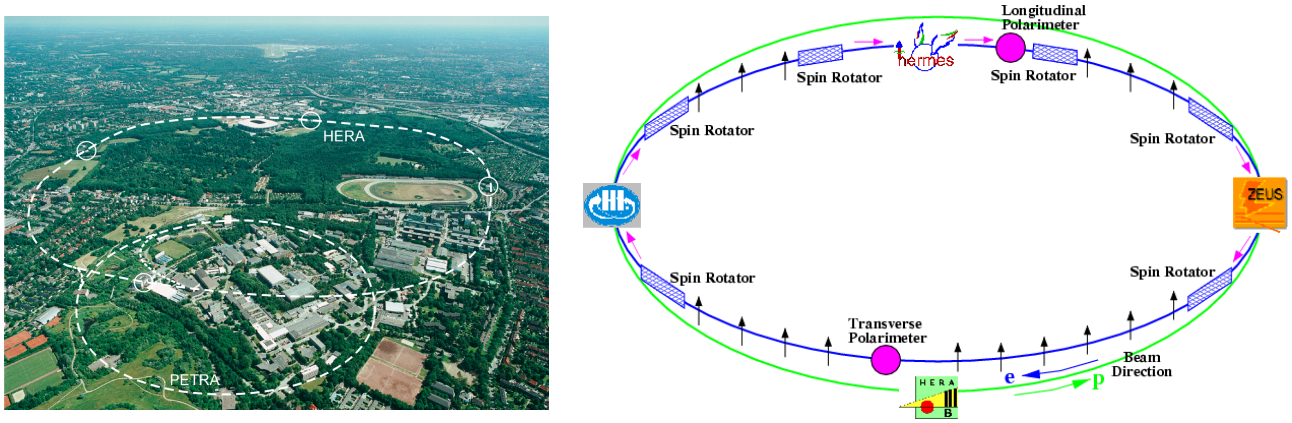

(a) (b)

Figure 2.2: The DESY research center in Hamburg [48][49].

The HERA and PETRA ring are shown on figure 2.2(a). Figure 2.2(b) shows the HERA accelerator which was the first accelerator which allowed for electron-proton colliding beam experiments. The accelerator was installed in 1990. The HERA ring was in operation during the years 1992 to 2007. The energy of the accelerated electrons was 27.5 GeV. Since 1998 the energy of the proton beam was 920 GeV, while till 1998 it had 820 GeV. The highest center of mass energy was $\sqrt{s} = 318$ GeV. The collider provides electron-proton collisions. A chain of pre-accelerators such DORIS, DESY II, DESY III, PETRA, provided beams for the HERA collider.

An illustration of the pre-acclerators system and the HERA ring is shown in Figure 2.2. The HERA operating time can be divided into two periods. The first part is HERA I (1992-2000) and the second one is HERA II (2003-2007).

Four experiments used the HERA facility (see Fig.2.2(b)). These are the ZEUS [51], H1 [52], HERA-B [53], and HERMES [50] experiments. The main goal of the ZEUS and H1 experiments was to measure the parton distributions of the proton. For this purpose, electrons from the electron beam were used as probes of the proton. HERA-B used the proton beam only and intended to measure CP violation via the measurement of J/ψ production originating from b-decays. The HERMES experiment used the electron beam only and mainly measured the spin structure of the nucleons.

2.2 The ZEUS Detector

The goal of the ZEUS detector [58] is to determine with high precision the energies, directions and the nature of single particles and particle jets created in the interactions. The ZEUS detector was located in the South hall of HERA. Its dimensions were $12m \times 10m \times 19m$. Its total weight was 3600 tons. Figure 2.3 shows the cross section of the ZEUS detector along the beam axis with different labels for the detector parts. This figure presents the detector configuration for the HERA I period (1992-2000). For the time period from 2003-2007 (HERA II) the VXD was replaced by the MVD and the TRD by the STT. The most important part

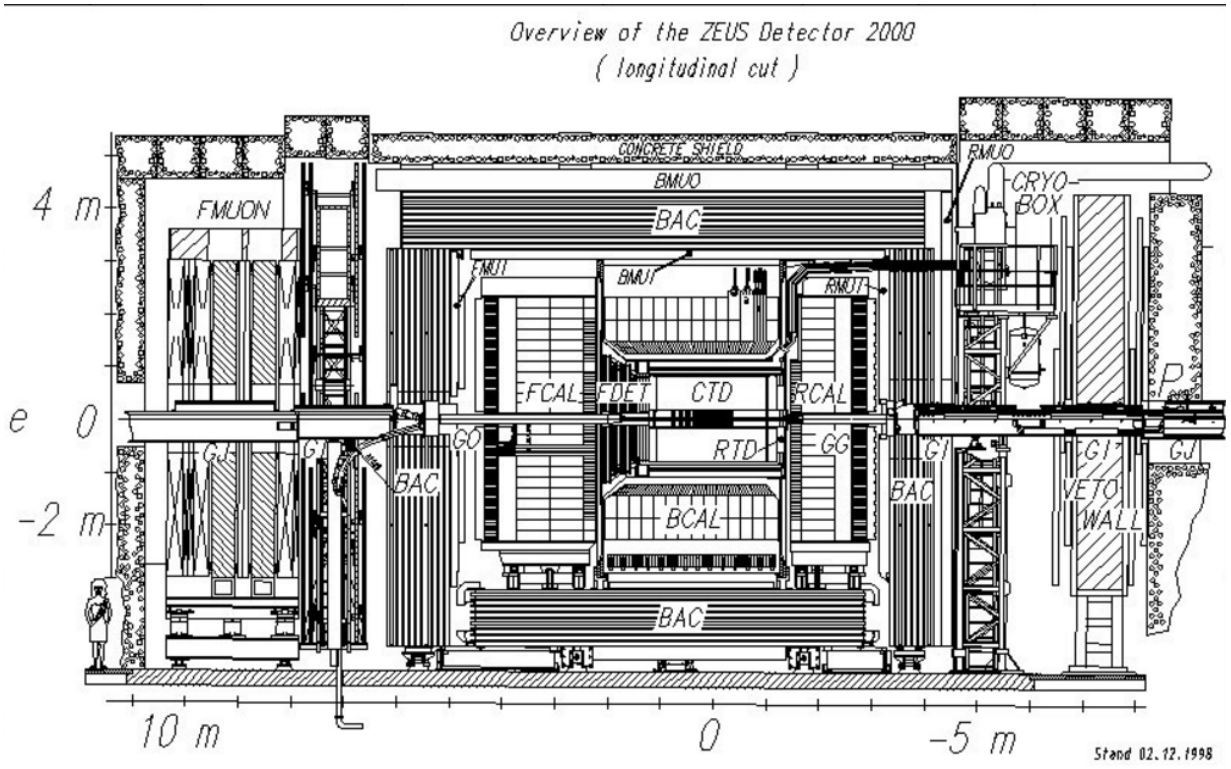

Figure 2.3: The cross section of the ZEUS detector along the beam axis[51].

of the ZEUS detector is the uranium scintillator calorimeter (CAL) which measures energies and directions of particles and particle jets with high precision. It hermetically encloses the tracking detectors which measure the tracks of charged particles using wire chambers and which consist of: a micro vertex detector (MVD), the central drift chamber (CTD) [54], forward

tracking detector (FTD) and a straw tube tracking detector (STT) to improve the tracking efficiency and reliability in the forward direction of the ZEUS detector and help to improve the tracking efficiency in high track multiplicity events. The tracking chambers are surrounded by a thin superconducting solenoid coil producing an axial magnetc field of 1.43 T [59] for the determination of the momenta of charged particles from the track curvature. Energy not fully absorbed in the uranium calorimeter is measured in the backing calorimeter (BAC) which uses the $\sim$ 7 cm thick iron plates of the return yoke as absorber and proportional tube chambers for observing penetrating particles.

Particles which are not absorbed in the substantial material of the uranium scintillator and backing calorimeter are typically identified as muons. Their tracks are measured before and after the iron yoke by limited streamer tube chambers (MUON). The muon momenta are determined by the deflections of their paths by the solenoid magnetic field and by the iron yoke which is magnetized toroidally up to 1.6 T by copper coils. In the forward direction magnetized iron toroids instrumented with limited streamer tube and drift chambers measure very energetic muons (up to 150 GeV/c). An iron wall equipped with two layers of scintillation counters (VETOWALL) is placed near the tunnel exit for the detection of background particles produced upstream by the proton beam. For the HERA I period, in the very forward direction a leading proton spectrometer was installed in the beam line to measure forward scattered protons. In the direction of the electron beam photons and electrons are detected in the luminosity monitor [60].

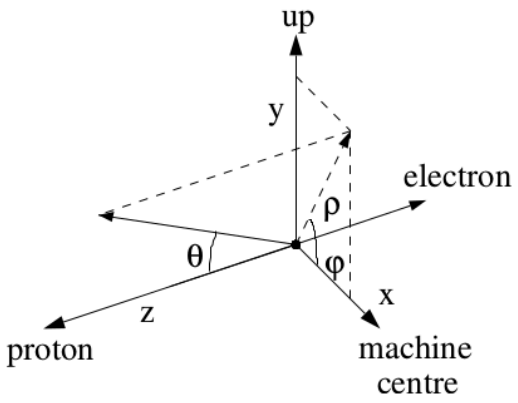

Figure 2.4: The ZEUS coordinate system. The center of the coordinate system is placed at the center of the CTD. This point not always matches with the the electron-proton interaction point. The image is taken from[99].

The ZEUS detector coordinate system is illustrated on Figure 2.4. It is a right-handed orthogonal system with the origin at the center of the CTD. The x-axis points to the HERA circle centre. The y-axis is pointing straight up, perpendicular to the earth's surface (more precisely perpendicular to both x- and z-axis). The z-axis is pointing along the proton beam. The azimuth angle ϕ is measured relative to the x-axis while the polar angle θ is measured relative to the z-axis. Often used is the pseudorapidity variable η, which is longitudinally

Lorentz-invariant for massles particles and calculated from the polar angle as:

$$\eta = -ln\left(tan\left(\frac{\theta}{2}\right)\right) \tag{2.1}$$

2.2.1 The Central Tracking Detector and the Microvertex Detector

The Central Tracking Detector (CTD) measured the momenta of charged particles [54] in the 1.43 T magnetic field. It was used for the track reconstruction in the polar angle window $15^0 < \theta < 164^0$. The main purpose of the CTD was to measure the curvature of charged tracks. The CTD was also used to locate the interaction point of the $e^{\pm}p$ collisions along the z-axis. It consists of 9 concentric superlayers which have radial and stereo components. The CTD

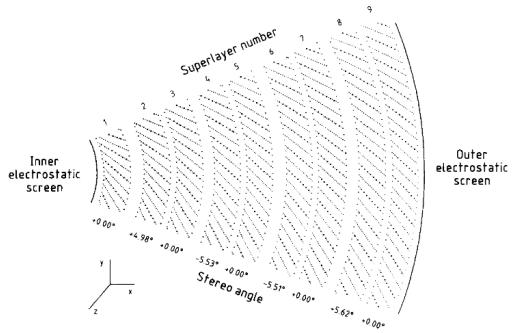

Figure 2.5: One octant layout in the central tracking detector. Nine superlayers organised in the radial direction are shown. The inner radius of the central tracking detector was 18.2 cm, while the outer was 79.4 cm. The image is taken from [54].

had the angular coverage of $15^o < \theta < 164^o$. The resolution of transverse momentum, p_T was determined to be: $\sigma(p_T)/p_T = 0.0058p_T \otimes 0.0065 \otimes 0.0014/p_T$ [67].

2.2.2 Uranium and Barrel Calorimeters

The Uranium calorimeter (UCAL) of the ZEUS detector is placed around the central tracking detectors and the solenoid, and can be divided into three parts: the forward (FCAL), the backward (RCAL) and the barrel (BCAL) calorimeters (Figure 2.6). The sections consist of modules, that are further segmented in towers. The wavelength shifter plates (WLS) divide the system longitudinally into the outer, hadronic (HCAL) part, and the inner part called electromagnetic (ECAL) [56, 57]. The FCAL covers polar angles from $\theta = 2.2^o$ to 39.9^o, the BCAL from $\theta = 36.7^o$ to 129.1^o and the RCAL from $\theta = 128.1^o$ to 176.5^o [55].
The UCAL was optimised for the best possible resolution in the measurement of hadronic jets with homogenous response. This was obtained by achieving equal response for the electromagnetic and the hadronic parts of jets, e/h = 1. The energy resolution of the UCAL was measured under test beam conditions [56] and the following equations were obtained (E in GeV) for hadrons:

$$\frac{\sigma(E)}{E} = \frac{35\%}{\sqrt{E}} \oplus 2\%, \tag{2.2}$$

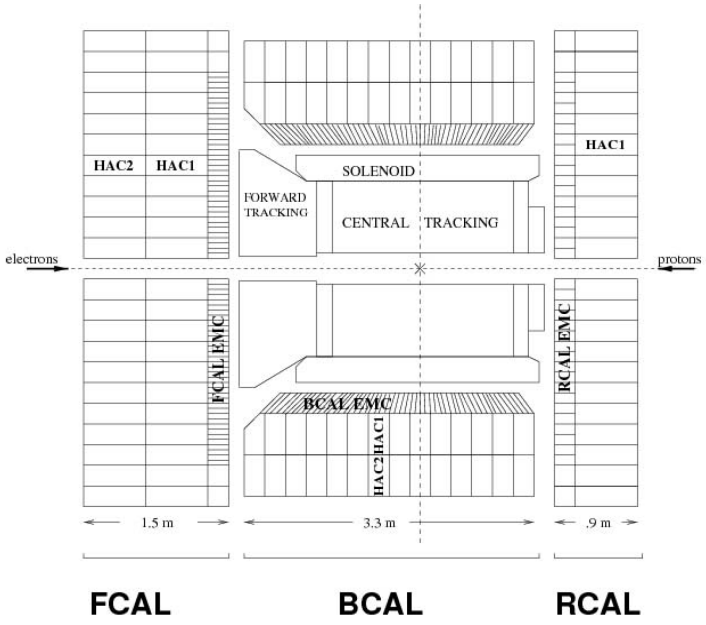

Figure 2.6: Shematic view of the UCAL. The image is taken from [57].

and for electrons:

$$\frac{\sigma(E)}{E} = \frac{18\%}{\sqrt{E}} \oplus 1\%, \tag{2.3}$$

2.2.3 Muon Detectors

The muon detectors are an important part of the ZEUS detector which is necessary for the beauty analysis. The muon detection system consists of a barrel muon detector (BMUON), rear muon detector (RMUON) and a forward muon detector (FMUON). Figure 2.7(a) shows an exploded view of the rear and barrel muon detectors.

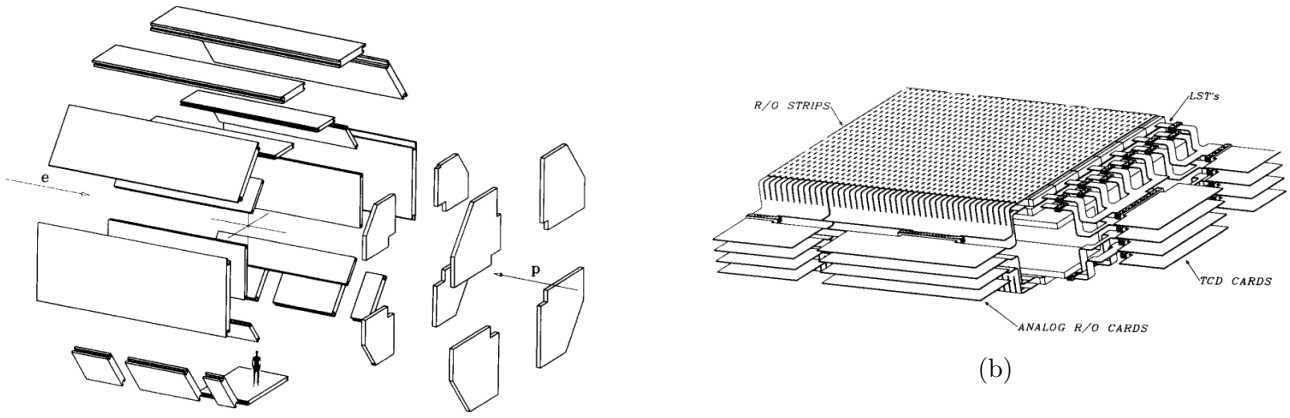

(a) (b)

Figure 2.7: Exploded view of the rear and barrel muon detectors (a), and layout sketch of the single element of a BMUO chamber [61].

The FMUON consists of four drift chambers and four planes of limited streamer tubes

(LST). Four planes of limited streamer tubes are used to define a trigger on high energy muons, selecting both according to direction and magnetic deflection. Four planes of drift chambers give very precise position measurements for momentum evaluation [62]. The LST and drift chambers are mounted on the inner and outer surface of the yoke, FMUI, FMUO [61]. The coverage of the FMUON in polar angle is $6^o < \theta < 32^o$.

The main task that the barrel and rear muon detectors have to accomplish is to identify pointing tracks penetrating the total calorimeter and iron thickness and, by re-measuring their momentum and comparing this measurement with that performed in the CTD, to reduce the background of non-prompt muons. A momentum constraint is obtained by measuring the direction of the particle before and after the magnetized iron yoke. The polar angle coverage of the outer barrel muon detector is $34^o < \theta < 135^o$. In turn, the rear muon detector has a polar angle coverage of $134^o < \theta < 171^o$. The BMUON has azimutal coverage of $-55^o < \phi < 235^o$. Each barrel chamber, inner (BMUI) or outer (BMUO), consists of 2 double layers of LST. Figure 2.7(b) shows a BMUO chamber sketch to give an idea of how a barrel chamber, LST looks like. Two double layers of LST are placed longitudinally with respect to the beam axis and are equipped with external read-out strips orthogonal (analog read-out) to the wires [63].

2.2.4 The Luminosity system

The luminosity (L) is an important parameter of any accelerator. It is directly related to the number of events (N) and cross section (σ) of the processes.

$$N = L \cdot \sigma \tag{2.4}$$

For the luminosity measurements a reference process should be chosen. The cross section of this process should be known well enough to get accurate precision. The process [64, 65] which has used at the HERA collider for luminosity measurements was:

$$ep \rightarrow e'\gamma p. \tag{2.5}$$

The photon or electron of this process was detected in dedicated detectors along the beam line [47].

2.2.5 Trigger System and Data Acquisition

A trigger does a first crude physics analysis of the events and select only those which contain useful information and processes. The ZEUS trigger system consists of three levels:

1. **The first level trigger (FLT)** [70]. On this stage a fast subdetector based reconstruction is performed. It takes a decision for each event. An event selection is done after a pre-analysis based on the information obtained from CAL and CTD. After that stage of trigger level selection the frequency of information flow is decreased to less than 1 kHz.

2. **The second level trigger (SLT)** [71]. All events which are selected by the first level trigger are analysed with the second level trigger. At this stage a fast complete event reconstruction is performed. All energy deposits are calculated. At this level a separation of events into DIS and photoproduction can be prepared. The information flow frequency is decreased to 100 Hz.

3. **The third level trigger (TLT)** [72]. After the FLT and SLT stage, an event is analysed by the third level trigger which performed an event reconstruction very similar to the one performed offline. The information flow frequency is decreased to about 10 Hz. At this level the final decision about recording the event is made.

2.3 The CMS detector

The Compact Muon Solenoid (CMS, [73]) detector was built to operate at the Large Hadron Collider (LHC) at CERN. The overall layout of CMS is shown in Figure 2.8. The CMS detector is 21.6 metres long, 15 m in diameter, and weighs about 14,000 tonnes. It is built around a huge solenoid magnet. The solenoid magnet has the form of a cylindrical coil of superconducting cable. It generates a magnetic field of 4T, which is about 100 000 times that of the Earth field. The main parts of the CMS detector which are usful for this analysis are: tracker detector, electromagnetic calorimeter, hadron calorimeter and muon detectors.

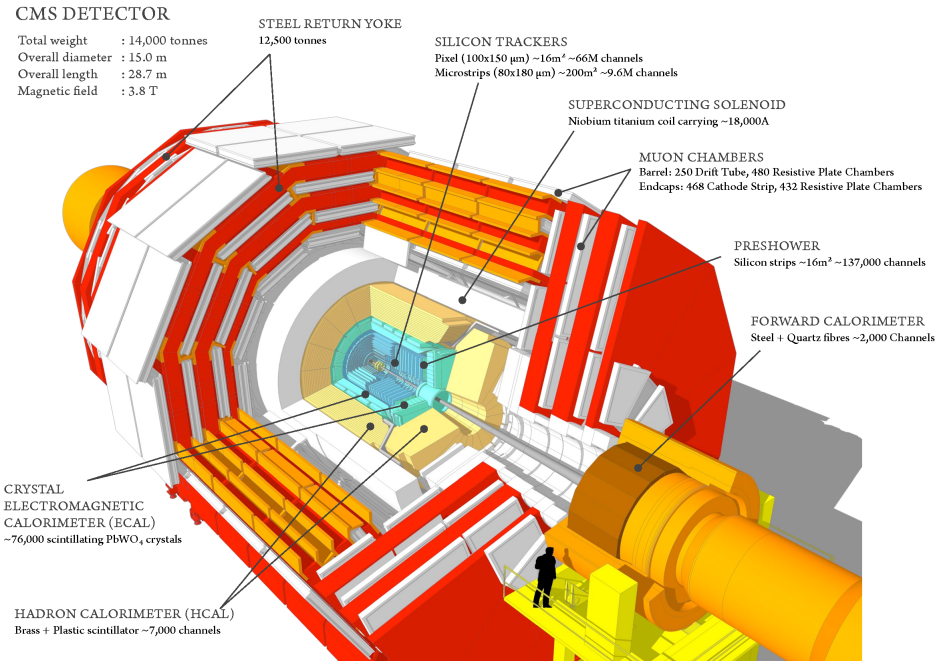

Figure 2.8: Sectional view of the CMS detector. The LHC beams travel in opposite directions along the central axis of the CMS cylinder colliding in the middle of the CMS detector. The image is taken from [73].

The coordinate system of CMS has the origin centered at the nominal collision point inside the experiment. The y-axis is pointing vertically upward while the x-axis is pointing radially inside the center of the LHC. The z-axis points along the beam direction. The azimuthal angle ϕ is measured from the x-axis in the $x-y$ plane. while the polar angle θ is measured from the z-axis.

2.3.1 The coordinate system and tracker global orientation

A right-handed coordinate system is used in the CMS experiment [129]. The interaction point is the origin of this system. The z-axis goes along the beam and in the anticlockwise to the LHC beam direction. The x-axis is pointed to the LHC ring centre. The y axis is pointing up, perpendicular to the x-z plane. The azimutal angle (ϕ) is measured from the positive x-axis in the $x-y$ plane. The polar angle (θ) is measured from the positive z-axis. Pseudorapidity

is defined as $\eta = -\ln[\tan(\theta/2)]$. In the cylindrical coordinates, the radius r defines the distance between the z axis and the point in the corresponding perpendicular $x-y$ plane [27].

Since the alignment procedure defines module parameters relative to each other the tracker outer barrel (TOB) has been chosen for the control point as a largest single component of the tracker. Measurements of the TOB position and angles in comparison to the designed(true) values define a rotation and shifts for the full CMS tracker. The alignment procedure uses predefined TOB parameters as the base for further tracker component alignment. The global tracker orientation is defined with θ_x and θ_y angles which quantify the TOB rotation around the x and y axis of the global coordinate system. Such coherent rotations of large parts of the tracker are very dangerous since they are hard to determine with the standard alignment procedure. The magnetic field direction is almost parallel to the z axis. In the case when θ_x and θ_y are not very small one can obtain distortions during the track transverse momentum measurements. This factor can significantly decrease the track reconstruction precision.

For each module a local coordinate system is defined (Figure 2.9). This system is characterized by three axes (u, v, w) and three rotation angles (α, β, γ). The u-axis is defined perpendicularly to the strips but in their plane and is thus more precisely measured than the others coordinates. The angle α characterises a rotation around the u-axis. The w-axis is perpendicular to the strip module plane with rotation angle γ. And the v-axis is going along the strips in the strip module's plane. The origin of the coordinate system is the geometrical center of the strip module.

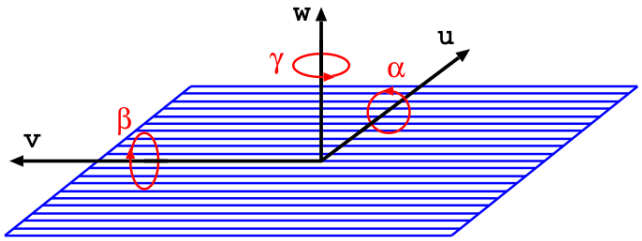

Figure 2.9: Sketch of a silicon strip module which shows the local coordinate system: u, v, and w, and the respective local rotation angles α, β, γ. The image is taken from [27].

For the pixel modules the v-coordinate is parallel to the magnetic field and the u-axis is orthogonal to the v-axis in a pixel module plane. As a connection to the global detector coordinate system the v-axis is parallel to the global z-coordinate. In general, the six parameters listed above are used for the module track-based alignment except of the dual strip modules for which additional three parameters are introduced.

2.3.2 Tracker components

As shown on Figure 2.10 the CMS tracker [27] consists of two big parts. There are pixel and strip detector parts. The pixel part is placed close to the interaction point, hence it has higher resolution in comparison to the strip one. Its consist of modules grouped into the forward pixel (FPIX) and the barrel pixel (BPIX).

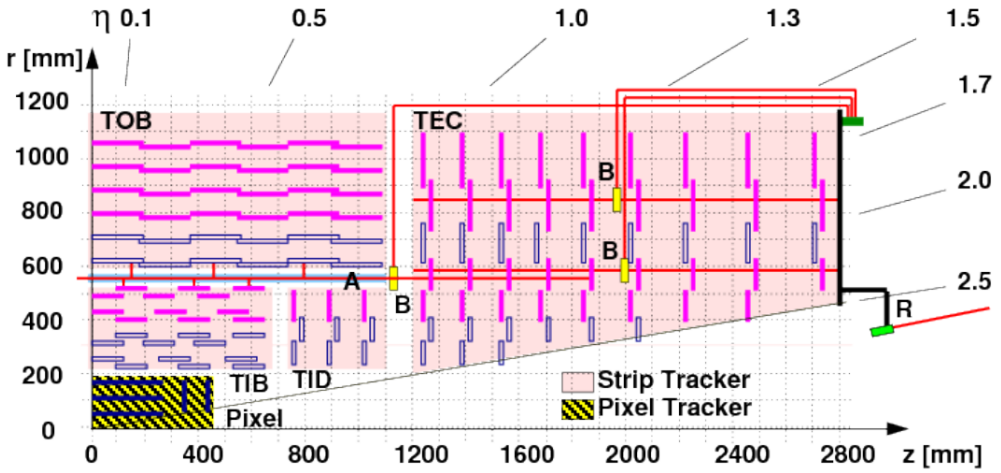

Figure 2.10: The CMS tracker one quarter sketch. The yellow area shows the pixel module position. The other areas contain solid and hollow rectangles. The hollow rectangles indicates strip module pairs with a relative stereo angle. The solid rectangles show single strip modules. The combination of the rectangles in the figure shows schematically how the strip detector layers are placed. The figure also shows the paths of the laser rays (R), the alignment tubes (A) and the beam splitters (B) of the laser alignment system. The image is taken from [27].

The strip tracker part is divided into four big groups. In the central rapidity region there are the tracker inner (TIB) and outer (TOB) barrel. Similary, the endcap detector region is divided into the tracker inner disks (TID) and tracker endcaps (TEC).

The FPIX as well as the TEC and TID consist of two symmetrical parts at positive and negative z hemispheres. Each part consists of a series of disks placed perpendicularly to the z-axis. TEC has nine when TID has three and FPIX only two such disks. The BPIX tracker part is separated into two cylindrical halves and each is a group of pixel modules. They are grouped in three concentric layers with radial positions at 4 cm, 7 cm, and 11 cm. The TOB and TIB tracker parts have the same structure with 4 and 6 microstrip layers. The TIB and TOB consist of two half-barrels for both direction in z [28].

The tracker consists of strip and pixel module types. The strip modules can register a signal in two modes: "peak" and "deconvolution"[32].

2.3.3 Tracker Detector

The trajectories and secondary vertices of charged particles are defined in the tracker of the CMS detector [78] system in the pseudorapidy range of $|\eta| < 2.5$. The tracker is designed in such a way as to combine simultaneously the requirements of high granularity and fast response, as well as the suppression of multiple scattering, bremsstrahlung, photon conversion and nuclear particle interactions. A transverse momentum resolution of about $1 - 2\%$ can be achieved for the tracks with high momentum (> 100 GeV) in the region of $|\eta| < 1.6$, and up to 1% for the tracks with low momentum [80].

In Figure 2.11 a schematic overview of the CMS tracker is shown. As already mentioned above, the tracker system combines two types of detection systems, pixel detector and silicon strip tracker. The pixel detector is the innermost part of the detector.

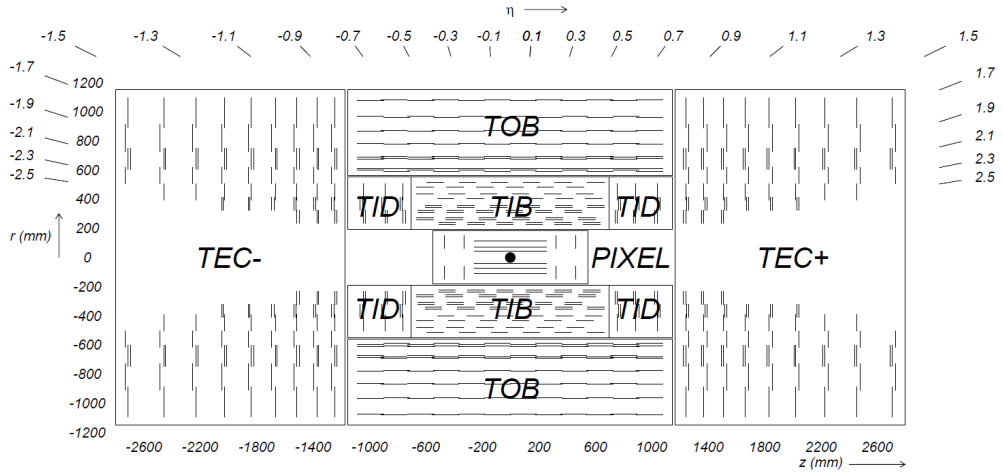

Figure 2.11: Schematic cross section through the CMS tracker. Each line represents a detector module. Double lines indicate back-to-back modules which deliver stereo hits. [79].

The pixel detector has 66 million pixels with sizes of $100 \times 150\ \mu m^2$ covering the area of 1 m^2. Thus, it is possible to obtain precise 3D vertex reconstruction with a spatial resolution of 10 μm and 20 μm in the $r - \phi$ and z directions accordingly [79].

The strip silicon tracker consists of three different subsystems. The inner parts are the Tracker Inner Barrel and Disks (TIB/TID) which cover the radius up to 55 cm and are composed of 4 barrel layers and 3 disks at the ends. The TIB/TID is surrounded by the Tracker Outer Barrel (TOB). It has an outer radius of 116 cm, consists of 6 barrel layers, and extends to 118 cm in z. The tracker EndCaps are labelled TEC+ and TEC-, according to the sign of the z coordinate. Each TEC has 9 disks and is placed in the region 124 cm $< |z| <$ 282 cm with a radius 22.5 cm $< |r| <$ 113.5 cm. The silicon strip tracker has 9.3 million strips and 198 m^2 of sensitive silicon area. The sensor elements in the strip tracker are single sided p-on-n type silicon micro-strip sensors [79].

2.3.4 Electromagnetic Calorimeter

The Electromagnetic calorimeter (ECAL) ensures high resolution energy measurements of electromagnetic showers. It consists of scintillating lead tungstate crystals (PbWO4), of which 61200 crystals are mounted in the barrel part (EB), and 7324 in each endcap part (EE). In front of the endcaps a preshower device is placed. The ECAL geometrical configuration is shown in Figure 2.12.

The choice of the crystal was based on its following properties: high density (8.3 g/cm^3), short radiation length (0.89 cm), scintillation decay time comparable to the bunch crossing time of the LHC. To keep the energy resolution stable, maintaining the temperature within 0.05 K is required. The photodetectors need to be operated in the 4T magnetic field together with a small yield of the scintillating crystal. Considering the different configurations of the magnetic field and the radiation level, different types of photodetectors should be used. Avalanche photodiodes are measuring the signal in the strong transverse magnetic field in the EB part.

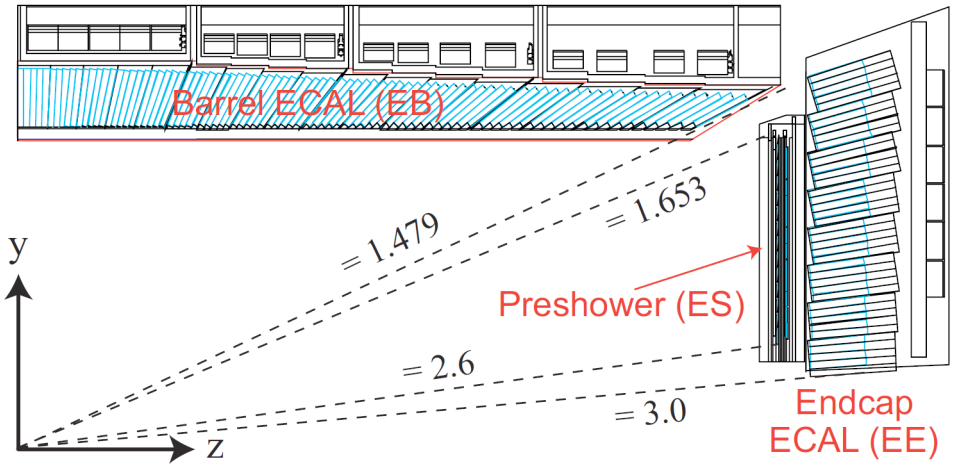

Figure 2.12: ECAL geometric configuration in the transverse plane. The image is taken from [82].

Vacuum phototriodes are used in the EE part, with very high radiation level. The EB part of the ECAL covers the pseudorapidity range $|\eta| < 1.479$. It has a 360-fold granularity in ϕ and consists of 61200 crystals. The crystals are contained in a thin-walled structure (submodule). This structure is made of an aluminium layer, facing the crystal, and two layers of glass fibre-epoxy resin. The submodules are assembled into modules of different types, according to the position in η, each containing 400 or 500 crystals. Four modules, separated by an aluminium conical web, are assembled in a supermodule, which contains 1700 crystals [79].

The EE part covers the pseudorapidity range $1.479 < |\eta| < 3.0$. It is composed of identically shaped crystals combined in units (supercrystals) of 5×5 crystals which create an alveolar structure. The crystals and supercrystals are arranged in a rectangular $x - y$ grid, with the crystals pointing at a focus of 1300 mm beyond the interaction point, so that the off-pointing angle varies with η [82].

The CMS Preshower (ES) identifies neutral pions in the region $1.653 < |\eta| < 2.6$ in the EE detector. Because of its high granularity the ES allows to distinguish between single photons and closely-spaced photon pairs. The ES is a sampling calorimeter with 2 layers. A lead radiator initiates electromagnetic showers from incoming photons/electrons whilst silicon strip sensors are placed after each radiator to measure the energy deposited and the transverse shower profiles [79].
The energy resolution below 500 GeV can be parameterized with the equation:

$$\left(\frac{\sigma}{E}\right)^2 = \left(\frac{S}{\sqrt{E}}\right)^2 + \left(\frac{N}{E}\right)^2 + C^2, \tag{2.6}$$

where S is the stochastic term, N the noise term, and C the constant term. A more detailed description can be found here [79]. The energy resolution is better than 2% in the CAL barrel region and between 2% and 5% for the other CAL parts [81].

2.3.5 Hadron Calorimeter

The hadronic calorimeter (HCAL) [83] measures the energy of hadronic jets and neutrinos through the missing transverse energy. Figure 2.13 shows the geometry and relative placement of the calorimeter parts [84]. The HCAL consists of different parts: the Hadron Barrel (HB), Hadron Endcap (HE), Hadron Outer (HO) and Hadron Forward (HF) calorimeters. HB covers the pseudorapidity range up to $|\eta| = 1.3$, HE extends until $|\eta| = 3.0$ and in the HF down to $|\eta| = 5.2$ can be covered. The pseudorapidity range between 1.3 and 1.4 is shared by HB and HE [85].

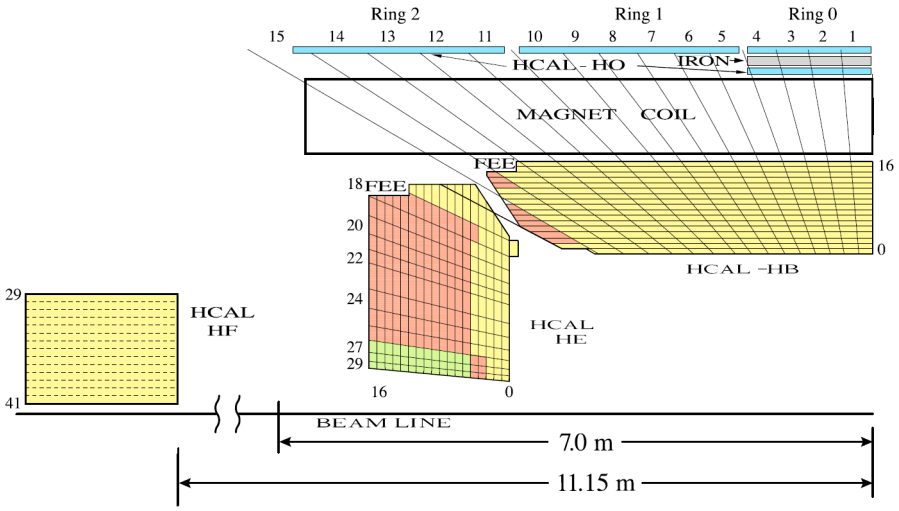

Figure 2.13: The CMS HCAL detector (quarter slice). The image is taken from [84].

The HB and HE consist of alternating layers of brass and plastic scintillator tiles. Brass (70% Cu and 30% Zn) is used as an absorber material and was chosen as non-magnetic material. The scintillator tiles are read out with wavelength shifting fibers. The HB consists of 36 identical azimuthal wedges and is divided into two half-barrels (HB+ and HB-). Each half-barrel is inserted from either end of the cryostat and positioned around the central axis of the CMS magnet. The HO calorimeter is placed outside the solenoid to catch the energy leakage from HB [85].

The two HF calorimeters are made of iron and quartz fibers. In the HF showers generated by electrons and photons are separated from hadronic showers by using two different lengths of the fibers. The Cherenkov light produced by the charged shower particles in the quartz fibers is registered by eight-stage photomultipliers with a borosilicate glass window [84].

2.3.6 Muon Detectors

Muon reconstruction and determination of their kinematic characteristics is of prime importance. Muons provide a signature for interesting events at LHC. Muons pass through all detector layers placed before muon detectors.

Geometrically the muon detector consists of a barrel part, which goes around the side surface of the solenoid cylinder and covers the kinematic region of pseudorapidity $|\eta| < 1.3$, and the

endcap part, which closes to the bases of the cylinder range $0.9 < |\eta| < 2.4$. The muon chambers are aligned to be perpendicular to the muon trajectories [86].

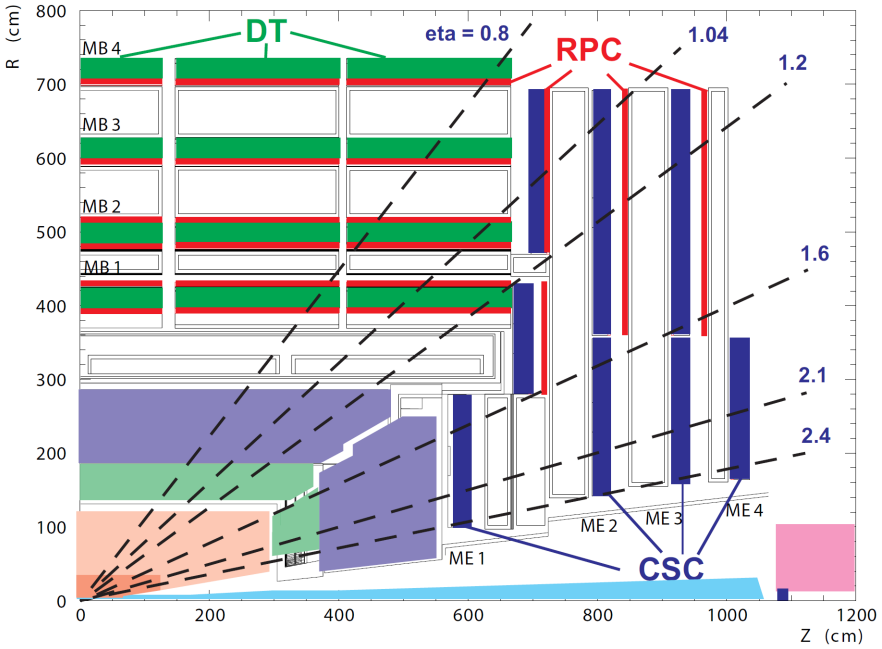

Figure 2.14: Scheme of one quarter of the CMS Muon detector system. The image is taken from [87].

Three types of detection elements are used in the different parts of the muon detector. In the barrel region with relatively low magnetic field drift tubes (DT) are deployed; in each endcap part, where the magnetic field and muon rate are high, cathode strip chambers (CSC) are used; resistive plate chambers (RPC) exist in both the barrel and endcap parts. Fig. 2.14 schematically shows the layout of one quarter of the muon CMS system with the detector dimensions and their relative position.

2.3.7 Trigger System and Data Acquisition

The collision of proton beams occurs in the LHC with a frequency of 40 MHz and the event recording speed is only about 300-600 Hz. The trigger system is performing the rate reduction to be suitable for the recording system level (suppression ratio $\sim 10^6$). The trigger system is organized in two stages called Level 1 (L1) Trigger and High Level Trigger (HLT) [88].
The architecture of the L1 Trigger system is shown in Figure 2.15. After the first level trigger the event rate will be limited to the frequency of 100 kHz. The first level trigger response time is 3.2 ms which includes the time required to deliver data from the detector to the trigger electronics, the decision time and passing the trigger signal back to the detector. The first level trigger decision is based on information from calorimeters and muon chambers. After the L1 trigger the readout of the front-end electronics is performed by the CMS Data Acquisition (DAQ) system and the HLT. At this stage the selection of high-quality physics data will be completed with further rate reduction up to 400 Hz [79].

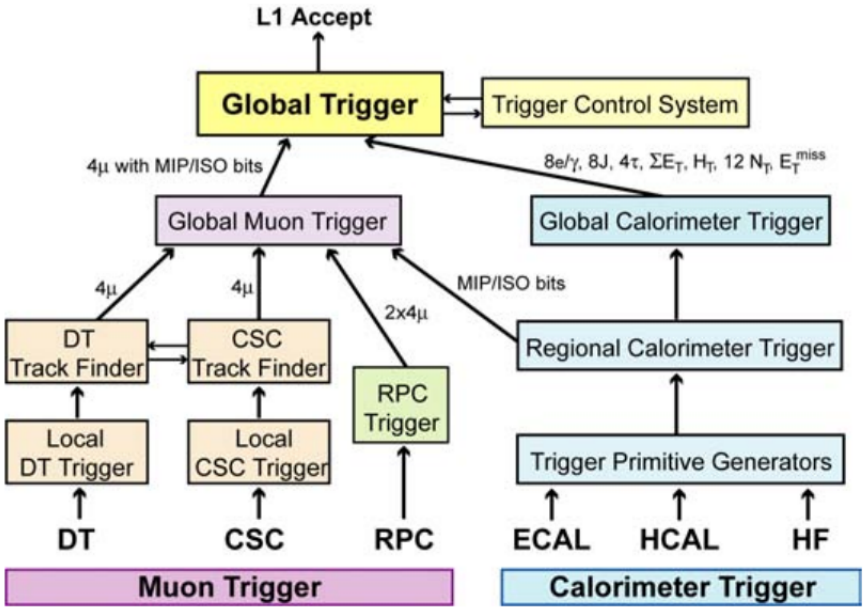

Figure 2.15: Architecture of the CMS Level-1 Trigger system. The image is taken from [79].

Chapter 3

Event Reconstruction

This chapter shows all general algorithms and procedures, with example results, which were used for the event analysis. Among them the reconstruction algorithm for the kinematic variables, for tracks and vertices, muons, for beauty quark identification, and the complete algorithm with examples for the decay length calculation.

As described in Chapter 2, the two beams collide at the point of interaction. The particles formed in this area subsequently fragment and decay. The point of production of the formed particles is called primary vertex. Figure 3.1 on the right, schematically shows B meson production and decay. The lifetime of b-hadrons is around 1.5 ps [13]. This corresponds to $c\tau \approx 450\ \mu m$ (Tab. 1.1), the approximate distance which a B particle flies through the detector. This allows the detection of secondary vertices. The hadronic products of the decay are forming a stream of hadrons which is called a jet. Figure 3.1 shows the sequential decay of a B hadron into a D* meson which in turn decays down into a kaon and two pions. A clear understanding of the process of decay and the knowledge about primary and secondary vertices provides a powerful tool for the beauty study in this analysis.

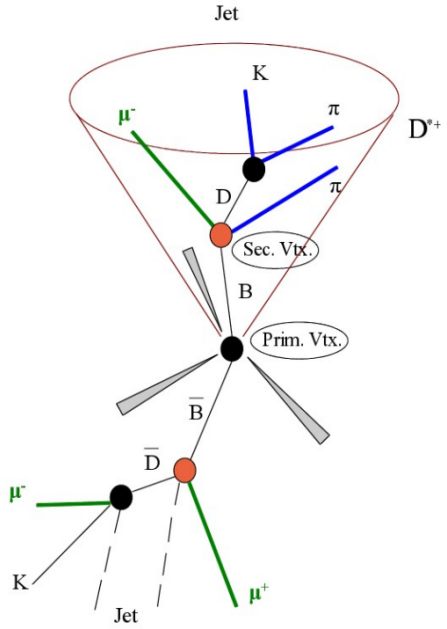

Figure 3.1: The example event illustration.

3.1 Reconstruction of Kinematic Variables for Electron-Proton Scattering at HERA

Kinematics for DIS.

The virtuality of the exchanged boson, Q^2, defines two kinematic regions: DIS and photoproduction (see 1.2.1). The deep inelastic scattering cross section for ep collisions for the inclusive process $ep \to eX$ mainly depends on three kinematic variables: the squared four-momentum transfer Q^2, the Bjorken variable x, and the squared centre-of-mass energy s. The squared centre-of-mass energy is defined as $s = 4 \cdot E_e E_p$. DIS events are characterized by a high boson virtuality, $Q^2 \geq 1GeV^2$ and large hadronic energy at the center of mass $W \gg m_p$, where m_p is the mass of the proton.

The electron kinematics is completely determined by two variables only. There are several possible choices for these two variables. Common choices are any two of (x, y, Q^2, W). For the structure function measurements, the results are usually quoted in terms of x and Q^2. The experiment measures the energy, E'_e , and polar angle, θ_e, of the scattered electron, and the longitudinal hadronic, p_z, and transverse, $p_{t\ had}$, momentum of the hadronic final state. There are many possible ways to combine these measurements and reconstruct the kinematical variables [101]. Here the Electron Method will be presented [102]. The photon virtuality Q^2 is defined by the equation:

$$Q^2 = -q^2 = -(k - k')^2 = 2kk' = 4E_e E'_e \cdot cos^2(\theta_e/2) \tag{3.1}$$

where the electron mass is neglected and θ_e is the angle between the scattered electron direction and the proton beam axis. With the equality $cos^2(2\theta) = (1 + cos(\theta))/2$, general equations for the electron method are:

$$Q^2 = 2E_e \cdot E'_e(1 + cos\theta_e) \tag{3.2}$$

$$y = 1 - \frac{E'_e}{E_e}(1 - cos\theta_e) \tag{3.3}$$

$$x = \frac{Q^2}{sy} \tag{3.4}$$

The invariant mass of the hadronic system W is defined as:

$$W^2 = (P + q)^2 \approx ys - Q^2. \tag{3.5}$$

At small y the resolution of the x measurement becomes bad, while this method shows very good x resolution at large y.

Photoproduction.

Photoproduction is the class of events where the Q^2 is very small (typically less than $10^{-2}GeV^2$[101], Sec. 1.2.1). For this kind of events, the electron is scattered at very small angles, and can not be identified with the main detectors. As was stated above the PHP events are characterized

by a low boson virtuality, $Q^2 \approx 0\ GeV^2$.

In photoproduction no scattered electron can be observed. In this case the Jacquet-Blondel [103] method is used. Reconstruction of the kinematic variable y_{JB} only requires the information of the hadronic final state:

$$y_{JB} = \frac{\delta_h}{2E_e}, \tag{3.6}$$

where $\delta_h = \sum_i (E_h^i - P_{zh}^i)$ and i loops over all hadronic final state excluding the scattered electron. In this analysis, for the DIS events the electron method has been used while for the photoproduction contribution the Jacquet-Blondel method has been chosen.

3.2 Track and Vertex Reconstruction

The vertex reconstruction is an important part of this analysis and thus a precise measurement as well as a detailed understanding of the track and vertex fitting procedure are main components discussed in this section. Here we will discuss the ZEUS reconstruction. Track hits are measured in the CTD, MVD and STT detectors. In the ZEUS experiment three different track types are defined:

- "Regular" tracks combine the MVD and CTD hit positions information and use pattern recognition based on a helix fit. Those tracks are obtained from the MVD and CTD tracks which are combined and connected between each other.

- "ZTT" tracks are the "Regular" tracks with Kalman filter information added. The accuracy of those tracks is improved by the Kalman filter fit procedure. For them the multiple scattering as well as the energy loss correction are applied. The parameters of those tracks are slightly different from the "Regular" tracks because they are improved by the Kalman filter [107].

All tracks are described with five helix parameters at their starting reference points. This parametrisation is extensively described in appendix B.

Reconstruction of the vertex. For independent vertex fitting and finding in HERA I, VCTRACK software package was used. The VCTRACK is the ZEUS package which performs vertex reconstruction. The VCTRACK vertex package is responsible to find the primary and secondary vertices and is based on χ^2 minimisation. Secondary vertices were caused by photon conversions ($\gamma \to e^+e^-$) and by long-lived particle decays (K_s^0, Λ). A more detailed information about VCTRACK package is here [97].

Secondary vertex candidates are fitted with additional information extracted from MVD and CTD. A few additional constraints are: the number of MVD hits greater than 4, number of CTD layers hits should be more or equal three and the transverse momentum of the track

should be more than 0.5 GeV. In this analysis secondary vertex candidates are obtained from the SECVTX data block [91]. The vertex reconstruction algorithm finds the best tracks combination and is based on the deterministic annealing filter (DAF) [108]. In case if the fit quality is acceptable by DAF, it provides three position coordinates of the secondary vertex and its covariance matrix [99].

3.3 ZUFO description

Charged and neutral particles make the energy deposit measured by the calorimeter. The resolution of energy measurements for the CAL increases with icreasing particle energy. The CAL has electromagnetic and hadronic type of cell layers. In turn, the momentum resolution of the CTD increases with lower particle energy. A combination of both, CAL energy measurement and track momentum measurement is called energy flow objects (EFO)[105]. In the ZEUS experiment they are called ZEUS Unidentified Flow Objects (ZUFO). The energy flow object reconstruction is performed in few steps [105]:

1. For each type of layer and for each of the CAL sections (FCAL, BCAL, RCAL), a combination of cells into a cell island is done separately. Each cell which is measured with enough energy deposit is considered as a candidate to be connected to the other neighbouring cells. This procedure is iterated, while a cell island is obtained. Cell islands may be caused by a single particle or a set of particles (jet).

2. Cell islands matching starts from the outermost and proceeds to the innermost hadronic layers. A combination of all cell islands caused by a single particle or a jet is called cone island. The hadronic cell islands are linked together using a single pion MC simulation . The final cone island is obtained using information of the hadronic and electromagnetic layers. The centre of the cone island is calculated as the energy weighted mean of all island cells.

3. The distance-of-the-closest-approach (DCA) is used for matching criterion between track and island positions.

There are three main types of the track-island matching:

- In case when more than one tracks are associated to the cone island, the cone island is treated as jet.

- A cone island is not matched to any track, and is treated as neutral particle.

- In case when a track is not matched to any island, the track is treated as charged particle.

- In the case when the DCA is smaller than the island radius a track is matched to the island. Such case is explained in detailed in this section above.

The CAL information is then used for the first two matching types while for the charged particles the CTD information is used. ZUFO was supposed to combine the information about the cone islands from CAL cells and tracks and create a representation about the final-state of one particle.

3.4 Muon Reconstruction

Muon reconstruction algorithms.
There are different algorithms for muon reconstruction in ZEUS. Most of them are using the BMUON, FMUON, RMUON chambers and MUBAC, CAL. Some algorithms are using all detectors, others only some of them. They are MV, GLOMU, MUFO, MUBAC, MAMMA and others [110].

Muon quality flag.
All muon finders listed above provide various information about muons which is useful for different analysis that use muons. Among other information such type of track which is associated to a muon, it contains an approximate overall muon quality with ranges from 0 to 6. Low muon quality means that a signal to background ratio might be bad, while high muon quality means that the high signal to background ratio is expected [109].

Muon's properties.
Muons are special particles because they interact very little with matter. A muon's energy loss in the calorimeter is almost independent of its momentum. The energy deposit formula is:

$$\frac{dE}{dx} = 1.082 \frac{MeV}{g/cm^2} \tag{3.7}$$

There are four main muon properties which are very useful in this analysis in the sense of signal and background determination:

- Muons from heavy flavour are non-isolated. They are accompanied by hadrons.
- Muons are mainly identified at the muon chambers because of their high penetration power.
- Since the muon is a charged particle it will be associated with a track reconstructed in the tracking detectors.

Monte Carlo muon efficiency corrections. The MC simulation often overestimates the efficiency of the muon chambers. Since the muon efficiency value is very important for the cross section calculation of this analysis, it has to be corrected. This was done in previous analyses by [117, 99]. The idea is to take clean dimuon decays such as $J/\psi \; of \; \psi' \rightarrow \mu^+\mu^-$, Bethe-Heitler processes (Ch. 1.4). The muon efficiency correction function was calculated in other dimuon

analyses, and remains valid for this one as it is [99, 110].
The Monte Carlo correction function applied to correct the muon efficiency, for the particular muons finder "i" depends from the η^μ and p_T^μ, and is defined as data vs Monte Carlo efficiency ratio:

$$f^i_{corr}(\eta^\mu, p_T^\mu) = \frac{\varepsilon^i_{data}(\eta^\mu, p_T^\mu)}{\varepsilon^i_{MC}(\eta^\mu, p_T^\mu)} \tag{3.8}$$

A random number x was used and for each muon was checked if x satisfied the condition:

$$x < f^i_{corr}, \tag{3.9}$$

In case the condition was true, the finder information was reset for the corresponding muon. In this case it is simulated that the muon finder did not tag the muon. Then the finder information was changed. Based on the new finder information, the quality of the muon was recalculated.

Figures 3.2(a) 3.2(b) show the distribution of the different muon finder combinations, which are plotted in the histograms as numbers, before and after the muon efficiency correction respectively.

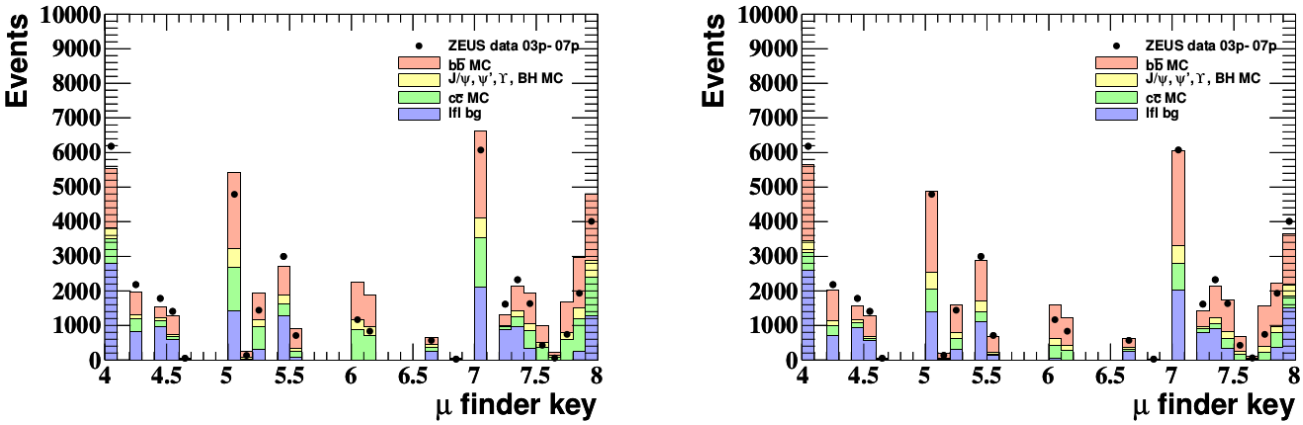

Figure 3.2: Distribution of muon finder combinations for dimuon events left: before and right: after applying the muon efficiency corrections.[99]. The μ finder key description is shown in table 7.2.

The correspondence between names and numbers is provided at the table 7.2. One can see a significant improvement of agreement between data and Monte Carlo events.

3.5 Muon and Dimuon Isolation

An isolation criterion is important in the study of the processes related to muons. This parameter can reveal a lot about the type of process that takes place when considering the selected event. In this analysis the single muon isolation criterion I^μ was calculated as the sum of the transverse momenta of ZUFO objects (ZEUS Unidentified Flow Objects, Sec. 3.3). Muons associated to the ZUFO objects are excluded.

$$I^{\mu} = \sum_{i}^{nZufos} (P_T^{zufo_i}), \text{if Zufo}_i \neq \mu_{id}, \Delta R < 1 \tag{3.10}$$

where $\Delta R = \sqrt{\Delta\eta^2 + \Delta\phi^2}$ between ZUFO objects. For a dimuon system the isolation is defined as:

$$I^{\mu\mu} = \sqrt{I_{\mu_1}^2 + I_{\mu_2}^2}. \tag{3.11}$$

The important aspect is that the dimuons from beauty decays are strongly accompanied by hadronic activity. In this case the dimuon pairs are called non-isolated and these events are considered as signal events. On the other hand dimuons from BH, J/ψ, ψ' , Υ are clearly isolated and can be identified as background events for this analysis.

3.6 Jet Reconstruction

A jet is a narrow cone of hadrons and other particles produced by the hadronization of a quark. A proper understanding of the jet reconstruction algorithm and jet properties is essential knowledge for this analysis. There are many jet finders, but all of them should fulfill the following requirements[111]:

- **Infrared safety.** The results should be insensitive to the emission of very low energy particles.

- **Collinear safety.** The results should be independent of one parton splitting into two partons moving collinearly.

In this analysis jets produced by the k_T object clustering algorithm were used. The k_T clustering algorithm is devoid of such problems. At the ZEUS software it is implemented in the KTCLUS library[112]. The clustering algorithm measures the distance between two objects, i and j, then makes a decision about their merging. The distance d_{ij} is calculated as:

$$d_{ij} = \frac{min(E_{T,i}^2, E_{T,j}^2) \cdot ((\eta_i - \eta_j)^2 + (\phi_i - \phi_j)^2)}{R^2}, \tag{3.12}$$

where E_T is the transverse energy of the i, j objects, and R is the cone radius. The minimal distance of the objects i and j is:

$$d_{min} = min(d_i, d_j) \tag{3.13}$$

where, $d_i = E_{T,i}^2$. There are two possibilities for the next step. In the case $d_{min} = d_{ij}$, the objects i and j are merged, which means that their four-momenta vectors are summed. In the case when $d_{min} = d_i$, the object i is removed from the clustering [111]. In this case, the object i is a final jet.

3.7 Beauty Quark Identification

Decay Length Calculation

The decay length (DL) parameter is one of the most important values in this analysis. It shows the path length value which a particle travels before its decay. The decay length is calculated in the XY plane and thus refers to the transverse path of the particle with respect to the beam line. For events that contain at least one jet, a DL calculation becomes possible. The first step is the calculation of the DL value in the XY plane: L_{XY}. Information about primary and secondary vertex candidates is obtained from the data. Since the position of the vertices is known with some accuracy, one can calculate L_{XY} as a simple vector length between two points such as a primary and secondary vertex. The next step is the definition of the axis with respect to which the decay length projection will be calculated. This axis may be obtained either as the direction of the jet from which the secondary vertex was obtained or as a combined direction of all charged particles which are coming from this secondary vertex (SV). In this analysis the jet axis was used as the direction. Equation 3.16 shows the definition of the cosine between the two vectors:

$$cos\ (\vec{L_{xy}}, \vec{P_T^{axis}}) = \frac{(\vec{L_{xy}} \cdot \vec{P_T})}{|\vec{L_{xy}}| \cdot |\vec{P_T}|}. \tag{3.14}$$

In the DL calculation, the two vectors used are $\vec{L_{xy}}$ and the momentum of the axis vector $\vec{P_T}$. The decay length is defined as:

$$L_{xy}^{axis} = cos\ (\vec{L_{xy}}, \vec{P_T^{axis}}) \cdot |\vec{L_{xy}}| = \frac{(\vec{L_{xy}} \cdot \vec{P_T})}{|\vec{P_T}|}. \tag{3.15}$$

The third formula defines the accuracy of the L_{XY} calculation. It uses covariant matrices from the primary and secondary vertices:

$$dL_{xy}^{axis} = \vec{P_t} \cdot (M_{cov}^{PV} + M_{cov}^{SV}) \cdot \vec{P_t^T}, \tag{3.16}$$

The decay length significance is defined as the ratio of the decay length by its accuracy and is defined with the formula:

$$L_{XY}^{sign} = \frac{L_{xy}^{axis}}{dL_{xy}^{axis}}. \tag{3.17}$$

Figure 3.3 shows an illustration of the decay length calculation procedure. The decay length significance is a powerful parameter which helps to discriminate signal from background events. One of the detector features is that due to the technical limitation of its resolution, a negative value could be obtained for the decay length and its significance. While such a value is not really physical, it can be used as a tool for the background event subtraction. The decay length significance distribution for the light flavour events should be symmetric around 0 while the charm and beauty hadrons have their lifetimes which is reflected in an assymetric DL distribution. This expectation is a useful feature which can be used for the separation of signal

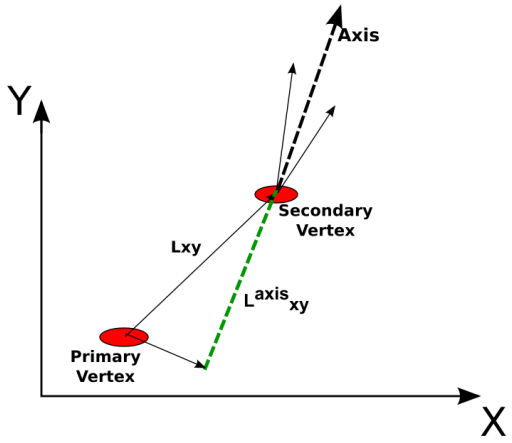

Figure 3.3: Schematic view of shows the primary and secondary vertices and the decay length with its projection on the axis in the XY plane.

from background. The analyses [99, 117] show that the decay length significance distribution in different secondary vertex mass regions has a special behaviour for different MC samples. In this analysis the decay length as well as the decay length significance in the complete secondary vertex mass region are used to determine the contributions of the beauty and charm MC samples.

Chapter 4

Event Selection in ZEUS data

This section describes the data and Monte Carlo samples which have been used in this work for the HERA analysis. The corresponding event selection including the trigger and general selection logic is described in the following sections. The last section contains information about the cuts which were used for background suppression.

4.1 Data and Monte Carlo Samples

In the HERA analysis the *data* collected by the ZEUS detector in 2003-2007 have been used in the ROOT-based Common Ntuple (CN) format [89]. The version of the ntuples is "v02d". The ntuples are based on the overlying routine for analysis ntuple generation (ORANGE) [90]. The experiment energy in the center of mass system is $\sqrt{s} = 318$ GeV for this period. The data for the first two years (2003/2004) were combined into one data sample with positron-proton collision data and with total luminosity equal to 40.6 pb^{-1}. In the years 2005/2006, with electron-proton collisions, the total luminosity is 190.1 pb^{-1}. And for the 06/07 data with positron-proton collisions the luminosity is equal to 145.9 pb^{-1}. The total luminosity is respectively equal to 376.6 pb^{-1}.

The *Monte Carlo* samples (Sec. 1.5) contain simulations of charm, beauty and light flavour events. Photoproduction and DIS processes are hard to describe within a single generator. For this and other reasons beauty and charm events were generated with the PYTHIA [39] (for photoproduction) and RAPGAP [40] (DIS) generators. Inclusive beauty and charm MC samples in DIS are produced from the BGF process. The photoproduction samples were separated into categories with respect to different photon and proton processes. Among them are resolved, direct and excitation processes [39], with a cut on the virtuality of the exchanged photon of $Q^2_{gen} < 1\ GeV^2$ (Sec. 1.2.4).

For the photoproduction MC generation, the *beauty and charm* quark masses were set to $m_b = 4.75$ GeV and $m_c = 1.35$ GeV, respectively.

Beauty and charm events (DIS) are generated with a lower cut on the photon virtuality $Q^2_{gen} > 1\ GeV^2$ and $Q^2_{gen} > 1.5\ GeV^2$. The mass of the heavy flavours was set to $m_b = 4.75$ GeV for the beauty and $m_c = 1.5$ GeV for the charm quark [99].

Beauty quarks have a much lower production rate than charm quarks. In order to get satisfactory statistics for the analysis, the DIS inclusive beauty MC sample was generated with 6-10 times more luminosity with respect to the data statistics. The photoproduction MC inclusive beauty samples were generated with ≈ 15 times more luminosity than the data luminosity. The inclusive charm MC was generated for DIS and PHP with statistics similar to the data.

The generator GRAPE [94] was used to simulate Bethe-Heitler processes. $J/\psi, \psi'$ samples were generated by HERWIG [92]. Υ MC samples were generated by the DIFFVM generator [93]. Multi-heavy-flavour events $c\bar{c}b\bar{b}$ and $b\bar{b}b\bar{b}$ were generated with approximately 10 times larger statistics than the data, and $c\bar{c}c\bar{c}$ events with only two times more statistics. For this kind of samples no cuts were applied on generator level and the MG2ZEUS, FORMOZA [95] generators were used.

4.2 Trigger Selection

In this analysis a combination of most of the triggers listed in the table 4.1 was applied. At least one of those third-level triggers (TLT) were required for the event selection. There are also first and second level triggers (Sec. 2.3.7) which are partially required as input to the TLT. They usually have weaker restrictions than the TLT triggers. The third level triggers contain the first and second level triggers and in most of cases have more stringent restrictions to distinguish a certain physical process. The list of possible triggers for this analysis was obtained from the previous analysis [99] and is listed here:

HFL01 : Open charm and beauty on PHP	**HFL31** : Isolated $\mu\mu$ from MV
HFL05 : Inclusive di-jet	**HFL32** : Inclusive double-tagged $\mu\mu$
HFL06 : Dijets in DIS	**DIS03** : Medium Q^2 DIS
HFL13 : Inclusive semi-leptonic μ	**HPP31/SPP02/SPP09** : Inclusive low Q^2 DIS
HFL14 : Inclusive μ in DIS	**EXO11/12** : Barrel/rear μ
HFL16 : Inclusive μin BAC	**MUO03** : Semi-isolated barrel/rear μ
HFL25 : μ + dijets	**MUO01/02/04-09** : forward μ
HFL27 : MVD inclusive trigger	**MUO10-14** : μ in BAC.
HFL30 : J/ψ candidate	

Table 4.1: A trigger description which contain all triggers which might be used in this analysis [99, 117].

4.3 General Event Selection

DIS electron selection

To select an electron, SINISTRA [96] as a part of the ZEUS reconstruction software has been used. SINISTRA is using the transverse and longitudinal energy profile, analyses it and as output gives the probability that the chosen electromagnetic cluster was created by an electron. Since this program is based on a neural network package is was trained on MC events, where one can absolutely know the electron information and the results of training. In those cases where an electron passes the requirements it is considered as an electron candidate. For the electron selection the following requirements were applied:

- SINISTRA finder probability: $P_{sinistra} > 90\%$
- inelasticity : $y \in [0.05, 0.7]$
- photon virtuality: $Q^2 > 4\ GeV^2$
- DIS selection criterion: E - $p_z \in [40, 60]$ GeV
- energy deposit in EMC : $E_e > 10$ GeV

The hadronic transverse energy

In some cases , the electron is scattered to a region which is very close to the beam line. In the case where a DIS electron was found, one should remove its impact on the hadronic transverse energy calculations. The transverse energy is the sum of all deposits in the calorimeter multiplied by $sin(\theta)$. To reject proton-remnant effects this sum is calculated only for angles $> 10^0$. The hadronic transverse energy is thus defined as:

$$E_T = \sum_{i,\theta_i} (E_i \cdot sin\theta_i), \text{ for } \theta > 10^0, \quad \text{in the case where an electron was found: } E_T = E_T - E_T^e. \tag{4.1}$$

The object for this analysis is a $b\bar{b}$ pair. It has a large mass which causes a large amount of deposits to the detector. This point can be helpful to suppress charm and false-muon background. In this analysis a cut on the hadronic transverse energy was used as:

$$E_T \geq 8 \text{ GeV}. \tag{4.2}$$

4.4 Dimuon Selection

The main process studied in this analysis is the $ep \to e' b\bar{b} X \to e' \mu\mu X$ process. For this reason a dimuon selection is one of the most important tasks. The general muon selection requirement includes transverse momentum and energy cuts. The dimuon selection obviously requires two muon candidates. A cut on the total transverse energy of the dimuon pair has been applied

which depends on the muon pair mass:

$$\begin{aligned} 0.1 < \frac{(p^T_{\mu 1} + p^T_{\mu 2})}{E_T} < 0.5 \text{ for } m^{\mu\mu}_{inv} < 4\ GeV \\ 0.1 < \frac{(p^T_{\mu 1} + p^T_{\mu 2})}{E_T} < 0.7 \text{ for } m^{\mu\mu}_{inv} \geq 4\ GeV \end{aligned} \tag{4.3}$$

Very high or low hadronic activity is most likely an indication for either false muon (see 5.3) background, or Bethe-Heitler or quarkonia events. This cut efficiently removes background events from Bethe-Heitler and heavy quarkonia but has almost no effect on the beauty contribution. Another cut applied on the transverse momentum depends on the quality of the muon:

$$\begin{aligned} \mu_{quality} = 4 : p^{\mu}_T \geq 1.5\ GeV \\ \mu_{quality} \geq 5 : p^{\mu}_T \geq 0.75\ GeV \end{aligned} \tag{4.4}$$

To thoroughly understand the processes that are going on in the event one needs to clearly know how dimuon pairs were produced. A muon from a beauty event can be obtained from the direct or cascade decay of a b or $\bar{b}$ quark (Sec. 1.4). Those processes (fig. 4.1) could be separated through dimuon pair invariant mass. Dimuon pairs with mass < than 4 GeV come predominantly from a single bottom quark 4.1(d). In the case where the invariant mass is larger than 4 GeV, most likely the dimuon pair comes from the direct $b\bar{b}$ decays. Schematic explanation of those cases are shown on the figure (4.1).

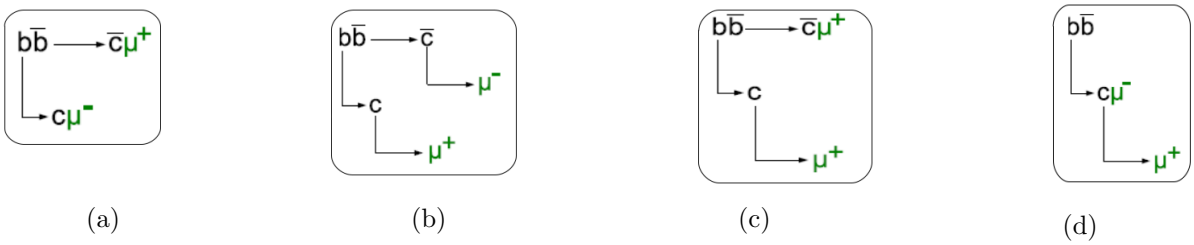

(a) (b) (c) (d)

Figure 4.1: Muon pair sources in $e^{\pm}p$ collisions.

An additional separation criterion occurs by looking at the charge of the dimuon pair. In the case of the cascade decay of one of the beauty quark pair, the muons will be produced with an electric charge of the same sign. Those di-muons are called like-sign dimuon pair. Otherwise, the di-muons are called unlike-sign. In this analysis we are interested in unlike-sign dimuon pairs as a source for the beauty signal events identification, but information about like-sign pairs is very useful to control the background and to provide a background estimation which will be explained in the next section.
In the case of high dimuon invariant mass the muons come from different b quarks. But in this case, unlike-sign muons might also arise from $c\bar{c}$, BH, Υ and false muon background. In turn, while like-sign high mass muon pairs most likely come from different b quarks, they contain a large fraction of false muon background.

Background Suppression Cuts

To suppress background events a few basic cuts were applied. For the light-flavour suppression a cut on minimal dimuon invariant mass is used:

$$m_{inv} > 1.5\ GeV. \tag{4.5}$$

This also suppress events in which different tracks are associated to information in the muon system arising from a single muon. A cut on the pseudorapidity difference between the two muons is used to suppress light flavour and Bethe-Heitler background events, in which the muons have a high difference in pseudorapidity.

$$|\eta^{\mu 1} - \eta^{\mu 2}| < 3.0. \tag{4.6}$$

In addition, for some of the muon candidates the momentum was not well measured. To take this into account a cut which uses the transverse momentum of muons was used:

$$\frac{(|p_T^{\mu 1} - p_T^{\mu 2}|)}{(|p_T^{\mu 1} + p_T^{\mu 2}|)} \leq 0.7. \tag{4.7}$$

To reject muons from cosmic rays, a timing cut with respect to the nominal collision time was applied. If the time difference is more than 10 ns the event are rejected.

4.5 List of all cuts

In this section all cuts which were used in this analysis are summarised. The cuts can naturally be divided into two main groups: general event and muon selection and background suppression cuts.

Muon selection cut list:

- Number of muons ≥ 2
- di-muon invariant mass, $m^{\mu\mu}$ lower limit is 1.5 GeV
- asymmetry cut: $\frac{(p_T^{\mu_1} - p_T^{\mu_2})}{(p_T^{\mu 1} + p_T^{\mu 2})} \leq 0.7$
- Muon p_T/E_T cuts:
  $0.1 < \frac{(p_{\mu 1}^T + p_{\mu 2}^T)}{E_T} < 0.5$ for $m_{inv}^{\mu\mu} < 4GeV$
  $0.1 < \frac{(p_{\mu 1}^T + p_{\mu 2}^T)}{E_T} < 0.7$ for $m_{inv}^{\mu\mu} \geq 4GeV$
- Muons η cut: $|\eta^{\mu_1} - \eta^{\mu_2}| < 3.0$
- Muon P_T cuts:
  $\mu_{quality} = 4 : p_T^{\mu} \geq 1.5$ GeV
  $\mu_{quality} \geq 5 : p_T^{\mu} \geq 0.75$ GeV

In this analysis events are selected with two muons. The muon η difference cut removes events which contain very forward and very backward muons. A very significant fraction of such events are from light flavour or Bethe-Heitler background. The cut on the muon transverse momentum strongly depends from the muon quality and was applied with different values for the different muon quality candidates.

General event & background suppression cuts:
General cuts which were applied to all events of this analysis are:

- $E_T^{CAL} \geq 8$ GeV
- Cosmic particles (mostly muons) cuts:
  – Calorimeter time : $t < 10ns$
  – BAC energy : $E_{BAC} < 100$ GeV, in case of muon particle: $N_{BAC} < 15$GeV
  – Difference between angles of two registrated muons:
  $|\pi - |\phi_{\mu_1} - \phi_{\mu_2}|| < \pi/200$ and $|\pi - (\theta_{\mu_1} + \theta_{\mu_2})| < \pi/200$

The transverse energy cut is used for charm and false-muon background suppression because $m(b\bar{b}) \geq 10\ GeV$. Cosmic particle cuts are used to reject cosmic particles. In the case that the event passed the cosmic cuts, this event is rejected. The difference between angles of two registrated muons is a powerful tool, since cosmic track on the first glance, looks like two muons which are going back-to-back from the same vertex. The ϕ and θ angle cuts help to recognize such events.

Vertex cuts:
In addition to the cuts above, vertex cuts are used in this analysis: To reject bad quality vertices a cylinder like cut was used: $\sqrt{x_{vtx}^2 + y_{vtx}^2} < 3$ cm and $|z_{vtx}| < 30$ cm, where the $x_{vtx}, y_{vtx}, z_{vtx}$ are vertex candidate position coordinates. The maximal distance of the vertex from the nominal vertex point in the xy plane is required to be less than 3 cm.

Chapter 5

Beauty Signal Determination

Section 3.7 explains the decay length distribution calculation algorithm. This method is used to get the decay length distribution (Fig. 5.4). The figure shows each MC sample scaled to the data luminosity according to its MC cross section. The scale factors are applied for the beauty (brown color), charm (green) samples and for the heavy quarkonia and Bethe-Heitler samples which are marked with yellow collor. The "standard" procedure repeats the previous analysis to get the checkpoint for further improvements. The "standard" charmonium and Bethe-Heitler factors are explained in Section 5.2. Continuing the analysis using secondary vertices the beauty and charm scale factors are obtained from the fit procedure which is described in this section.

5.1 General Measurement Procedure

In this analysis beauty quark production is measured via the process $ep \to e'b\bar{b}X \to e'\mu\mu X$. The beauty quark cross section measurement needs a clear understanding of the beauty and background contributions in the dimuon sample. The next sections will explain in more detail how the background contributions were estimated. As stated in Section 1.3, there are a few possible processes which may contribute to the beauty signal. They are the direct decay of both b and $\bar{b}$ quarks and cascade b-quark decays, cascade decay of both b and $\bar{b}$ quarks and a combination where one b-quark makes a direct decay while the other makes a cascade decay (Fig. 4.1).

In the cascade decay process of a single b-quark, the reaction $b \to cX \to s\mu X'$ takes place. In this case unlike-sign muon pairs are produced (Fig. 4.1(d)). In the case of direct decays from both beauty quarks (Fig. 4.1(a)) the $b, \bar{b} \to c\mu X$ process take place. In this case unlike-sign muon pairs are produced except if one of two b-quarks has oscillated (see Sec. 1.4.1). Because of the reaction topology (in most case muons from the different beauty quarks are produced in different hemispheres) the invariant mass of such a dimuon pair will be more than 4 GeV. Both beauty quarks can decay into charm quarks which decay and produce unlike-sign muon pairs (Fig. 4.1(b)). In some case there will be the combination of two processes where one of the quarks decay into charm quarks which produce a muon, and a second beauty quark decays directly to a muon. In this case like-sign muon pairs are produced (Fig. 4.1(c)), except case of

$B^0 - \bar{B}^0$ oscillation.

There are a few possibe background contribution which create backround unlike-sign dimuon pairs. The most obvious is the decay of both c and $\bar{c}$ quarks of a $c\bar{c}$ pair. This process will produce an unlike-sign dimuon pair with muons in different hemispheres. The charm quark contribution is suppressed with cuts listed in the section 4.5. Heavy quarkonia decays create background events for this analysis with unlike-sign muon pairs. There are $J/\psi, \psi', \Upsilon$ events which create background dimuon pairs as well as Bethe-Heitler events. In such cases the muons are not accompanied by hadronic activity.

5.2 Normalisation of Heavy Quarkonia and Bethe-Heitler background

The dimuon isolation criterion, $I^{\mu\mu}$, is different for the different mass regions. In the case of the $J/\psi, \psi'$ peak mass ranges $[2.9, 3.25]$ and $[3.6, 3.75]$, $I^{\mu\mu} > 2\ GeV$. Otherwise, $I^{\mu\mu} > 0.25\ GeV$. For this analysis the dimuon isolation criterion is quite significant. The isolated, unlike-sign distribution mainly contains events with J/ψ and ψ' candidates (Fig. 5.1). This allows to extract scale factors to normalise their contributions using MC simulation and data distributions. The MC scale factor for J/ψ and ψ' is obtained from the isolated unlike-sign part. With the isolation criteria shown in Sec. 3.5 the unlike data samples of the low and high

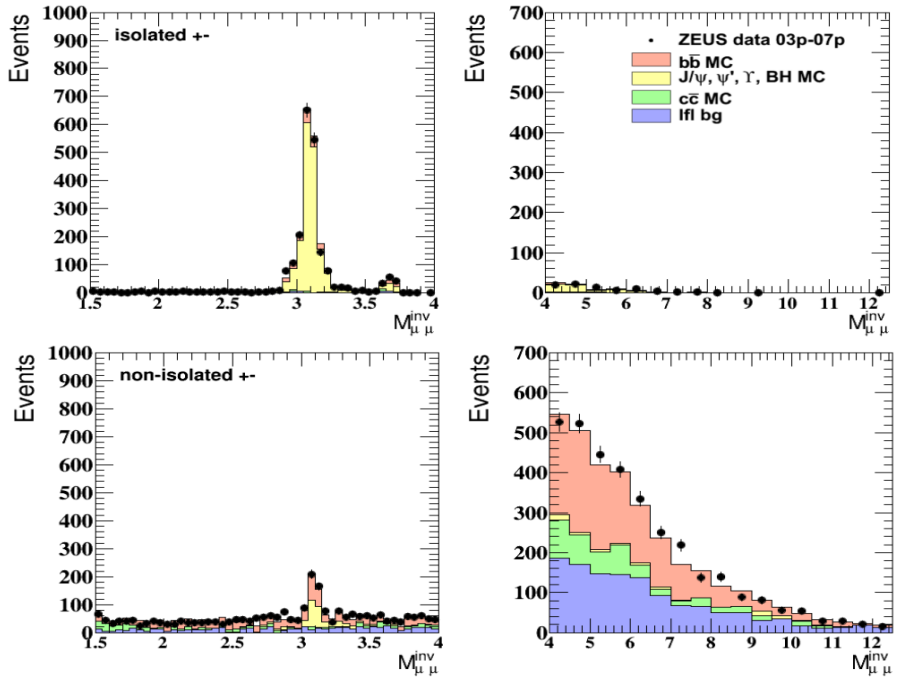

Figure 5.1: Unlike-sign dimuon invariant mass distributions. The top part is related to isolated dimuons for the low(left) and high(right) mass regions. The bottom part shows the invariant mass behaviour of the non-isolated dimuon pairs. Four different colors show the MC contributions from the beauty (brown), heavy quarkonia (yellow), charm (green) and light flavour. Black dots describe the data.

mass regions were separated into two samples with isolated and non-isolated dimuons. The

top part shows the unlike-sign isolated dimuon pair invariant mass distribution. The bottom part of the figure shows the dimuon invariant mass distribution with non-isolated unlike-sign dimuon pairs.

5.3 Light Flavour Background Determination

At the ZEUS experiment light flavour background was not simulated. Because of this special techniques were used to take into account the light flavour contribution. In the "traditional" ([99]) analysis, the light flavour background was obtained with the so-called substruction method. Two hypotheses have been made. The first assumption is that only beauty-quark decays can produce real like-sign muon pairs and is based on the Standard Model. The second one is that in the light flavour background like-sign and unlike-sign muon pairs have no charge correlation. The second assumption was checked on a dimuon sample with a lower cut on muon quality in a previous analysis [99]. The like-sign dimuon contribution from charm quarks is negligible. The light flavour background which produces false muons contributes to both the like- and unlike-sign muon pairs. The like-sign data sample contains only the beauty and light flavour events. The like-sign light flavour background can be extracted from the data by subtracting the predicted beauty contribution. In turn the beauty scale factor was obtained from the unlike-sign sample, where the unlike-sign light flavour background is the reflection of the like-sign. The second hypothesis was checked on the like-sign data sample with GMUON

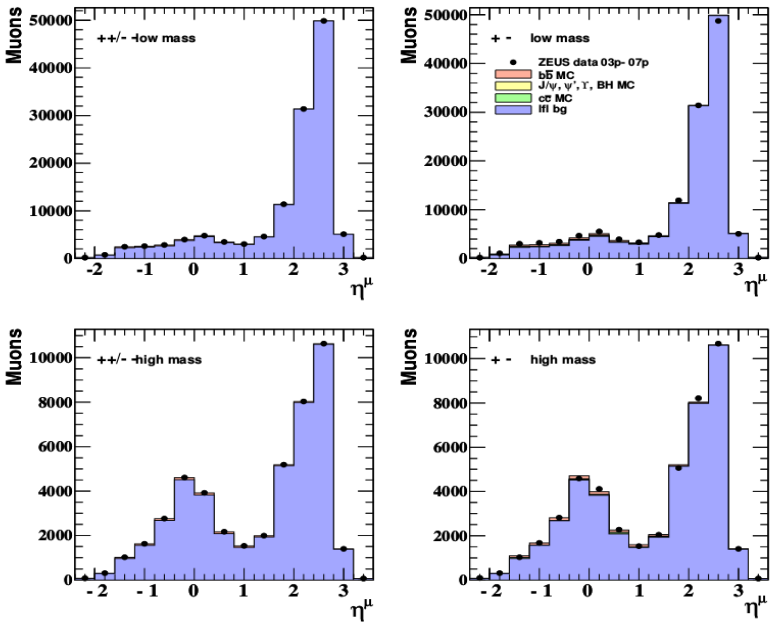

Figure 5.2: Muon pseudorapidity η^{μ} for like- (left) and unlike-sign (right) dimuon in the low- (top) and high-mass (bottom) range. The figure is taken from [99].

quality greater than 0. Figure (5.2, left) shows the like-sign η^{μ} distribution which is well described by data and mainly consist of light flavour events. The contribution from beauty, charm, Bethe-Heitler and heavy quarkonia events is very small and almost negligible. The same shape

of the light flavour background was then applied to the unlike-sign data, and was used as its light flavour background with small corrections for the low mass ($C_{lm} = 1.04$) and for the high mass region ($C_{hm} = 1.01$). These factors are also applied to the current analysis.

5.4 Charm background Normalisation

Due to the low statistic of the $c\bar{c}$ events, in the "standard" analysis the charm scale factor which normalises the charm MC background to data was obtained from another process. A suitable process with a similar topology, is the process with $D^*\mu$ events.

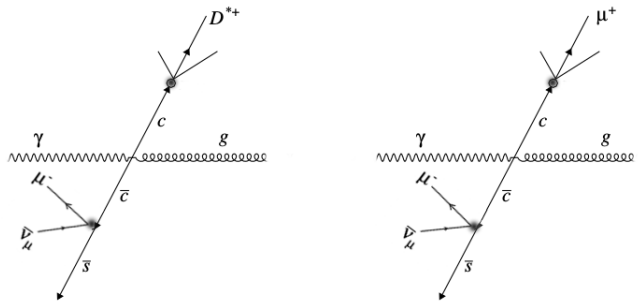

Figure 5.3: Illustration of the two similar topologies of $c\bar{c}$ events. The sketch shows the topology of events with the production of $D^*\mu$ (left) and $\mu\mu$ (right) pairs.

The scale factor for the charm contribution was obtained from the analysis [99], and was used in the "standard" part of this analysis, before the decay length significance fit procedure.

$$S^{MC}_{charm} = 1.37 \pm 0.20 \tag{5.1}$$

Fig.5.3 clearly shows the similarity of the topology of two processes.

5.5 Beauty MC Normalisation

In the case when all important control data distributions are in a good agreement with their MC prediction one can calculate the beauty signal fraction using MC and data distributions. As shown in Sec. 5.3, the light flavour normalisation is slightly different for the low and high mass distributions. Since the difference is not large, a detailed formula description will be provided with a single light flavour normalisation coefficient - C (while C_{lm} and C_{hm} are the coefficients defined for the low- and high-mass regions (see 5.3)). To make the following formula a bit more clearly defined, N_{const} is defined as:

$$N_{const} = N^u_{const} = N_{c\bar{c}} + N_{VM} + N_{BH}. \tag{5.2}$$

The general formula which takes into account high and low mass regions and shows the relation between the data and MC contributions is the following:

$$N^u_{data} = N^u_b \cdot S^{MC}_b + N_{const} + C \cdot N^l_{data} - S^{MC}_b \cdot C \cdot N^l_b, \tag{5.3}$$

where the formulas define the mapping between the data and Monte Carlo part:

$$\begin{aligned} N^u_{data} &= N^u_b \cdot S^{MC}_b + N^u_{const} + N^u_{lfl}, \\ N^l_{data} &= N^l_b \cdot S^{MC}_b + N^l_{lfl}, \\ N^u_{lfl} &= N^l_{lfl} \cdot C, \end{aligned} \tag{5.4}$$

where S^{MC}_b is the normalisation factor for beauty events in the data relative to the MC expectation, and the right part of the formulas 5.4 is related to the MC contributions. The N_{data} value is related to the number of events extracted from the data, for the unlike- (u) and the like-sign (l) data samples. N^u_b is the number of events from the beauty unlike-sign MC dimuon sample, while N^l_b is related to the like-sign dimuon contribution. The N^u_{lfl} and N^l_{lfl} values specify the number of events of the unlike- and like-sign light flavour contribution. From the formula (5.3) one can extract the final equation for the beauty MC scale factor:

$$S^{MC}_b = \frac{N^u_{data} - C \cdot N^l_{data} - N_{const}}{N^u_{b,MC} - C \cdot N^l_{b,MC}}. \tag{5.5}$$

Following such a conversion, one can see that to account for the small differences between the unlike and like-sign samples for the low and high mass regions separately, the equation (5.5) looks like:

$$S^{MC}_{b,lm+hm} = \frac{N^u_{data} - C_{lm} \cdot N^l_{data,lm} - C_{hm} \cdot N^l_{data,hm} - N_{const}}{N^u_{b,MC} - C_{lm} \cdot N^l_{b,MC,lm} - C_{hm} \cdot N^l_{b,MC,hm}} = 1.85 \pm 0.06 \tag{5.6}$$

Fig.(5.4) shows that the left part of the data distribution is underestimated by the MC. In addition, the light flavour contribution is not symmetric. This shows the possibility for further improvements of the light flavour contribution, charm and beauty normalisation. In this analsis this is done with a fit of the decay length significance distribution.

5.6 Control distributions

With the contributions from different properly normalised MC samples the next step is to check some control distributions.

Figure 5.5 shows the dimuon mass distribution for both the isolated and non-isolated dimuon samples. The plots on this figure are separated by the dimuon sign and invariant mass range (cut at 4 GeV/c^2). The two left plots show the low mass region, while the two right plots describe the high mass region. The top and bottom distributions show the separation into like-

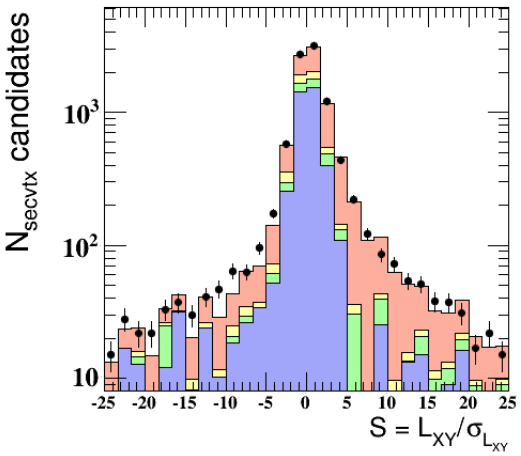

Figure 5.4: Decay length distribution for both the low and high mass regions and for both like- and unlike-sign dimuon events. The brown color related to the beauty part, yellow color shows a Bethe Heitler and heavy quarkonia contribution, while green and blue describe charm and light flavor contributions respectively.

and unlike-sign dimuon combinations. The heavy quarkonia shown in yellow mainly dominate at the low mass region and make a relatively small contribution at the high mass region. The blue color shows the light flavour contribution. With green and brown colors the charm and beauty contributions are shown respectively. The black dots show the data distribution with their statistical uncertainty. In the unlike-sign dimuon low mass distribution (top left) of the figure, the main contribution comes from the heavy quarkonia sample. The unlike-sign dimuon high mass distribution (top right) essentially contains beauty events, making this region particularly interesting in this analysis. Since the light flavour contribution was extracted from the like-sign dimuon data and the beauty contribution (see Sec. 5.3), the two bottom plots contain only light flavour and beauty MC contributions and ideally coincide with the distribution of the data.

Figure 5.6 shows event properties such as the quantity $E - p_z$ (left) which is related to the kinematic quantity W (Sec. 1.2.1) and the $log_{10}(Q^2)$ (right). Since for the DIS and photoproduction contributions the same scaling factors for the signal and background contribution were used, the Q^2 distribution was used to check their contributions. The last 4 bins contain events from the DIS process. The first bin mainly contain PHP events while the second bin contains events wich did not pass the electron requirements for the DIS process.

Figure 5.7(b) shows some discrepancies in the low muon p_t and negative η regions. By definition, such differences mainly comes from the unlike-sign dimuon part.

Figure 5.8 shows the $\eta^{\mu\mu}$ (a) and $P_T^{\mu\mu}$ (b) distribution for dimuon events in the low and high mass regions for unlike sign and the non-isolated subsample.

This subsection shows a repetition of the previous analysis performed with same selection criteria and data samples. In this study technical improvements were made with respect to the previous analysis. Because of no possibility to check step by step the analysis process some differences to the previous results appeared in the control distributions. In the same time,

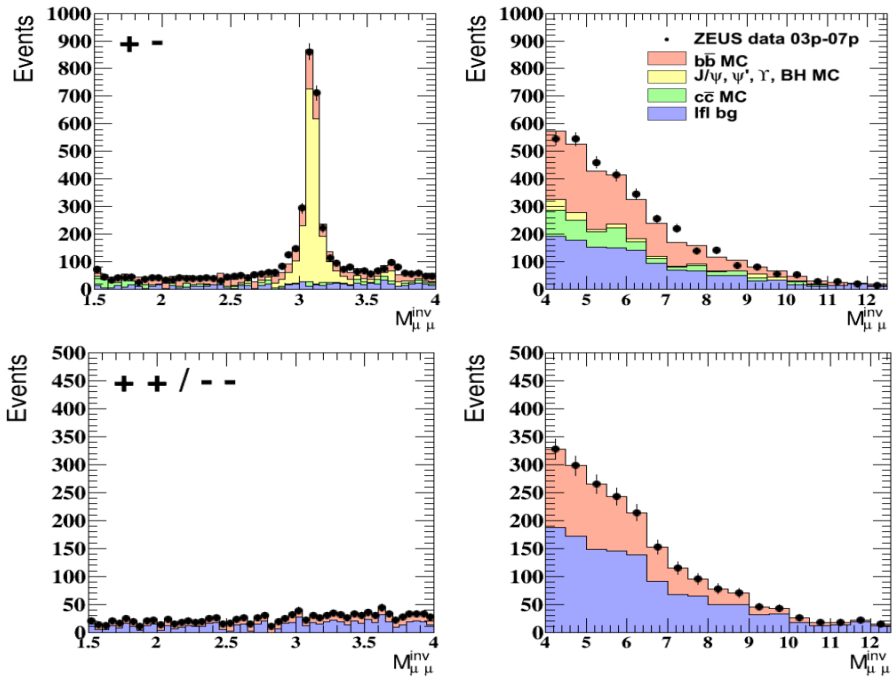

Figure 5.5: Like- and unlike-sign dimuon invariant mass distributions. The top part is related to unlike-sign dimuons for the low(left) and high(right) mass regions. The bottom part shows the invariant mass behaviour of the like-sign dimuon pairs. Four different colors show MC contributions from the beauty (brown), heavy quarkonia (yellow), charm (green) and light flavour. Black dots describe data.

the discrepancies are small and are covered by statistical uncertainties. In this study all control distributions show a good agreement between the data and MC, while the decay length distribution shows that further improvements might be needed.

5.7 The fit procedure

Starting from this section improvements are implemented via the decay length significance fit. The decay length significance fit may be considered as a separate cross check for the beauty and charm mormalisation, or as a mix of both, since this method uses formula (5.5) to extract the light flavour contribution.

In this section, the decay length significance fit procedure will be explained. The input for this procedure consists of the data sample, and all MC samples. The light flavour background shape was obtained from like-sign dimuon data and beauty MC samples with the "standard" method used in the previous analyses and described in the Sec. 5.3. The output of the fit will give us new scale factors for the beauty and charm MC samples. Both mass regions (the low and high) were used in the fit simultaneously.

The decay length calculation requires at least one jet in the event. It also has additional requirements on the secondary vertex candidate quality which are related to the secondary vertex candidate coordinates (Sec. 4.5). Thus, the decay length distribution is obtained from a subset of the original events obtained with the original list of cuts (Sec. 4.5). This data set is $\approx$ 20% smaller than the original one (without a jet requirement). The fit procedure

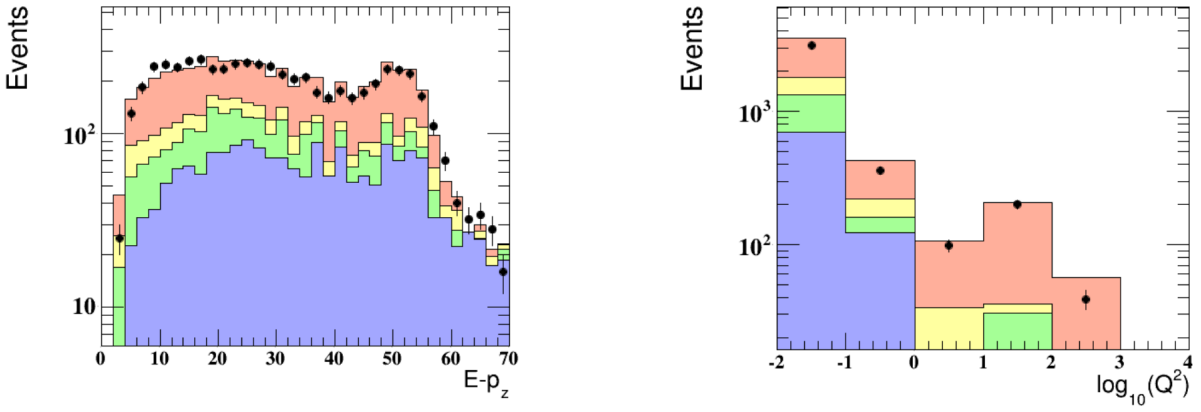

(a) (b)

Figure 5.6: The distribution for Q^2 in the logarithmic scale (right) and $E-p_z$ (left) from unlike-sign, non-isolated dimuons for both low and high mass regions. Each event contains two muons.

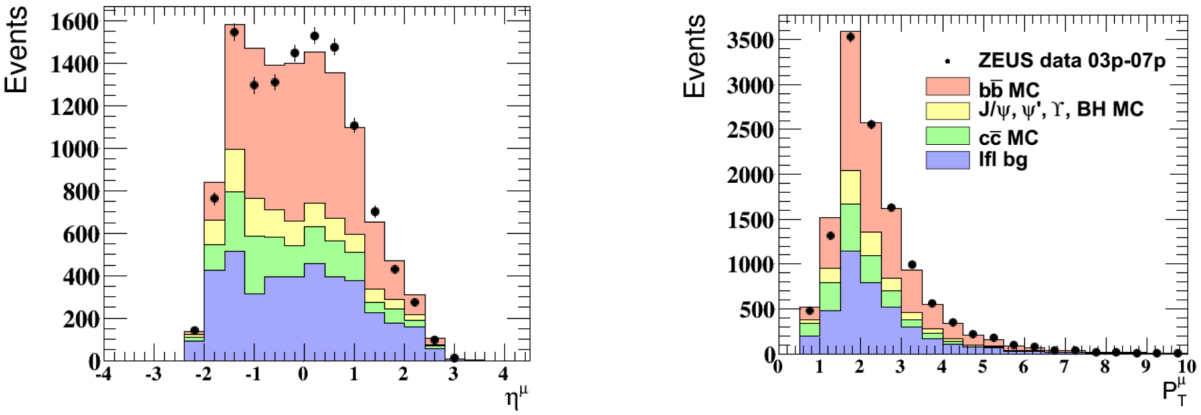

(a) (b)

Figure 5.7: The pseudorapidity (left) and the muon transverse momentum p_T^μ from unlike-sign, non-isolated dimuons for both low and high mass regions.

	N_{data}	$N_{b\bar{b}}$	$N_{c\bar{c}}$	$N_{BH,heavyq\bar{q}}$	N_{lfl}
no jet req.	11587	5169	3024	2457	3509
with > 1jet req.	8949	4275	2258	1281	3039

Table 5.1: Number of events from the different dimuon samples.

has two additional physical constraints. While for the beauty MC sample one can observe a strong asymmetry which is related to the b-hadron decay length there is no reason to have an asymmetric distribution for the light flavor contribution. The light flavour contribution can be controlled by the beauty contribution. This is used to make an additional constraint to the χ^2 fit. Due to low light flavour contribution and its correlation with the beauty MC sample this constraint makes only a few percent difference to the fitted parameters. For statistical reasons, the decay length distribution was organised into ten bins (Fig. 5.9(a)) for both the low and high mass regions, unlike-sign sample (Figure 5.9).

Figure 5.4 shows that the negative decay length significance of the MC distribution is signif-

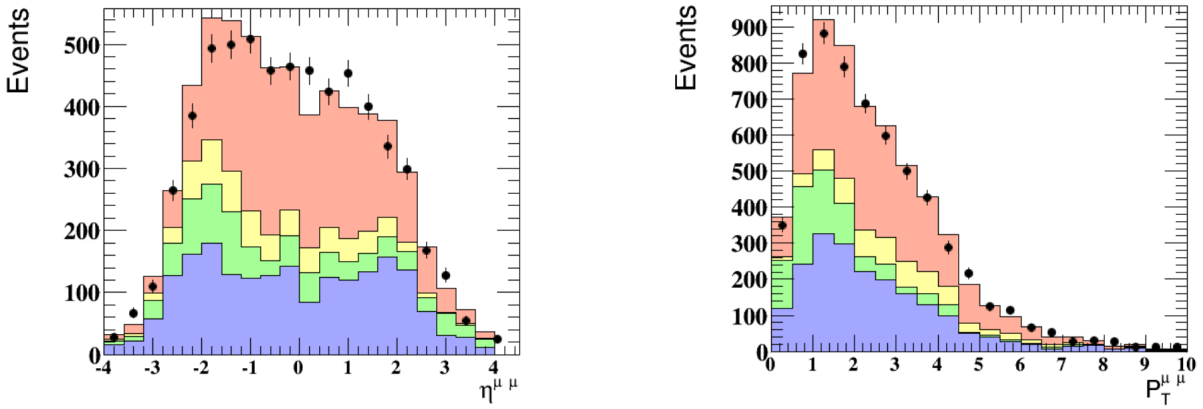

(a) (b)

Figure 5.8: The dimuon pseudorapidity, $\eta^{\mu\mu}$ (left) and the transverse momentum $p_T^{\mu\mu}$ from unlike-sign, non-isolated dimuons for both low and high mass regions.

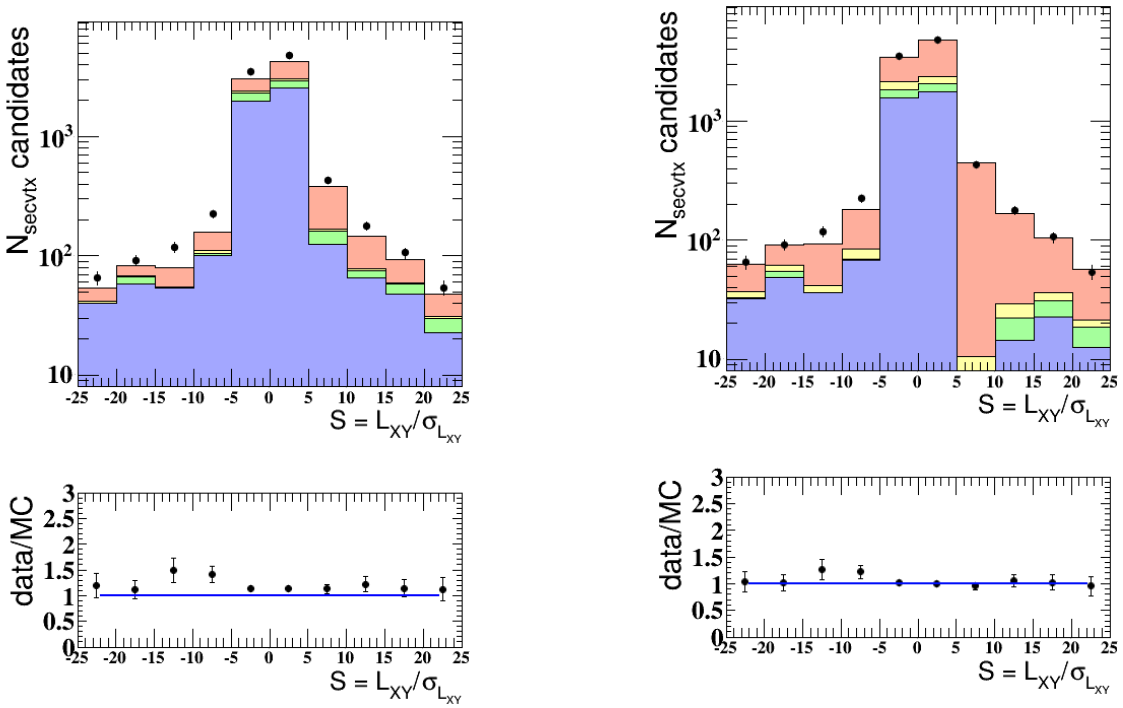

(a) (b)

Figure 5.9: The DL significance distribution. The plot (a) shows the data vs the MC samples before the fit. The plot (b) shows the result of the fit procedure. The brown color related to the beauty part, yellow color shows a Bethe Heitler and heavy quarkonia contribution, while green and blue describe charm and light flavor contributions.

icantly underestimated. The fit function uses two parameters which describe the correction scale factor for $b\bar{b}$ ($P_1 = S_{b\bar{b}}$) and for $c\bar{c}$ (P_2). For the fit, the light flavour coefficients $C_{lm} = 4\%$ and $C_{hm} = 1\%$ were used for the low and high mass regions respectively (Sec. 5.3). The fit procedure uses χ^2 minimisation and minimises the difference (ΔN_i) between the data and MC in each bin of the decay length significance distribution for the low and high mass regions simultaneously. With the following equation (5.3) for each of the bins the difference between

MC and data is defined in the way:

$$\Delta N_i = N^u_{data} - C \cdot N^l_{data} - S_{b\bar{b}} \cdot (N^u_{b,MC} - C \cdot N^l_{b,MC}) - S_{c\bar{c}} \cdot N_{c\bar{c}} - N_{BH+J/\psi+\psi+Y} \tag{5.7}$$

where the C value depends on the dimuon invariant mass region as described above, and the parameters $S_{b\bar{b}}, S_{c\bar{c}}$ are new scale factors for the corresponding beauty and charm MC samples.

$$\begin{aligned} \chi^2 &= \sum_{i=1}^{10} \left(\frac{\Delta N_i}{\sigma(\Delta N_i)} \right)^2, \\ \chi^2_{tot} &= \sum_{i=1}^{10} \left(\frac{\Delta N_i}{\sigma(\Delta N_i)} \right)^2 + \left(\frac{P_{c\bar{c}} - 1.37}{0.2} \right)^2 + \left(\frac{P_{b\bar{b}} - 1.7}{0.5} \right)^2. \end{aligned} \tag{5.8}$$

A second constraint restrict the charm and beauty scale factors to be within their approximate sigma range obtained from previous analysis using formula (5.8). As the result of the fit procedure, a set of the new scale factors was obtained from the fit with $\chi^2 = 1.05$:

$$\begin{aligned} S_{b\bar{b}} &= 2.07 \pm 0.08, \\ S_{c\bar{c}} &= 1.12 \pm 0.14, \end{aligned} \tag{5.9}$$

From the fit results one can say that indeed the beauty contribution was underestimated refering to the "standard" method of the beauty scale determination [99], where the beauty normalisation coeficients was determined as: $S_{b\bar{b}} = 1.85 \pm 0.06$ (Sec. 5.5). The fit procedure is performed as an upgrade to the method stated in the previous analysis with the formula (5.5). The light flavor contribution is extracted with the "standard" method. Charm and beauty contributions are obtained from the fit. The $J/\psi, \psi', BH, \Upsilon$ scale is obtained from the dimuon isolated invariant mass distribution. Both MC scale factors have an impact into the total and differential cross section measurements. It has to be stated that the statistics used in this method is different because of the additional cuts which are related to secondary vertex candidates and jets. The obtained coefficients after the fit procedure (except the one for beauty, which is reextracted bin-by-bin from the data) are used later as the new normalization coefficients for the corresponding MC samples.

Figure (5.10) shows the final decay length distribution with includes the scales factors from the fit. The left plot contains the contribution from both the unlike- and like-sign distributions for both the low- and high mass regions. The right plot is the same distribution but contains only the unlike-sign contribution same to the Fig. (5.9(b)) where each bin has been splited into these bins in order to show finer details of the distribution. The decay length significance distribution could be divided into more bins also for the fit and this may increase the accuracy of the fit procedure, but then the low statistics for some bins will require a different fit procedure.

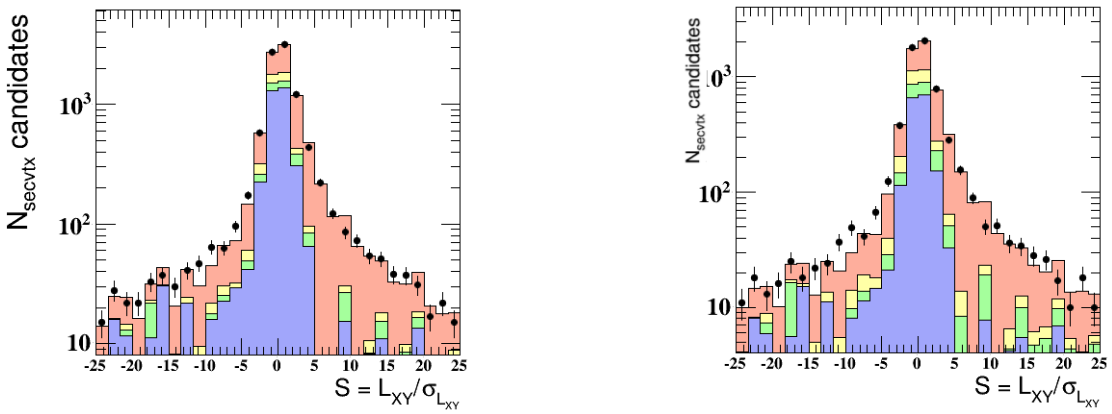

Figure 5.10: The DL significance distribution after the fit procedure with higher number of bins with a jet requirement. Both plots show low and high mass regions. The left plot shows distribution for both like- and unlike-sign dimuon pairs contribution, while the right plot shows decay length distribution only for the unlike-sign part.

5.7.1 Control distributions with the fit results included

The beauty, charm and other MC sample normalisation coefficients were checked with the muon and dimuon distributions. In this subsection different kinematic variable distributions are shown together with variable distributions which are related to the secondary vertices. The

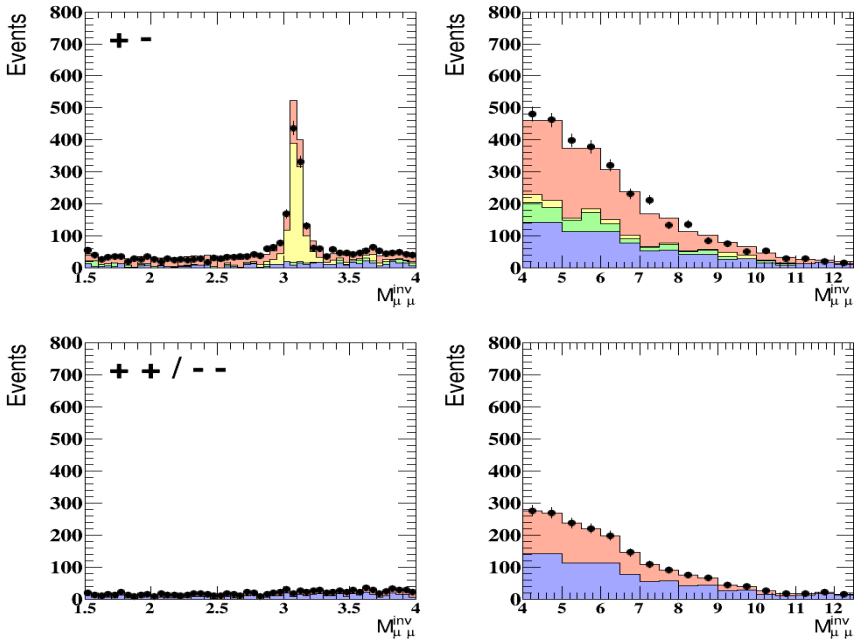

Figure 5.11: Like- and unlike-sign dimuon invariant mass distributions with a jet requirement. The top part is related to unlike-sign dimuons for the low(left) and high(right) mass regions. The bottom part shows the invariant mass behaviour of the like-sign dimuon pairs. Four different colors show the MC contributions from the beauty (brown), heavy quarkonia (yellow), charm (green) and light flavour. Black dots describe the data.

contributions of this section contain dimuon events which are accompanied with at least one jet. This section shows control distributions with the new charm and beauty scale factors (5.9) obtained from the fit procedure. Figure (5.11) shows the dimuon invariant mass distributions

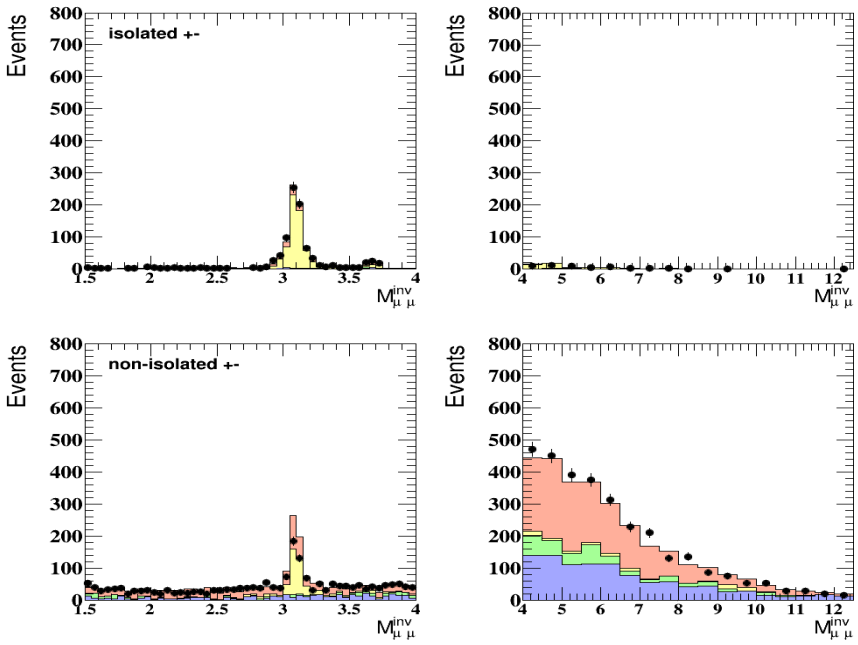

Figure 5.12: Unlike-sign dimuon invariant mass distributions. The top part is related to isolated dimuons for the low(left) and high(right) mass regions. The bottom part shows the invariant mass behaviour of the non-isolated dimuon pairs.

separated by charge. In case of reduced data sample beause of jet requirement, invariant mass distribution shows that unlike sign dimuons are overestimated by the MC. This might be because of overestimation of the beauty contribution.

Event control distributions.

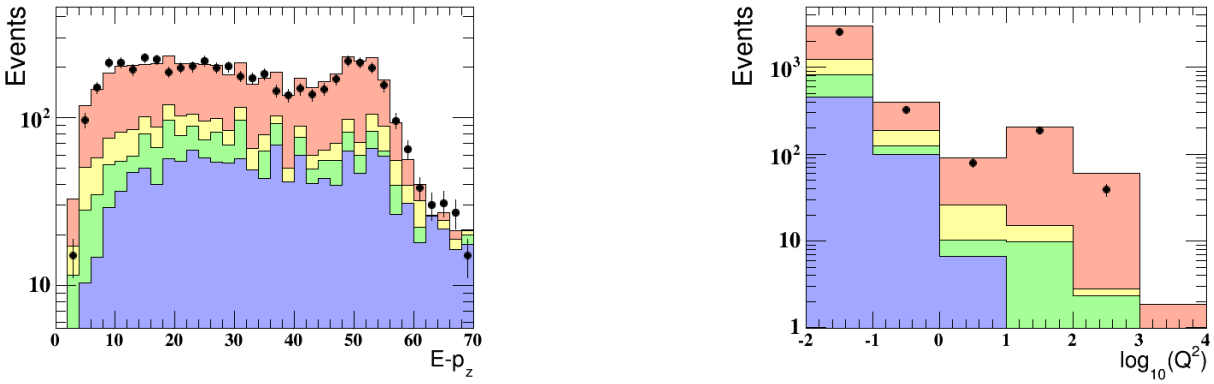

Figure 5.13: The Q^2 distribution in the logarithmic scale (left) and $E - p_z$ (right) from unlike-sign, non-isolated dimuons for both low and high mass regions. Each event contains two muons and has a jet requirement.

Muon control distributions.

Figure 5.14 shows the pseudorapidity and muon transverse momentum p_T^μ from unlike-sign, non-isolated dimuons for both the low and high mass regions.

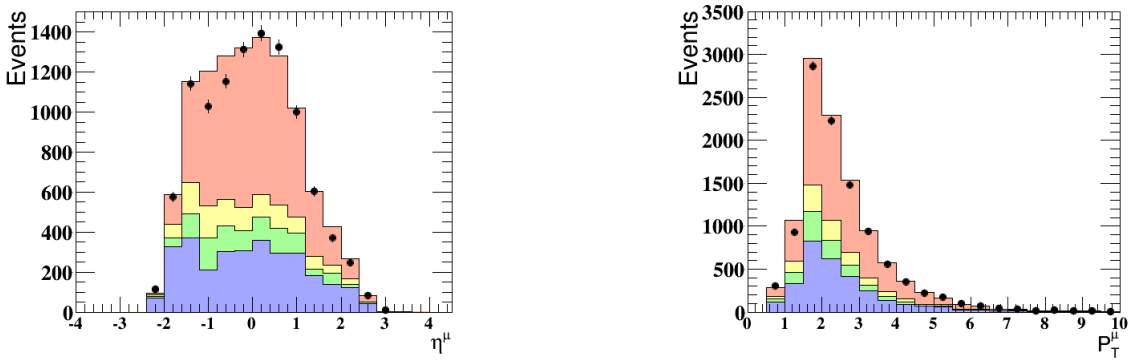

Figure 5.14: The pseudorapidity (left) and the muon transverse momentum p_T^μ (right) distributions from unlike-sign, non-isolated dimuons for both low and high mass regions with a jet requirement.

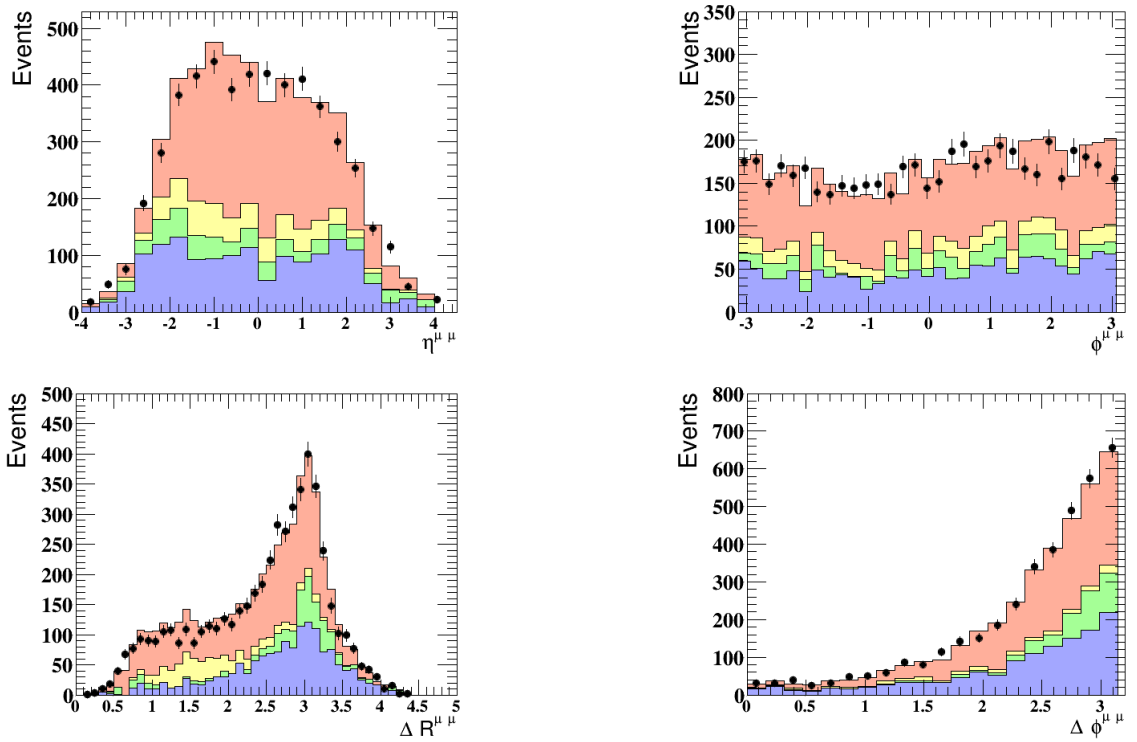

Figure 5.15: Dimuon pseudorapidity $\eta^{\mu\mu}$ (a) and $\phi^{\mu\mu}$ (b) distributions with a jet requirement to be present in event. Angular correlation in ΔR (c) and $\Delta\phi$ (d). All distributions contain the low and high mass regions with unlike-sign dimuon events in non-isolated subsample.

Secondary vertex control distributions

All secondary vertex quantities show good agreement of the second vertices information between the data and MC (Fig. 5.16). The decay length and decay length significance calculation procedure is described in section 3.7. Fig. 5.17 presents its distributions for the all mass region, like- and unlike-sign subsamples.

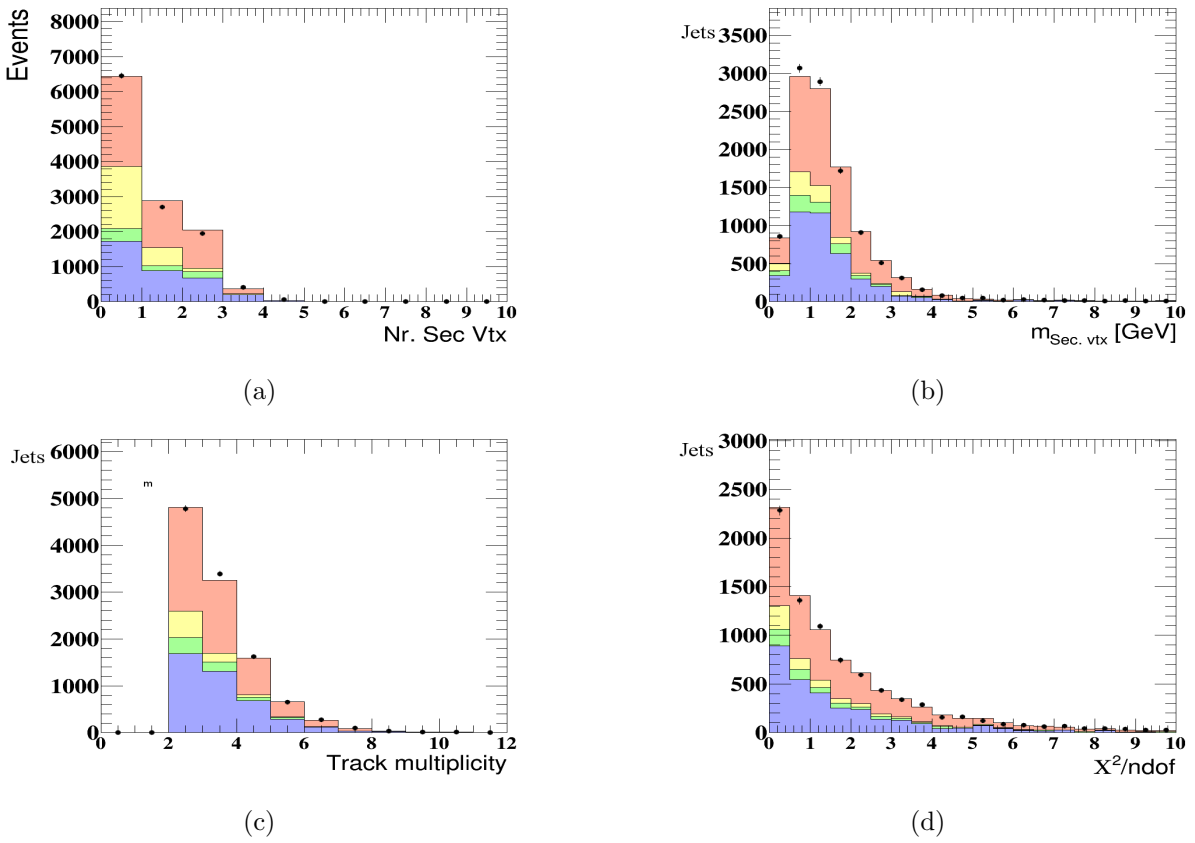

Figure 5.16: Number of secondary vertex candidates (a), mass of secondary vertex candidates (b), track multiplicity of such vertices (c) and normalised χ^2 (d) distributions. Distributions are presented for secondary vertex candidates for like- and unlike-sign dimuon events in the low and high mass regions.

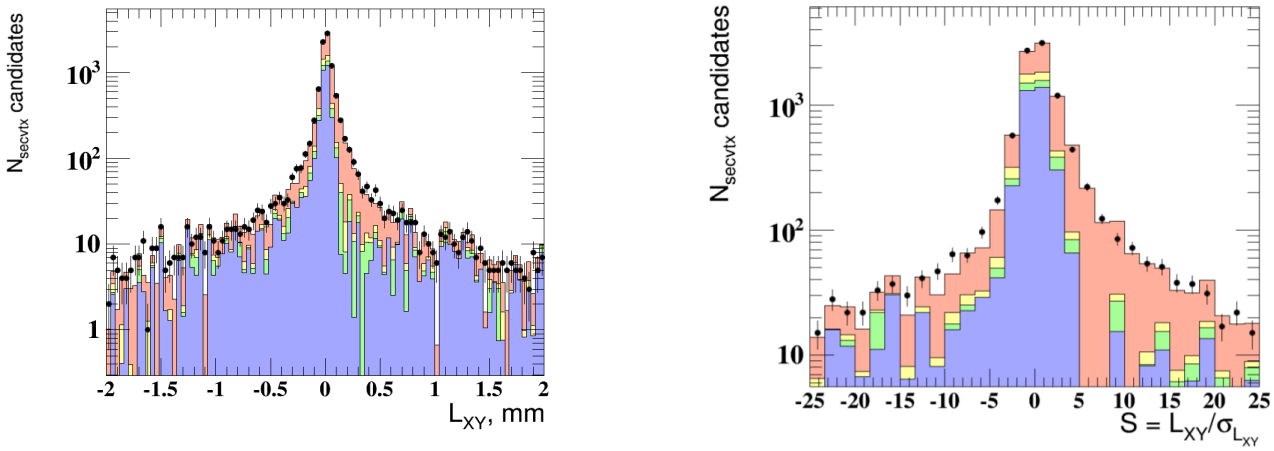

Figure 5.17: The decay length (a) and decay length significance distribution for secondary vertex candidates, like- and unlike-sign dimuon events in low and high mass regions with a jet requirement.

Good agreement is observed, which justifies the initial assumptions. With the new scale factors obtained from the fit procedure (5.5), the decay length significance distribution shows better description of the data by the MC. This is visible especially on the left part of the distribution, where the MC fraction was underestimated.

5.8 Cross section determination

The main process analysed for this analysis is $e^{\pm}p \to b\bar{b} \to \mu\mu X'$. To measure a cross section, the fraction of dimuon events in the data coming from this process have to be determined. The formula is :

$$N_{b\bar{b}\to\mu\mu} = [N^u_{data} - C \cdot N^l_{data} - (S_{c\bar{c}} \cdot N_{c\bar{c}} + N_{VM} + N_{BH})] \times \left(\frac{N^u_{b\bar{b}} + N^l_{b\bar{b}}}{N^u_{b\bar{b}} - N^l_{b\bar{b}}}\right)^{MC} \tag{5.10}$$

where, $N_{c\bar{c}}$ is the unlike- and like-sign difference of the number of $c\bar{c}$ events, (therefore removing non-$c\bar{c}$ background). N_{VM} is the number of unlike-sign, non-isolated dimuon events from the heavy quarkonia ($J/\psi, \psi', Y$), N_{BH} is the number of the unlike-sign, non-isolated dimuon events from the Bethe Heitler MC samples, N_{data} is the number of the data events (like- and unlike-sign) and C is a correction factor which includes residual of the unlike- and like-sign background (Sec. 5.3). $S_{c\bar{c}}$ is the charm scale factor (Eq. 5.9).

This analysis contains two selection criteria for the dimuon selection which is used for the total cross section calculation. In the first case the dimuon sample was selected with using all dimuon selection cuts described in the Sec. (4.5) without the requirement of at least one jet in the dimuon event. Then the total and differential cross section can be calculated.
In the second case the decay length significance distribution was used to extract the charm and beauty contributions. Thus, in addition to the cuts used in the first case, each event requires at least one jet to make a decay length calculation possible. The resulting secondary vertex candidates should pass all requirements which are described in the Sec. (4.5 (Vertex cuts)).

The cross section for a process σ is determined with the number of events N, and integrated luminosity, L as:

$$\sigma = \frac{N}{L} \tag{5.11}$$

The number of beauty events, $N = N_{b\bar{b}\to\mu\mu}$ is obtained from the formula (5.10). The detector acceptance is calculated from the MC and defined as :

$$A = \frac{N^{(MC\ reco)}}{N^{(MC\ true)}} \tag{5.12}$$

where $N^{(MC\ reco)}$ is the number of MC events reconstructed in the same way as data and $N^{(MC\ true)}$ the number of events on the generator level (true). In turn the acceptance uncertainty depends on the reconstructed and true Monte Carlo samples.
For an equation of the form $f(a,b) = a/b$, the general formula of the error propagation (σ_f) is :

$$\frac{\sigma_f}{f} = \sqrt{\left(\frac{\sigma_a}{a}\right)^2 + \left(\frac{\sigma_b}{b}\right)^2} \tag{5.13}$$

To consider the detector acceptance, equation (5.11) becomes :

$$\sigma_{b\bar{b}\to\mu\mu} = \frac{N_{b\bar{b}\to\mu\mu}}{L \cdot A} \tag{5.14}$$

For a given variable X, the single differential cross section is defined as follows:

$$\frac{d\sigma}{dX} = \frac{N^{X_i}}{L \cdot A \cdot \Delta X_i} \tag{5.15}$$

where ΔX is the width of the i-th bin X.
The differential cross section bin values are calculated separately and normalised by bin width. The acceptance and number of beauty events are calculated separately for each bin while the luminosity value stays the same for all the bins. The statistical uncertainties for the total and differential cross sections depend on the number of beauty events. They are calculated using formula 5.13. Figure 5.14 and bottom part of Fig 5.15 shows the muon and dimuon distributions. In bins of such parameters, the differential cross sections were calculated.

The fitted scale factor impact.
The fit procedure of the decay length significance distribution performs an update of the beauty and charm Monte Carlo scale factors. It changes the fraction of the beauty dimuon events. As one can see from the formula (5.10), the beauty scale factor does not have an impact on the final dimuon events fraction (since it is reduced in the fractional part of the formula) while the charm scale factor corrects the $c\bar{c}$ fraction. But one can not say that the beauty scale factor does not make a contribution to the overall cross section measurements. The beauty scale factor was obtained from the fit in combination with the charm coefficient. By increasing the contribution of the beauty events the charm event contribution is reduced. Therefore, the beauty factor has an indirect contribution to the cross section calculation.

Chapter 6

Cross Section Measurement

In Section 5.8, a detailed explanation how the total and differential cross section was measured is given. This chapter describes the total and differential cross section measurement results. The first section shows the total cross section results in this analysis. Section 6.2 shows the differential cross section results for both the case with and without the decay length significance fit procedure. The decay length significance fit procedure is applied to improve the charm and beauty Monte Carlo samples contribution. The last section contains information about the systematic uncertainty studies.

6.1 Visible and total cross section

For the process $e^{\pm}p \to e' b\bar{b} X \to e'\mu\mu X'$ the total and visible cross section is measured. The total cross section is calculated in two ways. The first case is the total cross section calculated from the dimuon sample without including the decay length significance fit results. The second case includes the fit results as well as an additional requirements on the event selection (Sec. 4.5).

In the first case which is similar to the previous analyses, the beauty contribution factor was calculated with Eq. (5.6) and $S^{MC}_{b,lm+hm} = 1.85 \pm 0.06$. The charm factor was obtained from the previous analysis [99], $S_{c\bar{c}} = 1.37 \pm 0.20$. Using Eq. (5.10) the fraction of the dimuon events coming from the studied process was calculated, and is shown in Tab. (6.1, second row) as well as the corresponding acceptance and luminosity values.

In the second case, the additional requirement that the event should contain at least one jet candidate is present. Using the jet information the decay length significance was calculated and the fit procedure performed (Section 5.5). From the decay length significance fit procedure the charm and beauty scale factors obtained were: $S_{c\bar{c}} = 1.12 \pm 0.14$, $S^{MC}_{b,lm+hm} = 2.07 \pm 0.08$. From the equation (5.8) one can see that the cross section calculation does not depend from the beauty MC fraction changes but it depends from the charm scale factor. In this case this value is smaller then the corresponding value which was taken in the previous HERA II analysis ([99]), and therefore the effect of increasing the contribution of the beauty dimuon events is present. This, in turn slightly increases the total cross section. Table (6.1) shows comparison

of the values which were extracted from the data and MC samples and were used for the total cross section measurements.

	$\sigma_{b\bar{b}\to\mu\mu}(pb)$	$N_{b\bar{b}\to\mu\mu}$	N^{MC}_{rec}	N^{MC}_{gen}	A	L (pb^{-1})
with > 1jet req.	50.16 ± 3.28	4455	3368	14279	0.24 ± 0.01	376.61
no jet req.	43.27 ± 3.01	4673	4140	14279	0.29 ± 0.01	

Table 6.1: The total cross section calculation values, where the "with jet req." means that the cross section was calculated from the sample which have passed all dimuon event selection cuts (Sec. 4.5) with the additional requirement of at least one jet in the event, while the "no jet req." case has dimuon event selection cuts only.

There are two contributions in the visible cross section. A part of it comes from direct b-hadron decays and the other part is from the indirect decays with muons as an output. In the same time, two muons as output can originate either from different quarks of the $b\bar{b}$ - pair or from the same beauty quark.
In order to compare results with previous results [99, 117], the same phase space region for the visible cross section was defined:

- for both muons: $\eta \, \epsilon \, (-2.2, 2.5)$,
- for one of the muon: $p_T > 1.5$ GeV and for the other : $p_T > 0.75$ GeV,
- additional for the other muon for $\eta^\mu > 0.6 : p^\mu > 2.5$ GeV or $p_T^\mu > 1.5$ GeV and for $\eta^\mu < 0.6 : p^\mu > 1.8$ GeV.

Within defined phase space, the visible cross section for the process defined above in this analysis was measured for the two cases:

$$\begin{aligned} &\text{standard dimuon selection, no jet requirements:} \\ &\sigma_{vis}^{HERA\ II}(e^\pm p \to b\bar{b}X \to \mu\mu X') = 43.27 \pm 3.01\ (stat.)\ ^{+13.15}_{-11.06}\ (syst.)\ pb, \\ &\text{including } DL_{sign} \text{ fit procedure:} \\ &\sigma_{vis}^{HERA\ II}(e^\pm p \to b\bar{b}X \to \mu\mu X') = 50.16 \pm 3.28\ (stat.)\ ^{+15.28}_{-12.84}\ (syst.)\ pb, \end{aligned} \tag{6.1}$$

The measured HERA II cross section listed above is compatible with the NLO predictions from the FMNR $\bigotimes$ PYTHIA [41].

$$\sigma_{vis}^{NLO}(e^\pm p \to b\bar{b}X \to \mu\mu X') = 33^{+18}_{-8}\ pb. \tag{6.2}$$

The effective fraction of $b\bar{b}$ pairs decaying into at least two muons is 6.3% [126]. The probabiltity for such muon pair to be in the visible kinematic range, evaluated from the beauty MC, is on average $\approx$ 6% [99]. Thus for a beauty quark pair the probability to have a muon pair in the

visible range is a product of these two probabilities:

$$P_{vis}^{b\bar{b}\to\mu\mu} \approx 0.38\%. \tag{6.3}$$

The total cross section is then calculated as the visible cross section divided by the combined probability (Eq. 6.3). For this analysis the total cross section for the beauty quark production ($e^{\pm}p \to b\bar{b}X$) is measured:

$$\begin{aligned} &\text{standard dimuon selection, no jet requirements:} \\ &\sigma_{total}^{HERA\ II} = 11.38 \pm 0.79\ (stat.)\ ^{+3.46}_{-2.91}\ (syst.)\ nb, \\ &\text{including } DL_{sign} \text{ fit procedure:} \\ &\sigma_{total}^{HERA\ II} = 13.20 \pm 0.86\ (stat.)\ ^{+4.02}_{-3.38}\ (syst.)\ nb, \end{aligned} \tag{6.4}$$

Where for the previous analysis based on HERA I, HERA II and NLO predictions:

$$\begin{aligned} &\sigma_{total}^{HERA\ II} = 12.6 \pm 1.0\ (stat.)\ ^{+3.6}_{-3.3}\ (syst.)\ nb\ [99], \\ &\sigma_{total}^{HERA\ I} = 13.9 \pm 1.5\ (stat.)\ ^{+4.0}_{-4.3}\ (syst.)\ nb\ [117], \\ &\sigma_{total}^{NLO} = 7.5\ \pm^{+4.5}_{-2.1}\ (syst.)\ nb\ [41]. \end{aligned} \tag{6.5}$$

The total cross section measurement with fit improvements for this analysis is in good agreement with the NLO prediction and with previous analyses based on the HERA I and HERA II data. Due to the set of bug fixes and missing of the possibility to check with author step by step all technical aspects, the results from the previous HERA II analysis (6.5) are a bit different from the current analysis results (6.4, first line) obtained with HERA II data. Nevertheless, differences are within the statistical uncertainties. The most interesting part of the total cross section calculations is that the calculated total cross section with including a decay length significance procedure (6.4, second line) with reduced data set (because of a jet requirement) is in good agreement within the statistical and systematic uncertainties.

6.2 Differential cross Section Results

In this analysis differential cross sections were calculated in bins of muon transverse momentum, p_T^μ, muon angle η^μ, and $\Delta R^{\mu\mu}, \Delta\phi^{\mu\mu}$. Each of the differential cross section distributions includes both the direct and indirect b-hadrons decays.
In order to compare differential cross sections with previous analysis, the cuts on transverse momentum and pseudorapidity for both muons are:

$$\eta^{\mu_{1,2}} \epsilon (-2.2, 2.5), \quad p_T^{\mu_{1,2}} > 1.5\ GeV \tag{6.6}$$

The scale factors for the different MC were recalculated due the different phase space definitions:

$$\begin{aligned} &\text{standard dimuon selection, no jet requirements:} \\ &S_{b\bar{b}} = 1.92 \pm 0.08, S_{c\bar{c}} = 1.37 \pm 0.20. \\ &\text{including DL sign fit procedure:} \\ &S_{b\bar{b}} = 2.31 \pm 0.09, S_{c\bar{c}} = 1.06 \pm 0.14. \end{aligned} \tag{6.7}$$

Tab. (6.2) shows the number of events for these two cases. The differential cross sections are

	$N_{b\bar{b}\to\mu\mu}$	N^{MC}_{rec}	N^{MC}_{gen}	A	$L\ (pb^{-1})$
with > 1jet req.	3757	2891	14279	0.20 ± 0.01	376.61
no jet req.	3892	3110	14279	0.22 ± 0.01	

Table 6.2: The number of events, where the "with jet req." means that the event contains at least one jet in the event, while the "no jet req." case has dimuon event selection cuts only. In both case the cuts on pseudorapidity and p_T listed in this section are used.

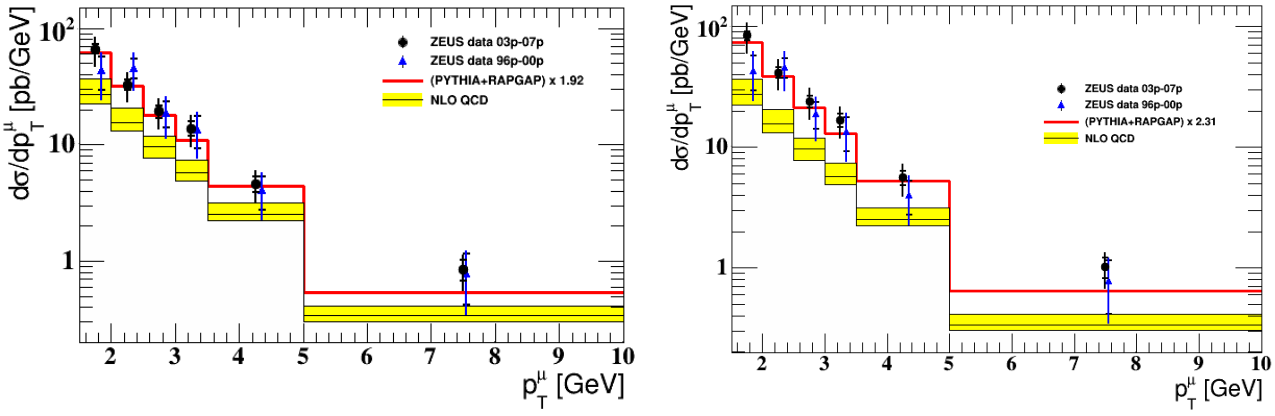

Figure 6.1: Differential cross section in p_T^μ bins. The HERA II results (black points) are compared to HERA I (blue triangles) and to the NLO QCD prediction from FMNR ⊗ PYTHIA (yellow band) and with LO PYTHIA and RAPGAP (red line). The left part corresponds to measured differential cross section in a "standard" way, with the $S_{c\bar{c}} = 1.37$. The right part is measured with charm scale factor is obtained after the DL_{sign} fit procedure.

calculated with the two selection criteria applied to the data samples similar to the total cross section calculations. While the "standard case" contains all events and selection requirements which is present for the previous analysis, the additional technique of the decay length significance fit was used indirectly in the second way, and uses data samples with the requirement of at least one jet per event. The following differential cross section figures will show a comparison of these two cases. Figure 6.1, left plot, shows the differential cross section in p_T^μ bins

P_T^μ bins	A (a)	A (b)	$d\sigma/dp_T^\mu \pm stat.^{err}$ (a)	$d\sigma/dp_T^\mu \pm stat.^{err}$ (b)
1.5-2.0	0.19	0.16	66.4 ± 6.3	84.1 ± 7.1
2.0-2.5	0.28	0.24	32.7 ± 3.6	41.4 ± 4.1
2.5-3.0	0.32	0.27	19.3 ± 2.3	24.1 ± 2.6
3.0-3.5	0.33	0.28	13.8 ± 1.9	16.7 ± 2.1
3.5-5.0	0.32	0.28	4.6 ± 0.7	5.6 ± 0.8
5.0-2.0	0.27	0.23	0.8 ± 0.2	1.0 ± 0.2

Table 6.3: p_T^μ differential cross section numbers. Where the case (a) is related to the scale factor obtained from the general procedure and formula (5.5). The case (b) is related to the charm scale factor obtained after the DL_{sign} fit procedure. This marks correspond to Fig. 6.1.

for the "standard" analysis and event selection. The shape and values of this distribution is in a good agreement with the previous analysis based on HERA II [99]. Fig. 6.1, right plot, shows that including secondary vertex information increases the cross section values in each bin. This behavior is caused by the fact that the charm contribution is lower (Eq. 6.7) after the secondary vertex information was included. These conclusions fit well to the other differential cross section distributions which are shown below.

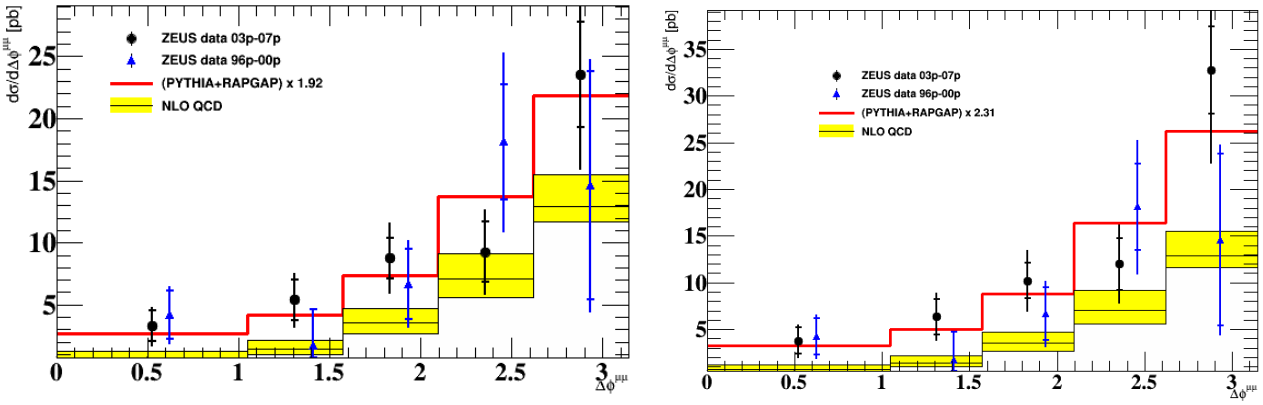

Figure 6.2: Differential cross section in $\Delta\phi^{\mu\mu}$ bins. The dimuon events satisfy cuts on p_T and on η listed at the beginning of this section. The HERA II analysis (black points) are compared to the HERA I (blue triangles) and to the NLO QCD prediction from FMNR $\otimes$ PYTHIA (yellow band) and with LO PYTHIA and RAPGAP (red line). The left part corresponds to the measured differential cross section with the $S_{c\bar{c}} = 1.37$. The right part is measured with the $S_{c\bar{c}} = 1.12$, scale factor obtained after the DL fit procedure.

$\Delta\phi^{\mu\mu}$ bins	A (a)	A (b)	$d\sigma/d\Delta\phi^{\mu\mu} \pm stat.^{err}$ (a)	$d\sigma/d\Delta\phi^{\mu\mu} \pm stat.^{err}$ (b)
0.0 - 1.047	0.11	0.09	3.3 ± 1.2	3.8 ±1.4
1.047 - 1.571	0.17	0.14	5.4 ± 1.6	6.4 ±1.9
1.571 - 2.094	0.23	0.19	8.7 ± 1.6	10.2 ±1.9
2.094 - 2.618	0.28	0.24	9.3 ± 2.4	11.9 ±2.7
2.618 - 3.141	0.29	0.25	23.5 ± 4.2	32.7 ±4.7

Table 6.4: $\Delta\phi^{\mu\mu}$ cross section numbers. a is related to the scale factor obtained from the general procedure and formula 5.5. b is related to the results where the charm scale factor obtained after the DL fit procedure. Differential cross section is measured in (pb/rad) units.

To have a detailed look on the beauty quark properties the differential cross sections in bins of p_T^μ and η^μ were calculated. Figure (6.1) shows the differential cross section in p_T^μ bins. Both plots show the comparison beetween the HERA II analysis (black points), the HERA I (blue triangles), the NLO QCD prediction from FMNR ⊗ PYTHIA (yellow band) and LO PYTHIA and RAPGAP (red line) scaled to the HERA II data. The left plot shows the differential cross section calculated without the decay length fit procedure, while the right plot shows the differential cross section with the fit results included. Table (6.3) shows the numerical values obtained for the differential cross section measurements.
In order to study the correlation of the b quarks in the $b\bar{b}$ system, differential cross sections in bins of $\Delta\phi^{\mu\mu}$ and $\Delta R^{\mu\mu}$ were measured (Fig. (6.2, 6.4)).

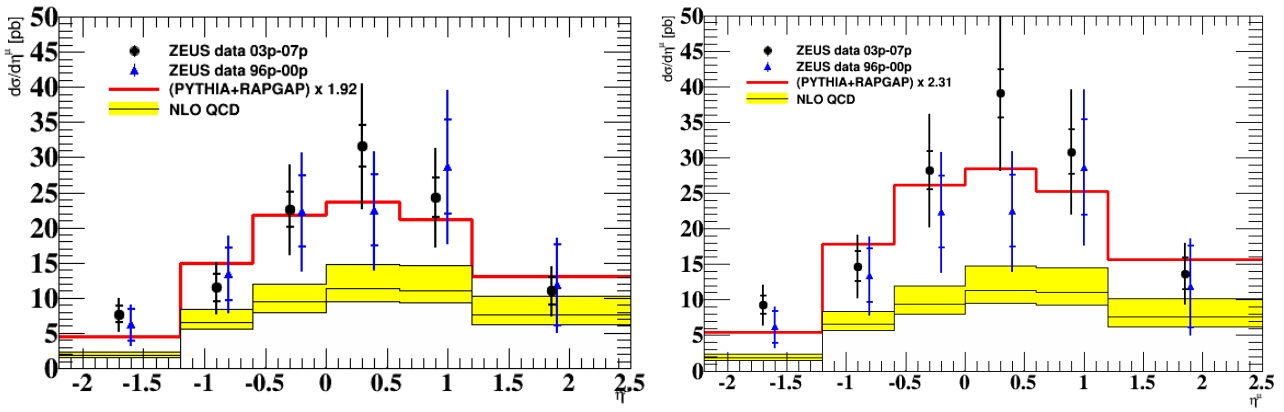

(a) (b)

Figure 6.3: Differential cross section in η^μ bins. Di-muon events satisfy cuts on p_T and on η listed at the beginning of this section. The HERA II analysis (black points) are compared to the HERA I (blue triangles) and to the NLO QCD prediction from FMNR ⊗ PYTHIA (yellow band) and with LO PYTHIA and RAPGAP (red line). The left part corresponds to measured differential cross section with the $S_{c\bar{c}} = 1.37$. The right part is measured with the charm scale factor obtained after the DL fit procedure.

The decay length significance fit shows that the beauty fraction was underestimated, while the charm contribution was slightly overestimated. This situation is reflected in all differential cross section plots with secondary information included.

η^μ bins	A (a)	A (b)	$d\sigma/d\eta^\mu \pm stat.^{err}$ (a)	$d\sigma/d\eta^\mu \pm stat.^{err}$ (b)
-2.2 : -1.2	0.34	0.29	7.7 ± 1.1	9.3 ± 1.3
-1.2 : -0.6	0.33	0.28	11.4 ± 1.9	14.7 ± 2.2
-0.6 : 0.0	0.31	0.26	22.6 ± 2.4	28.2 ± 2.8
0.0 : 0.6	0.29	0.25	31.6 ± 2.9	39.1 ± 3.4
0.6 : 1.2	0.24	0.21	24.3 ± 2.8	30.8 ± 3.2
1.2 : 2.5	0.13	0.11	11.0 ± 1.9	13.7 ± 2.2

Table 6.5: η^μ cross section numbers. a is related to the scale factor obtained from the general procedure and formula 5.5. b is related to the results with the charm scale factor obtained after the DL fit procedure.

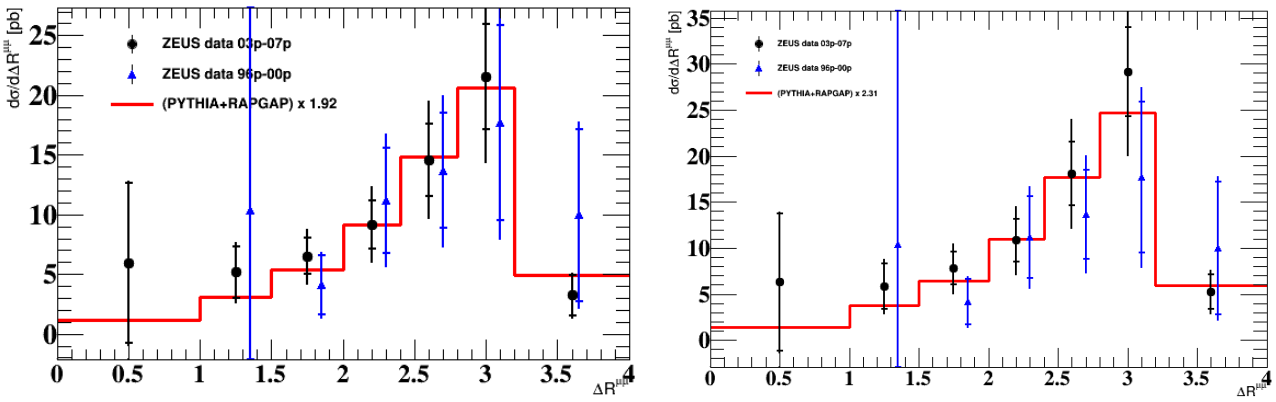

(a) (b)

Figure 6.4: Differential cross section in $\Delta R^{\mu\mu}$ bins. Di-muon events satisfy cuts on p_T and η listed at the beginning of this section. The HERA II analysis (black points) are compared to the HERA I (blue triangles) and to the NLO QCD prediction from FMNR $\otimes$ PYTHIA (yellow band) and with LO PYTHIA and RAPGAP (red line). The left part corresponds to measured differential cross section with the $S_{c\bar{c}} = 1.37$. The right part is measured with the charm scale factor obtained after the DL fit procedure.

$\Delta R^{\mu\mu}$ bins	A (a)	A (b)	$d\sigma/d\Delta R^{\mu\mu} \pm stat.^{err}$ (a)	$d\sigma/d\Delta R^{\mu\mu} \pm stat.^{err}$ (b)
0 - 1	0.01	0.01	5.9 ± 6.7	6.3 ±7.4
1 - 1.5	0.07	0.06	5.2 ± 2.1	5.7 ±2.5
1.5 - 2.0	0.19	0.16	6.5 ± 1.5	7.8 ±1.7
2.0 : 2.4	0.27	0.23	9.2 ± 2.0	10.8 ±2.3
2.4 : 2.8	0.29	0.25	14.6 ± 3.0	18.1 ±3.4
2.8 : 3.2	0.30	0.26	21.5 ± 4.4	29.1 ±4.8
3.2 : 4.0	0.27	0.23	3.2 ± 1.7	5.2 ±1.9

Table 6.6: $\Delta R^{\mu\mu}$ cross section numbers. a is related to the scale factor obtained from the general procedure and formula 5.5. b is related to the results with the charm scale factor obtained after the DL fit procedure. Differential cross section is measured in (pb/ΔR) units.

6.3 Systematic Uncertainties

There is a list of sources of systematic errors which were studied in this analysis:

- **The Bethe-Heitler and heavy quarkonia contributions.** The normalisation of such processes was changed by ±50%. The impact on the visible cross section of such a variation is $^{+10\%}_{-3\%}$.
- **Dimuon isolation criterion,** $I^{\mu\mu}$. This parameter was varied by ± 500 MeV. The impact on the visible cross section is $^{+2.7\%}_{-3.0\%}$.
- **Variation of the calorimeter transverse energy cut**. The cut on the hadronic E_T was changed to 7 and 9 GeV. This makes an impact to the visible cross section at $^{+3.5\%}_{-2.2\%}$.
- **Muon efficiency correction** impact was obtained from the previous HERA II analysis . $^{+20.2\%}_{-18.4\%}$.
- **Charm and beauty spectral shape.** This uncertainties are related to the variation of the direct and not direct $b\bar{b}$ and $c\bar{c}$ MC contributions. The values were roughly taken from the previous analysis as ±12% for the beauty shape changes and as ±2% for the charm shape changes
- **Luminosity impact.** The luminosity uncertainty of ±2% has the same directly propagates to the visible cross sections [99].

The total impact to the systematic visible cross section changes is calculated separately for the positive and negative changes of the parameters listed above. The contributions from each item listed above were added in quadrature. The systematic uncertainties study is not completed.

6.4 Summary

This section shows the total and differential cross section results which were calculated with the "standard" technique based on the previous analysis and with the additional technique based on secondary vertex information namely decay length significance fit procedure. The differential cross sections are compared for both cases and show similar shape of the distributions, while bin values are higher in case where secondary vertex information is used. The reason for this is the lower charm contribution obtained after the decay length significance fit. The total cross section calculations with the "standard" procedure show a good agreement with the previous results from the HERA I,II analysis. The calculations with the additional technique shows nice agreement within their uncertainties to both previous results and NLO calculations.

Chapter 7

CMS tracker alignment

This chapter describes the technical task performed in the context of this thesis and its results. It starts with Section 7.1 which gives a general overview of the experiment and the detector structure. In Section 7.2 the alignment procedure as well as a detailed description of the issues to be addressed are introduced. The last Section 7.3.4 shows a step by step solution of the problem and summarises the results of the task.

7.1 Introduction

The Compact Muon Solenoid (CMS) [129] detector is a general-purpose particle physics detector at the Large Hadron Collider (LHC). The main task of the CMS experiment is the exploration of a multitude of physical processes. Among many others these are the study of the properties of the Higgs boson, and searches of new particles such as those which might make up dark matter. A good quality for these important searches is not possible without high tracking resolution of the CMS detector. The results of the study of the tracker alignment in this section helped to understand the weak modes of the alignment procedure which in turn helps to better control the detector resolution. The high tracking efficiency requirement includes high angle, momentum and position resolutions. This becomes possible due to a strong magnetic field and a high resolution ($10 - 30\ \mu m$) of the silicon detector modules (pixel and strip accordingly)[25].

Tracker detector

The CMS detector [129] consists of subdetectors such as: tracker detector, electromagnetic calorimeter, hadron calorimeter and muon detectors. In this study the tracker detector is used. The CMS tracker is the world's largest silicon detector, consisting of more than 25 000 sensors. It is designed to track or measure different type of particles emerging from proton-proton and heavy ion collisions. Finding the energy loss and momentum of a particle gives clues to its identity. The detector uses a huge solenoid magnet to curve particles trajectory. This takes the form of a cylindrical coil of superconducting cable, cooled to $-268.5°C$, that generates a magnetic field of 3.8T, about 100,000 times that of the Earth [26] .

The tracker can reconstruct the paths of high-energy muons, electrons and hadrons as well as can registrate the tracks coming from the decay of very short-lived particles such as beauty quarks. It can record particle paths accurately. Each measurement is accurate to 10-30 μm. The tracker is also the innermost layer of the detector and so receives the highest density of particles. The construction materials were therefore carefully chosen to resist radiation [28].

7.2 Methodology of the track-based alignment

The track-based alignment procedure uses the minimization [27] of the residuals between the measured and expected hit positions in the detector. The silicon module positional parameters are used for track reconstruction. Typically the assumed position is different from the true one, and this is one of the reasons for which we observe track reconstruction residuals. The alignment algorithm uses hit information from many tracks and the least square approach is used to minimise the sum of squares of normalised residuals. The main goal of the alignment is to obtain a set of the geometry parameters which are as close to the true one as possible. The CMS tracker geometry parameters (geometry model) are obtained when the alignment procedure is applied.

A geometry model is a set of geometry parameters such as spatial coordinates, angles, sensor distortion parameters for a single detector module or for a group of modules. Tracks are reconstructed from the hits in the detector. The minimised function is :

$$\chi^2(\mathbf{p},\, \mathbf{q}) = \sum_{j}^{tracks} \sum_{i}^{measurements} \left(\frac{m_{ij} - f_{ij}\left(\mathbf{p}, \mathbf{q}_j\right)}{\sigma_{ij}} \right) \tag{7.1}$$

where i is a hit iterator, j is a track iterator, m_{ij} is the measurements of the track hit positions on the modules, σ_{ij} is hit measurements uncertainties. f_{ij} is the trajectory prediction based on the track ($\mathbf{q}_j$) and $\mathbf{p}$ are geometry (alignment) parameters.

The initial geometry description which is taken as a set of exemplary parameters is usually obtained from a previous alignment. The f_{ij} can be linearised around the values from the initial geometry. In cases where corrections are not small the solution is to obtain the next iterations of the same procedure [27]. After linearisation, the minimisation of the χ^2 function leads to the standard equations of the least square principle:

$$\mathbf{Ca} = \mathbf{b}, \tag{7.2}$$

where $\mathbf{a}$ is the vector of alignment geometry(global) and track (local) parameters, $\mathbf{b}$ is a product of residuals and global derivatives (measured) and $\mathbf{C}$ is the symmetric $n \times n$ matrix of the measured parameters.

The CMS detector alignment procedure is performed using the MILLEPEDE II (MPII) program [31]. The simultaneous solution of all the linear equations is a complex technical problem. The system has more than $2 \cdot 10^5$ equations and of the order of millions of parameters.

However, the individual tracks are independent of each other. This leads to a block structure of the equation matrix. The MILLEPEDE II program uses this special structure of the matrix **C** as well as a global-fit approach and block matrix algebra. This helps to reduce the large system of equations (7.2) to a smaller one [30]. At the end of the procedure the large system of equations is decreased into a few orders smaller one with alignment parameters only and brings us to the equation:

$$\mathbf{C'p = b'} \tag{7.3}$$

where **C'** and **b'** are values that summarise contribution from all tracks , and **p** is the vector of the alignment parameters. This is how a solution to so many equations becomes possible.

7.3 Weak modes

The alignment procedure of the CMS tracker is a powerful tool to extract information about the position, roration and deformation of all detector modules. However in the case of systematic shifts of a large amount of modules such a global detector rotation, deformation or overall detector shift, the alignment procedure of the CMS tracker may not take them into account. In such case the matrix **C** in equation (2.3) could be numerically close to being singular. As a result there can be linear combinations of parameters that do not have a strong impact on the overall χ^2 (**p**, **q**). These linear combinations are called "weak modes". Their contribution is not known in most cases.

Changes of the track parameters can be compensated by changes of the alignment parameters. If this has no strong impact to the χ^2 it may become a major problem for the alignment because it is hard to eliminate. Weak modes depend on the segmentation of the detector and on the track types used for the alignment. Given the fact that the CMS detector has cylindrical geometry and that collisions usually have tracks which go though the beam line one can use cylindrical coordinates for weak mode classification. To study the weak modes, the change of r, ϕ and z as functions of r, ϕ, z are monitored. Traditionally if $\Delta\phi(z)$ has been changed significantly the weak mode is called "Twist" weak mode. In the case of $\Delta y(r)$ changes the name of the weak mode is "Sagitta". $\Delta z(z)$ changes are called "Telescope" weak mode. A more detailed description of the weak modes will be given in the next sections.

It is required to include additional information in the equation (7.2) for better control of the weak modes. There are many possible ways to add this information. Cosmic ray tracks can break the cylindrical symmetry. Tracks recorded without magnetic field can give extra information, as well as knowledge about the vertex of the track and the invariant mass of a resonance from which tracks are observed. For example, they can originate from W, Z-bosons. The combination of the collision and cosmic data sets with magnetic field on and off, as well as resonance data, helps to deal with the weak modes.

For some reasons such as small statistics, the χ^2 minimisation can give an error matrix with large values. The reason for this could be a strong changes of the detector geometry. The

solution for this problem in general is to prepare a second iteration of the alignment. The first iteration estimates an approximate true parametrisation with large errors. The second iteration on top of the first will improve the results and the error matrix. Significant changes in the true geometry are usually observed after detector upgrades. For the weak modes a second iteration does not help because as described above the reason for this problem is the compensation of the alignment and track parameters and this is not resolvable with many iterations. The weak mode problem can only be resolved with information from additional data.

7.3.1 The twist weak mode

A twist is a deformation of the tracker, in which the modules are moved coherently in $\Delta\phi$ by an amount directly proportional to their longitudinal position: $\Delta\phi = \mathrm{C} \cdot \mathrm{z}$.

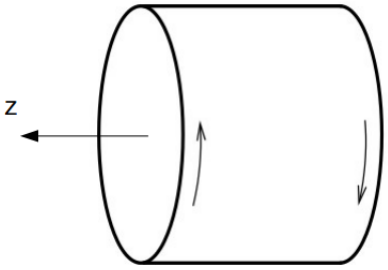

Figure 7.1: Schematic sketch of the twist process weak mode.

Here C is the proportionality constant. In this case, the further module is placed radially from the center, the large it will be displaced. For this mode, during the χ^2 minimisation, alignment parameter values are compensated by changes of the track parameters that create the weak mode. Schematically it is shown in the Figure 7.1.

7.3.2 The sagitta weak mode

A "Sagitta" weak mode is a process in which the deformation of the tracker has the behaviour: $\Delta y = \mathrm{C} \cdot \mathrm{r}$.

The "Sagitta" weak mode describes the tracker deformations in which the modules are moved coherently in the direction of the y-axis by an amount directly proportional to their radius r. This mode is accompanied by off-centring of the barrel layers and the endcap rings. Schematically it is shown in the Figure 7.2

7.3.3 The telescope weak mode

A "Telescope" weak mode is a process in which the deformation of the tracker has the behaviour $\Delta y = \mathrm{C} \cdot \mathrm{z}$.

The tracker barrel layers can be shifted in the z-direction as shown on figure 7.3. In this case, since the layer shifts are coherent, the changes of the geometry parameters will be compensated

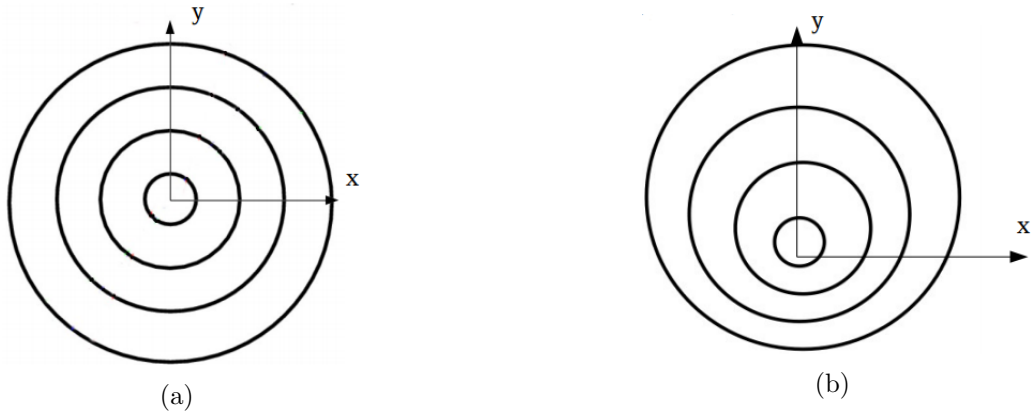

Figure 7.2: Comparison of two configurations. The left one (a) shows the normal barrel layer positions in the $x - y$ plane. The right figure (b) shows the influence of the "Sagitta" weak mode.

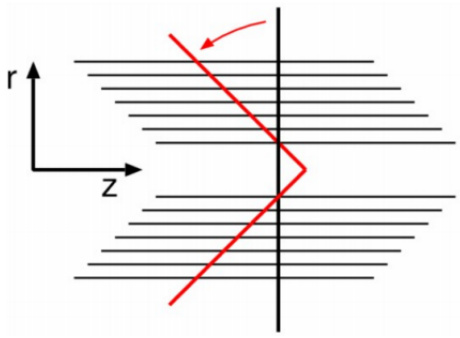

Figure 7.3: Schematic sketch of the telescope weak mode. The black line shows the true track direction through the detector. The red line shows the changed track trajectory as it will be reconstructed in the case when the telescope weak mode is present.

by the changes of the tracks parameters. This figure vividly shows us how the weak mode misalignment is dangerous.

7.3.4 Detailed strategy and results

In this section the main results of the weak modes study are described. For the alignment procedure the MILLEPEDE II package has been used. The following data were used to prepare the alignment:

- Primarily, **cosmic rays at four Tesla magnetic field** (3.8T) are used for the alignment. For this study the number of events used is around 1.1 million. For the cosmic ray data tracks must have momentum $p > 4\ GeV$ and the number of hits in the tracker should be larger than seven.

- 1.2 million events **cosmic rays measured with 0T magnetic field** were used.

- In 2012 there were periods when the magnetic field changed from 0 Tesla to four and back. During that period data has also been recorded. In this study we use 3.5 million of this kind of events as so-called interfill cosmic data which is the combination of the

cosmic rays measured with 0T and 3.8T. Half of the sample has been collected with the tracker operating in peak mode and the other half in deconvolution mode.

- The dataset with **isolated muons** for this study has fifteen million events. Isolated muons are reconstructed in both the muon system and the tracker. They are separated from any jet candidate. Jet candidates should have a transverse momentum of more than 40 GeV. Muons are separated from the jet candidates by a distance $\Delta R = \sqrt{(\Delta\phi)^2 + (\Delta\eta)^2}$ above 0.1. They must have momentum larger than 8 GeV and their transverse momenta should be more than 5 GeV. The number of hits for muons from this dataset should be more than 9 for the tracker and at least one for the pixel part.

- **A minimum bias** dataset with a statistic of 2M events. Tracks from this dataset are required to have more than seven hits and should have momenta more than > 8 GeV.

- **A Z**$\rightarrow \mu\mu$ data set with $N_{events} = 2.5$ M. This data sample contains events from any trigger that requires two muons and is used for Z-boson candidate reconstruction. The two muons have the same hit reqirements as the isolated muons. They also must have transverse momentum larger than 15 GeV. The distance from the reconstructed jets, ΔR should be larger than 0.2. The main benefit of this data sample is a mass constraint which can be used for the two muon system to be in the window (85.8, 95.8) GeV.

The 2012 alignment which was done by the CMS tracker alignment group, was the final alignment on the full amount of the 2012 data which took into account all new features of the MPII alignment technique, which in some cases were not available by the time the geometries for 2012 were provided. This geometry has been taken as a true tracker geometry and all tests have been performed on top of this.

This study was performed with the following steps. Starting from the 2012 geometry a misalignment procedure was applied. In our case misalignment means the simulation of the tracker shifts due to the defined weak mode. For all of them a linear misalignment function has been chosen. The misalignment function for the sagitta was chosen to be Δy $= 5 \cdot 10^{-4} \cdot$ r, for the twist dependency it is $\Delta\phi = 4 \cdot 10^{-4} \cdot$ z, and for the telescope: Δz $= 5 \cdot 10^{-4} \cdot$ r. The result of the procedure is illustrated on Figure 7.4. For a detailed explanation of the abbreviations in the legend see section 2.3.2. The Figures 7.4 and 7.5 show the difference between the two geometries. The results of the alignment procedure are compared to the initial 2012 geometry parameters. In the case when a weak mode is fully taken into account by the alignment procedure, the alignment parameters will be the same as for the true geometry. In such case one will see an ideal plot showing just a y-axis zero line. For the case when the original misalignment is applied, the plots in figure 7.4 show a difference between the true and misaligned geometries. The "realignment" procedure is used to the subdetectors. Each single module parameters are aligned and determined relative to each other but all are defined with respect to the tracker part parameters. After the application of "realignment" procedure figure 7.5 shows the difference between the initial geometry and the one after the second alignment iteration.

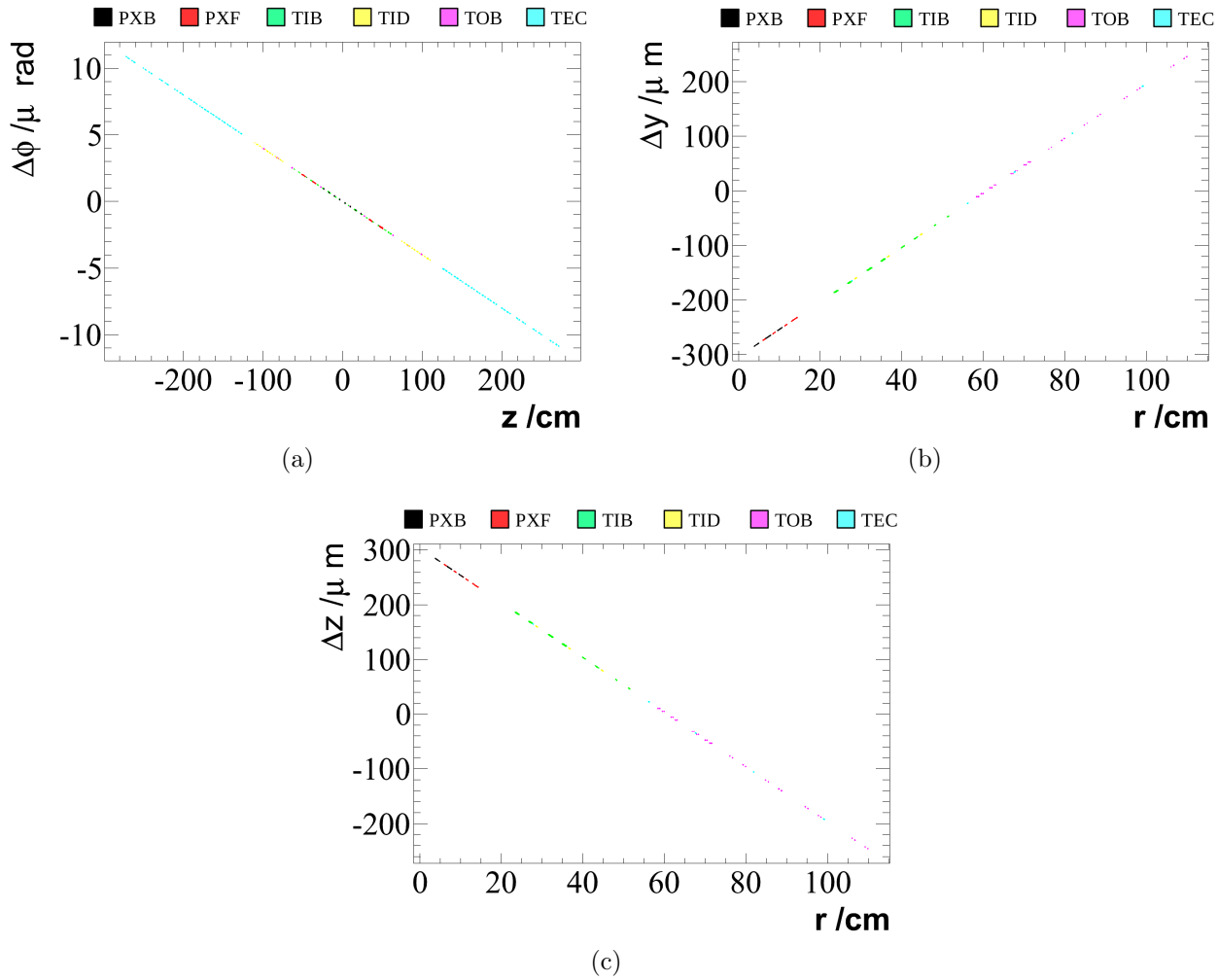

Figure 7.4: The misalignment for the three weak modes : twist (a), sagitta(b) and telescope (c). Linear misalignment functions are applied to the six tracker parts. The different components are marked with six different colors. A single point shows the position for the single or grouped modules. This depends on the granularity during the alignment procedure.

One can see the significant improvements in the position of the tracker components. The twist weak mode has an almost perfect recovery, figure 7.5, (a) with an improvement of an order of magnitude. The sagitta (b) and telescope (c) weak modes have a slightly worse recovery to the true geometry. In addition during the telescope realignment the TOB and TIB tracker parts were fixed for testing reasons. This was done to check if the realignment procedure is possible with not all tracker detector parts. Thus on the figure they are not shifted at all.

7.3.5 Summary

This study of weak modes in the alignment was perfomed using 2012 data samples. The alignment procedure was done on top of the 2012 official geometry object with the best estimated (true) parameters at that moment. A “misalignment” procedure was applied to the true geometry for the simulation of three weak modes : “Twist”, “Sagitta” and “Telescope”. This study presented explanations and solutions for the resolution of weak modes in the alignment fit. Certain systematic distortions of the tracker geometry are very challenging for track-based

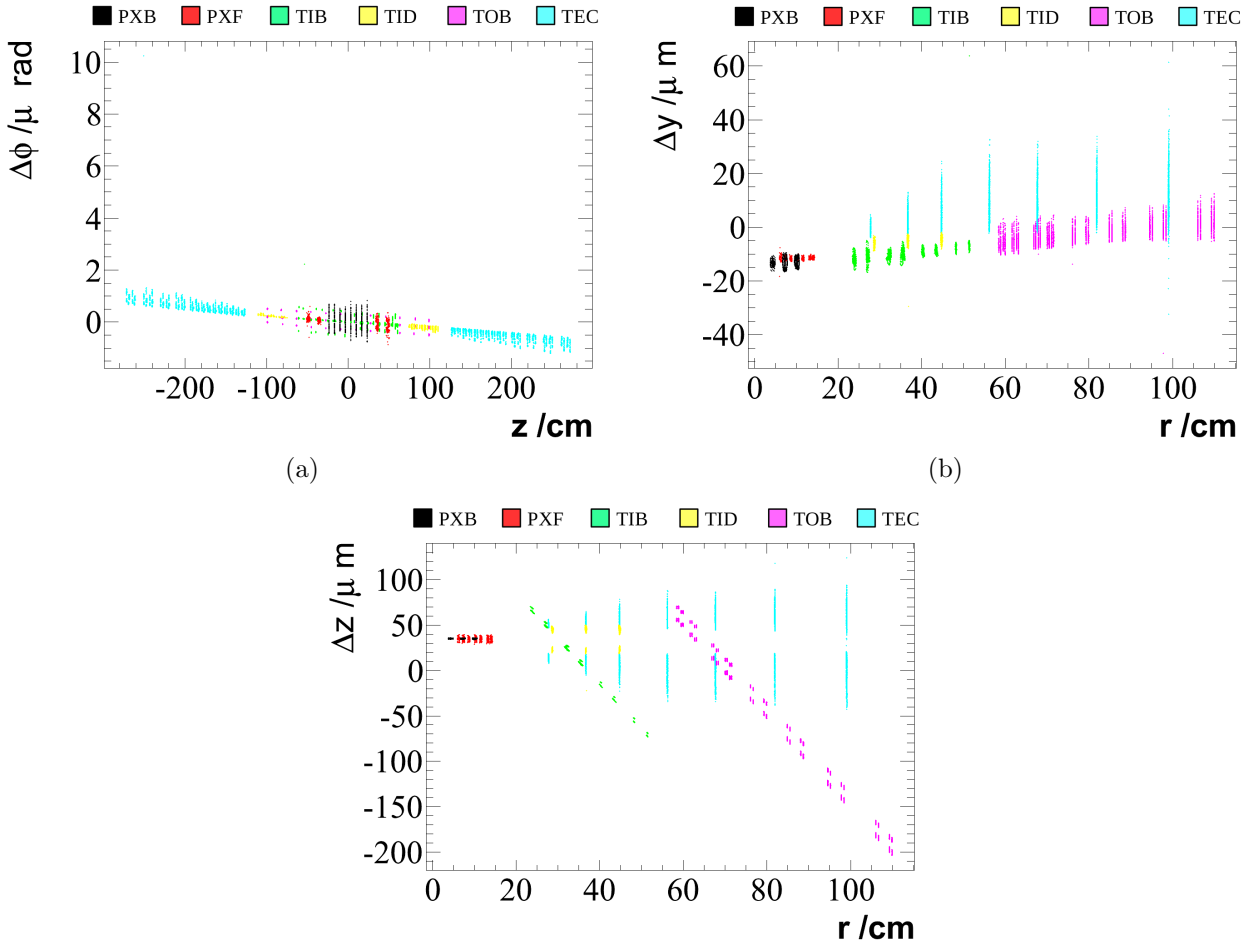

Figure 7.5: The "realignment" procedure for the three weak modes : twist (a), sagitta(b) and telescope (c). The figures show the module parameter differences between the true geometry and the geometry after two alignment itterations. The different subdetectors are marked with six different colors.

alignment. On top of the "misalignment", alignments with two iterations for the three weak modes were prepared. A good recovery has been demonstrated for the twist and sagitta weak-modes. The telescope alignment should be investigated further. Figure 7.5 shows that the weak modes can be controlled by combining different data types in the alignment fit.

7.4 Z-rescaling weak mode

In the tracker alignment with Millepede-II ([30]) significant Z-shifts of the TEC and TID disks proportional to the z-axis have been observed. The first indication was observed with a minimum bias data sample. The effect is present for both the Monte Carlo and data samples. It is present in collision data but not in cosmic samples with magnetic field at (0 or 3.8) T . The effect was studied on minimum bias, cosmic and on isolated muon Monte Carlo events. Figure 7.6 shows the effect which appears on a different data samples except of a cosmic data. For the minimum bias sample the maximum shift in the z direction up to 1 mm was observed. For the isolated muon in Monte Carlo samples maximum shift is 15 mm. For the cosmic data this issue was not observed (Fig. 7.6(c)). During this study the reason for this issue was not found due to the limited time to perform the technical tasks. The issue was effectively resolved by combination of minimum bias and cosmic data, which is described in details in Section (7.4.2). This chapter shows a significant amount of tests which were performed with ideas which came from different points of view on the issue. The study can be an important base for those who continue the analysis.

7.4.1 General information

Plots explanation. All the plots in this chapter show differences of the parameters with respect to the chosen initial geometry parameters. The initial geometry is the geometry obtained from the previous official CMS alignment and shows the best picture of all possible parameters which one can measure for that time point. Different colors mean that the parameters are related to different detector parts. They are the Pixel Barrel detector (PXB, black color), Pixel Forward detector (PXF, red color), Tracker Inner Barel (TIB, green color), Tracker Inner Detector (TID, blue), Tracker Outer Barrel (TOB, pink) and Tracker EndCaps (TEC, turquoise color).

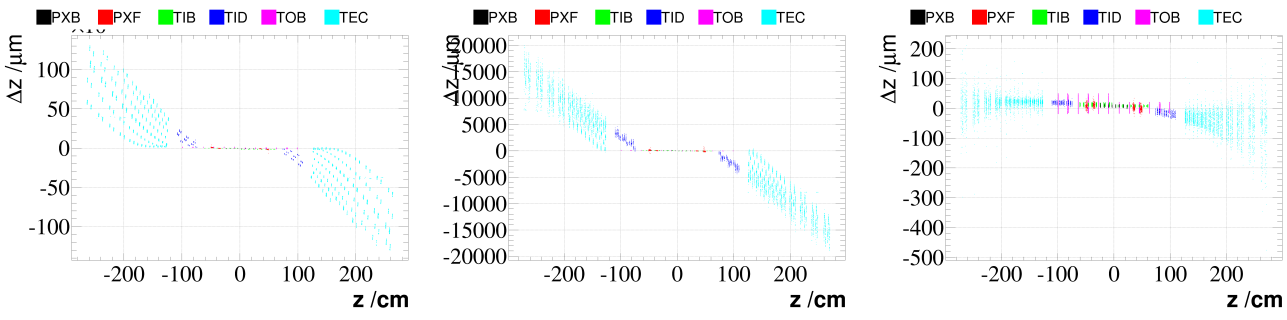

(a) (b) (c)

Figure 7.6: The $dz - z$ distribution for three data samples: minimum bias (a), isolated muons (b) and cosmic data samples (c).

The comparing procedure. In this study the initial geometry is used as a reference point. That means that any obtained parameter from the alignment procedure is compared with the corresponding parameter of the initial geometry. All distributions which show that difference

are obtained as the difference (res = a - b) of the alignment parameter obtained from the alignment procedure (a) and the initial geometry parameter (b).

The high level alignment procedure. The reference tracker part is BPIX. The BPIX detector was chosen among others as the one which was installed with high precision and as the most inner part of the tracker. All other components are aligned with respect to the BPIX detetor. All detector modules are combined into the big detector parts. The high level alignment procedure (HL alignment) means that in the fit procedure additional constraint is present which are coming from the combination of modules into big detector parts. The included constraints are related to the position and rotation of the global tracker blocks such as TIB, PXB, TID and others. This also means that every single module inside the high level modules is also involved in the alignment, but they can act only together on the chosen parameters of the high level modules. Each big detector part has its own three position and three rotation parameters.

The module level alignment procedure. This is the alignment procedure with module granularity of the tracker. All the single module parameters are taken into account together with the high level granularity parameters. This procedure takes approximately ten times more than time of high level alignment (around 24 hours with all possible data samples).

The data and Monte Carlo samples. In this study minimum bias data samples were used with a total number of events equal $\sim$ 2 million events. The number of isolated muon Monte Carlo events is around 15 millions. The total number of cosmic muon events is around 5 millions. More detailed information about samples can be founded here [137].

7.4.2 Tests Performed

- **HL structure.** The first step is a test if the z-rescaling weak mode appears with the high level structure alignment. After the alignment procedure some shifts were observed but with not huge effect. Figure 7.7 shows the comparison between the initial geometry and the geometry obtained after the high level alignment procedure ([30]).

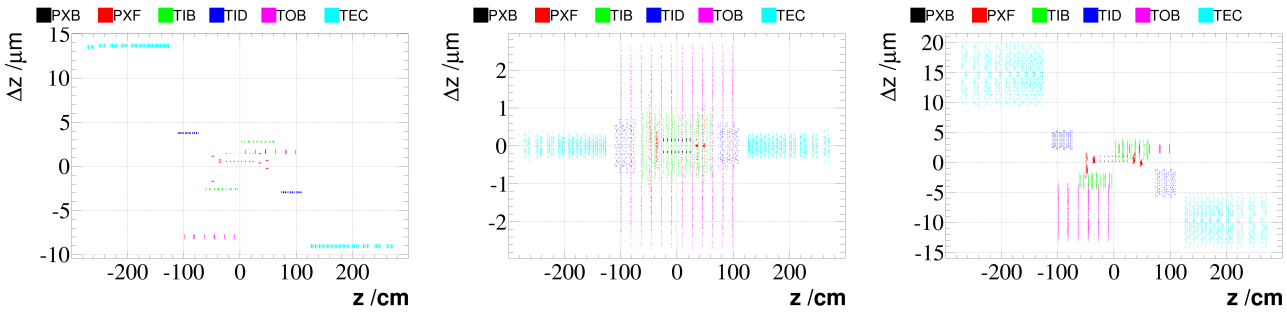

Figure 7.7: The alignment procedure control plot of the $\Delta z - z$ distribution with only position parameters included (a), rotation only (b) and both position and rotation parameters included (c), performed for the high level tracker structure.

This test shows small differences (up to 15 μm) between the initial geometry and the geometry obtained after the high level alignment procedure, but they do not have a dependence from

the z-axis. This effect can be explained by general shifts of the tracker detector parts. It has to be studied carefully, but obviously it is not related to the z-rescaling weak mode and will not be considered in this study. The important point here is that this issue mainly comes from the alignment with position coordinates only (Fig. 7.7(a)) while for the rotation parameters alignment (Fig. 7.7(b)) it does not appear and is slightly reduced in the combination of the position and rotation alignment parameters (Fig. 7.7(c)). The minimum bias sample has a P_T cut on tracks which is greater than 1 GeV. All other tests are carried out with the module level alignment.

- **Fixed End Caps.** The test was performed with fixed End Caps for TID, TEC, with module level alignment.

From figure 7.8 one can see that the z-rescaling effect disappeared but instead some spread of TOB and other detector part modules is present. In this test the end caps for TID and TEC were fixed which means that the corresponding high level parameters are not involved in the alignment procedure and are obtained as relative values to the TPB part.

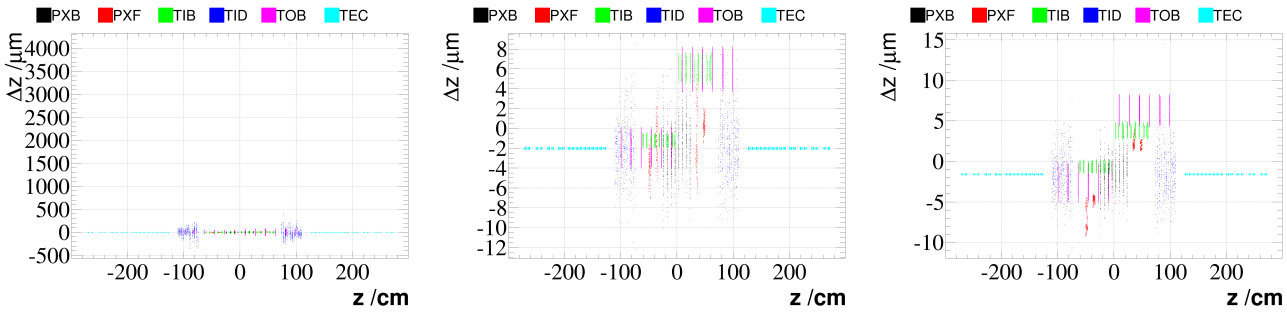

(a) (b) (c)

Figure 7.8: The alignment procedure with fixed End Caps for the TID, TEC parts. The minimum bias data sample is shown in the plot (a), cosmic data only in (b) and both minimum bias and cosmic data samples are shown for the plot (c).

One can see that for all distributions (Fig. 7.8), the TEC and TID parts are not shifted. In the case with TID some distribution is still present since module shifts are allowed if the average level corresponds to the fixed parameters. One can see that a source of other tracker part shifts is caused by the impact of the cosmic data (Fig. 7.8(b)). But those shifts are relatively small (up to 10 μm) and are not considered in this study. This test shows that the z-rescaling effect could be particularly related to the TID and TEC End Caps.

- P_T **dependencies.** To collect more information an analysis with P_T dependencies for the minimum bias data sample was performed. This test shows a reduction of the z-rescaling effect if the P_T cut is increased (Fig. 7.9).

Figure 7.10 shows that the reduction of the effect is related to the reduction on the number of tracks which are registered in the End Caps. In this case it is not clear if the P_T cut has a real impact to the z-rescaling weak mode. Figure 7.10 shows the occupancy of TEC for the P_T

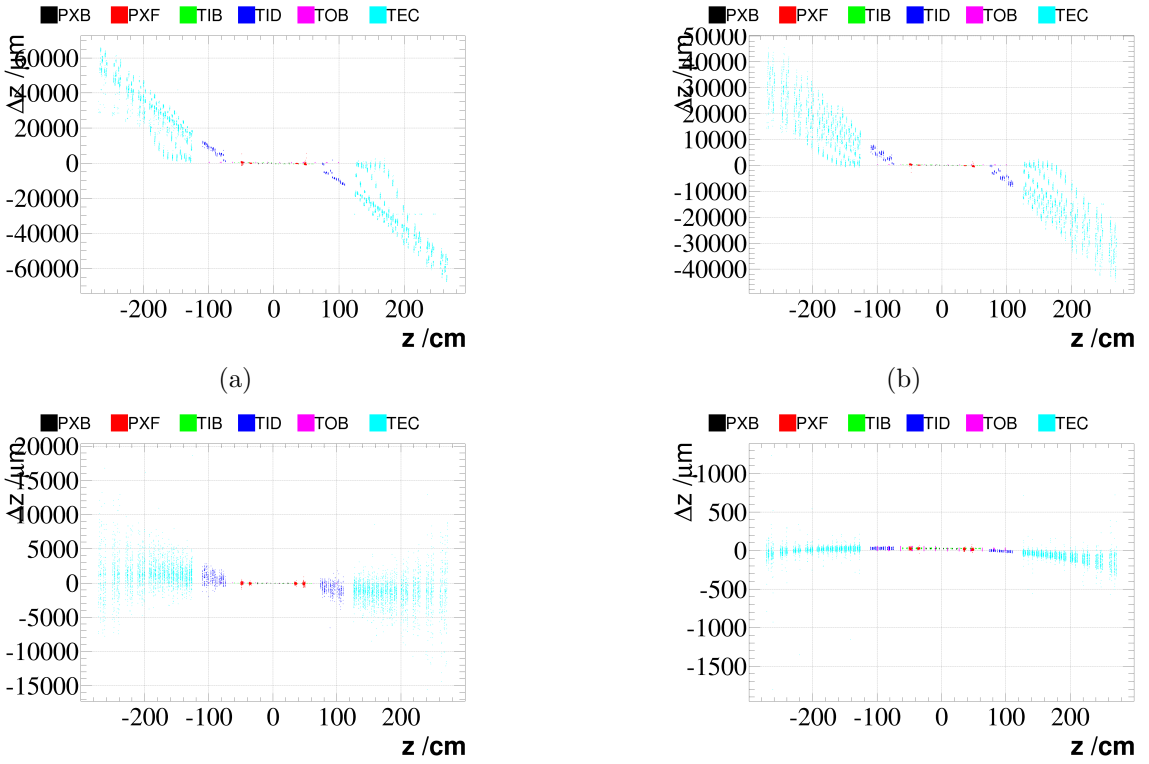

Figure 7.9: The alignment procedure with different P_T cuts. The minimum bias data sample with standard cut on tracks $P_T > 1\ GeV$ (a), minimum bias data with $P_T > 4\ GeV$ (b) , minimum bias data with P_T cut $> 7\ GeV$ (c) and both minimum bias and cosmic data samples are used for the alignment plot (d) with cut on tracks transverse momentum $P_T > 7\ GeV$.

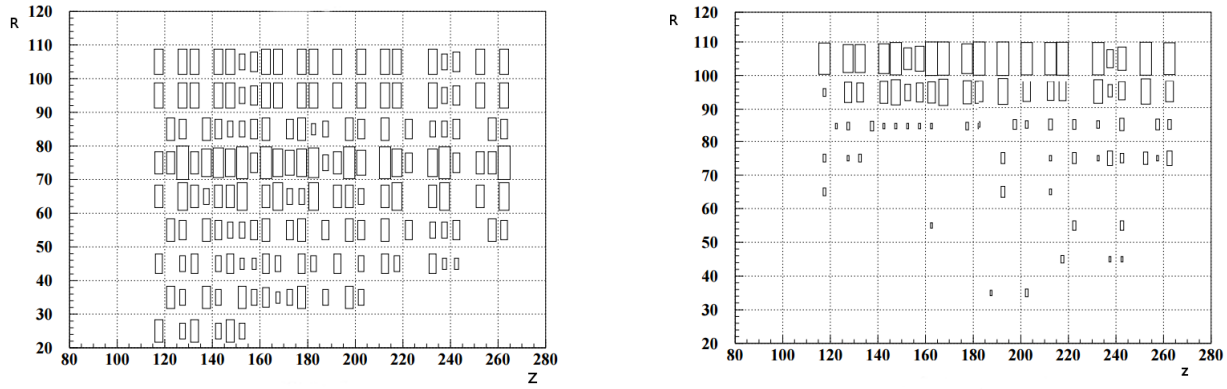

Figure 7.10: Figure shows occupancy of TEC for the two cuts on track P_T : 1 and 7 GeV. Both distributions show dependence r from z coordinates, where r is quadratic function of x and y coordinates. Both plots show the number of tracks, as rectangles with different size, for mimum bias tracks which were detected by TEC and with cut on $P_T > 1\ GeV$ (left, (a)) and $P_T > 1\ GeV$ (right, (b)). Plots were obtained by [128].

cut on 1 and 7 GeV [128]. Since minimum bias data samples consist of low P_T tracks one can observe a significant reduction of the number of tracks.

- **Cosmics as "real data".** For the cosmic data the z-rescaling effect is not observed. In this test we tried to simulate "collision" like data from the cosmic data sample by playing

with the dZ cut. The idea of this simulation is an observation of the z-rescaling effect with the cosmic data as well.

Cosmic muon tracks are different from the collision tracks because of their straight line tracks which go through the detector and cross it in any random z-coordinate . In this test the z-coordinate of such tracks is restricted to be close to the interaction point in the sense of the z-axis. This cut will significantly reduce the cosmic data statistics but on other hand it will be a rough simulation of collision data. The cut parameter which was applied to the cosmic muon

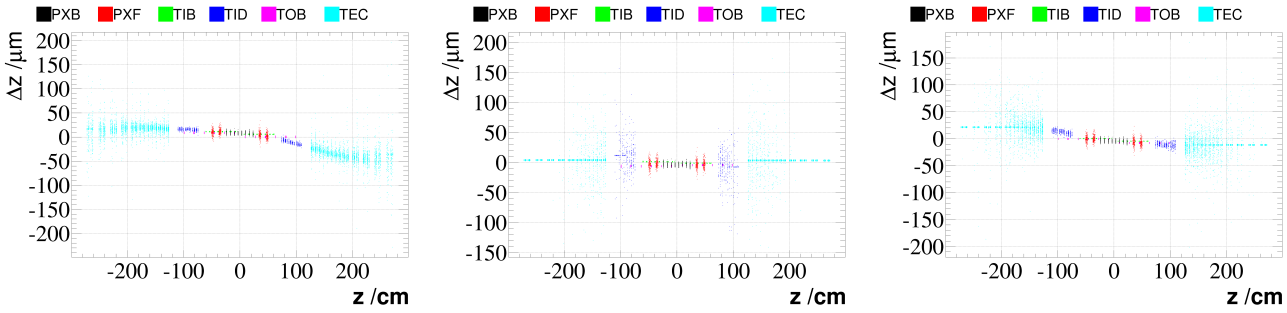

(a) (b) (c)

Figure 7.11: This figure shows $\Delta z - z$ distributions in case with no cuts (a), with cut 0.5 m (b) and cut 1 m (c) on the z-coordinate of cosmic tracks.

track z-coordinate in this test was chosen as 1 m (Fig. 7.11(c)) and 0.5 (Fig. 7.11(b)). In such an approximation all tracks which have the z-coordinate less than the chosen cut parameter are considered as collision tracks which go in opposite directions. Of course, this is a very rough approximation, but in such a test it can allow us to get more information and helps to understand the z-rescaling effect a bit better. This test shows that with such simulation one does not observe z-rescaling effect by using the cosmic data sample. An important point is that unlike cosmic data we observe this effect for minimum bias. And it is an important part of the work to find out why this effect does not appear for both data samples. Cosmic tracks have special characteristics which make them different from the minimum bias tracks. Cosmic tracks have a higher P_T spectrum, and due to their nature they break the cylindrical symmetry of the detector. With this test collision like tracks were selected and no z-rescaling effect was observed (Fig. 7.11). This could mean that some special characteristics of the cosmic data tracks are indeed creating such a restriction that does not allow z-rescaling to be present. A good start point for future studies could be a careful comparison of all alignment steps which are applied to the cosmic and collision data samples.

- **TEC/TID disk constraints.** This test was performed to show if it is possible to reduce the z-rescaling effect with introducing an additional alignment constraints for TEC and TID disks. Constraints were prepared as follows: the first disk (which is closest to the interaction point) is allowed to make a movements during the alignment procedure. The remaining disks are moving in the same directions as the first one. The constraints are implemented independly for the "-z" and "+z" directions (Fig. 7.12). In this test an isolated muon sample was used.

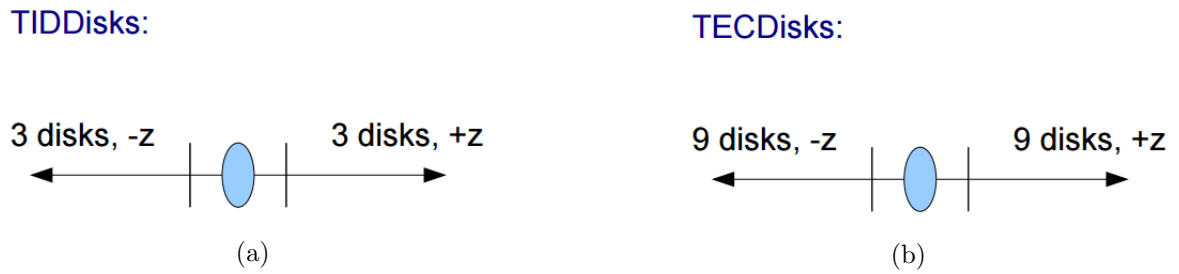

(a) (b)

Figure 7.12: Schematicall explanation of how the TID and TEC end cap disks were constrained.

Figure 7.12 shows a TID sketch (a) that has 3 end cap disks in which 2 of them (closest to the interaction point) are allowed to make a movement during the alignment procedure. Other disks are moving in the same direction as the first one from each z-direction. This constraint is separated for the positive and negative direction of the z-axis. At the same time, the same constraint was applied to the TEC disks (Fig. 7.12(b)) with the difference that it has 18 disks instead of 6 for TID. Thus, at the end of the alignment procedure about 20 constraints were applied to the end caps (Fig. 7.13).

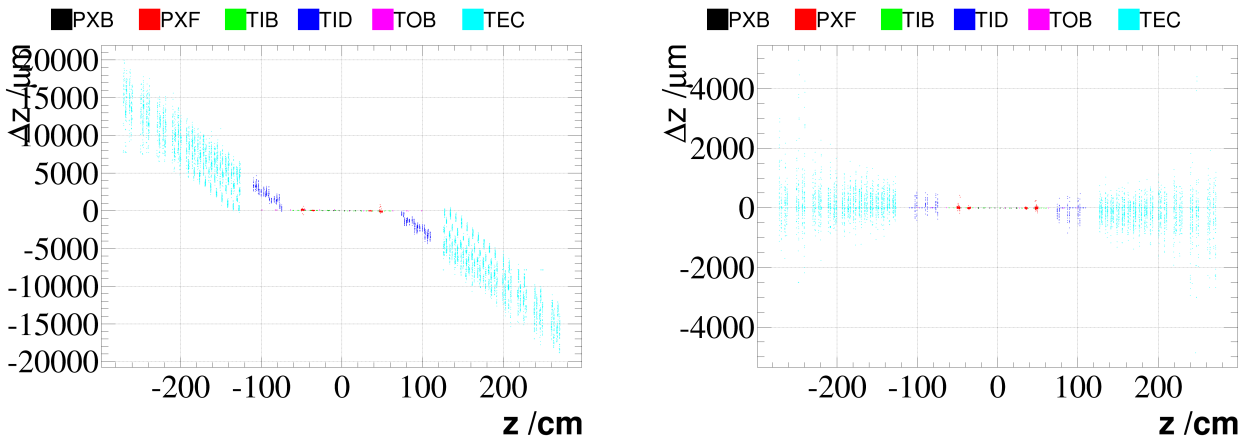

(a) (b)

Figure 7.13: The $dz - z$ distribution of the alignment procedure without (a) and with (b) the TID and TEC end cap disks constraints.

Figure 7.13(b) shows the result of the alignment procedure for the isolated muon data sample. Here it has to be mentioned that for the isolated muons data sample the same z-rescaling effect was observed (Fig. 7.13(a)). One can see that the constraints eliminated the z-rescaling effect. A significant spread of the TEC modules is still present. This might be eliminated by adding the cosmic data as was shown in one of the tests above. This test shows again that the z-rescaling effect directly depends from the TEC and TID end caps alignment parameters. For a future study one can start from this idea and make a careful investigation how these parameters are fitted with the alignment procedure and try to find out what is going in the wrong direction.

Other tests were performed and do not make a huge effect on the z-rescaling issue [127]. They are : a "**Skyline/Bandwidth option test**", which test a few algorithms of the error

matrix calculation. Indeed some of the tests obtained nice results but did not solve the issue. The next test is the test with "**TrajectoryFactory**" setup. This test uses different modes to fit the track trajectory. As a conclusion for this test one can say that all modes work almost the same and did not help to solve the z-rescaling issue. One of the interesting tests is a study of "**correlation between position and slope**" for cosmic and collision data tracks separately. The detailed information may be found at the CMS twiki page [127].

- **A combination of the cosmic and minimum bias data samples.** For this study around 2 million tracks from the cosmic and minimum bias samples were used. Figure 7.14 shows a decrease of the effect by a factor two with the increased amount of the cosmic data in the combination. The most important behaviour is that the z-rescaling effect is strongly eliminated by the increasing number of cosmic data tracks which take part in the alignment procedure. With different amount of cosmic muon tracks, the elimination factor of the z-rescaling effect is not linear.

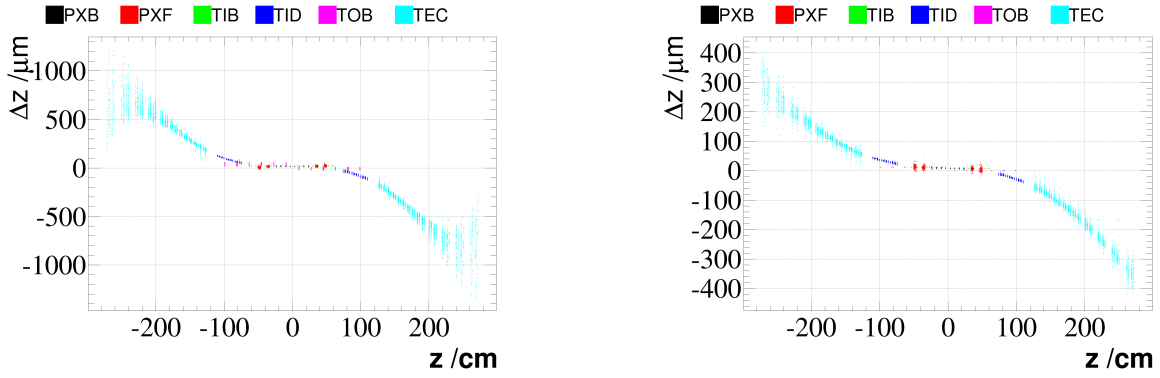

(a) (b)

Figure 7.14: The alignment procedure control plot of the $dz - z$ distribution with cosmic data included in the proportion 1:1.5 (cosmic vs minimum bias tracks) (a) and in the proportion 1:1 (b).

7.4.3 Results and Next Steps

All performed tests gave us additional information about the z-rescaling effect from different points of view. A significant number of tests such as "High level structure" alignment only, alignment with fixed end caps, impact of P_T dependence of the tracks on the alignment procedure, simulation of cosmic data as collision data, introducing TID , TEC end caps disks constraints and other important tests show important results.

As was mentioned at the beginning, this study does not solve the z-rescaling issue. The goal was to accumulate as much information about the problem as possible and find some special behaviour which might help to solve the issue. One can extract interesting conclusions from those tests. The z-rescaling effect may have a dependence on the track P_T values as was shown in one of the tests above. The issue mainly comes from the TEC and TID end caps. The additional TEC, TID constraints solve the problem, but this it can not be used in the final

alignment results because it ignores a lot of parametes which are important to be free during the fit procedure.

The effect is significantly reduced by a combination of minimum bias data with other data samples such as a cosmic data sample. The ratio in 1:5 of minimum bias and cosmic muon tracks reduces the z-rescaling effect up to tens of micrometers which is relatively acceptable for the official alignment. Thus for the final 2015 alignment procedure the combinations with other data samples in a good proportion was used. This method helps to completely eliminate the z-rescaling effect, but definitely further studies in the direction of the z-rescaling issue are very important to see the complete picture and to find the reason for this weak mode.

Summary and Outlook

Inclusive beauty quark production has been measured from dimuon events. For the HERA analysis the data collected by the ZEUS detector in 2003-2007 at the centre-of-mass energy of $\sqrt{s} = 318$ GeV with integrated luminosity of 376 pb^{-1} were used.

The dimuon events in this analysis mainly consist of beauty, charm, heavy quarkonia, BH, and light flavour events. The beauty fraction of the dimuon events was found by comparing unlike- and like-sign dimuon events. The charm fraction was initially determined by using the charm contribution from the similar event topology of a $D^*\mu$ sample. The isolated part of the dimuon invariant mass distribution was used to normalise the heavy quarkonia and BH contributions. The light flavour background was extracted as the difference between the like-sign dimuon samples of the data and the beauty fraction. The assumption that the light flavour background has almost no charge correlation and therefore contains almost equal number of unlike- and like-sign dimuon has been used to extract the unlike-sign light flavour contribution as a reflection of the like-sign dimuon light flavour events with an additional small correction. The total and differential cross sections in bins of $p_T^\mu, \eta^\mu, \Delta R^{\mu\mu}$ and $\Delta\phi^{\mu\mu}$ were calculated. The additional fit procedure based on secondary vertex information was used to improve the total cross section calculations. The results were compared to, and show good agreement with, the previous analysis and NLO predictions.

As the technical part of this thesis a study of the systematic shifts of the CMS detector parts called weak modes was done. A study of weak modes in the CMS tracker alignment was performed using 2012 data collected by the CMS detector of the LHC. The alignment procedure was applied on top of the 2012 official geometry with the best estimated (true) parameters at that moment. A "misalignment" procedure was applied to the true geometry for the simulation of the three weak modes: "Twist", "Sagitta" and "Telescope". A study of explanations and solutions for the resolution of the weak modes in the alignment fit has been performed. A good recovery has been demonstrated for the "Twist" and "Sagitta" weak-modes while the telescope alignment should be investigated further.

A detailed study of the weak mode related to the systematic shifts such as $\Delta z = c \cdot z$ in the CMS tracker detector has been done. All performed tests gave additional information about this mode from different points of view. A significant number of tests such as "High level structure" alignment only, alignment with fixed end caps, impact of P_T dependence of the tracks on the alignment procedure, simulation of cosmic data as collision data, introducing TID and TEC end cap disk constraints and other important tests show important results which

might help to solve the issue. The reason for this weak mode has not been found in this study but the accumulated information might help to find it in the future. One can extract interesting conclusions from the tests which have been performed: the effect may have a dependence on the track p_T, the issue mainly comes from the TEC and TID end caps. Additional TEC and TID constraints solve the problem, but this can not be used in the final alignment results because it ignores a lot of parameters which are important to be free during the fit procedure. The effect is significantly reduced by a combination of minimum bias data with other data samples such as a cosmic data sample.

Detailed explanations about the track helix parametrisations in the ZEUS and CMS experiments is presented in Appendix A, B. A transformation of the track parameters from the CMS into the ZEUS format has been developed as presented in Appendix B. In Appendix C, first steps towards a synergy between corresponding ZEUS and CMS analysis concepts have been explored.

The main part of this thesis combines a physics analysis for the ZEUS experiment and technical work at CMS detector. The ZEUS analysis obtained interesting physics results for beauty production, while the technical part naturally complements the physical part and helps to get correct and precise data for future CMS analyses.

Appendix A: Helix parametrization at CMS

General information

A charged particle has a helix trajectory in a solenoidal magnetic field. For the CMS detector the magnetic field is uniform and directed in the positive "x" direction in the global coordinate system. The x-axis is directed horizontally and points to the center of the LHC ring. The y-axis is directed vertically up. The azimuthal angle ϕ is measured from the x-axis in the $x-y$ plane. The radial coordinate in this plane is r. The polar angle θ is measured from the z-axis in the $r-z$ plane. All angles are given in radians. The transverse momentum P_t, is defined as the momentum projection into the x-y plane, $P_t = P \cdot sin\theta$.

A helix parametrization can be defined in many different ways. For CMS it is defined by a set of five track parameters: $\boldsymbol{(qoverp, \lambda, \phi, d_{xy}, d_{sz})}$ [123].

- $\boldsymbol{qoverp} = \frac{q}{|p|}$: signed inverse of momentum $[GeV/c]^{-1}$
- $\boldsymbol{\lambda} = (\frac{\pi}{2} - \theta)$ is the polar angle at the given point
- $\boldsymbol{\phi}$ is the azimutal angle at the given point
- $\boldsymbol{d_{xy}}$ is defined as: $d_{xy} = v_y \cdot cos(\phi) - v_x \cdot sin(\phi)$ [cm]
  - (v_x, v_y, v_z) is a reference point on the track
  - the (0,0,0) point is the center of the coordinate system. This can be the center of the global coordinate system or the beam spot or some other defined point chosen as origin.
  - d_{xy}, in general, is the signed distance from the defined origin to some reference point on the track in the $x-y$ plane. In the case when the reference point is (0,0), d_{xy} is geometrically the distance in the $x-y$ plane between the (v_x, v_y) and (0,0) points. The defined origin may be chosen as the beam spot, in this case d_{xy} is the distance in $x-y$ plane between the beam spot and (vx, vy) points.
- $\boldsymbol{d_{sz}}$ is defined as: $d_{sz} = v_z \cdot cos(\lambda) - sin(\lambda) \cdot (v_x \cdot cos(\phi) + v_y \cdot sin(\phi))$ [cm]

  - $s-z$ plane : the s-axis is not r. It is defined as $s = v_y \cdot cos(\phi) - v_x \cdot sin(\phi)$ for the coordinate (v_x, v_y). The $s-z$ plane is defined by the s and z axes, where (v_x, v_y) is the point of closest approach in the x-y plane.
  - d_{sz} : is the signed distance in the $s-z$ plane between the points (0,0,0) and (v_x, v_y, v_z)

- additional variables:
  - R : track circle radius
  - $\rho = q \cdot R = \frac{q \cdot |p| \cdot sin(\theta)}{0.0029979 \cdot B_z}$: signed track circle radius
  - $dz = \frac{dsz}{sin(\theta)}$ is the longitudinal impact parameter

There are only two cases when d_{xy} and d_{sz} provide sensible definitions of the distance from the (0,0,0) point to (v_x, v_y, v_z) [123]:

1. If (v_x, v_y, v_z) already is the point which corresponds to the minimum transverse distance of the helix to (0,0,0)
2. If (v_x, v_y, v_z) is close enough to it that the difference between the exact particle trajectory and a straight line is negligible.

This is usually true for tracks with high momentum. The important point is that the parameters d_{xy} and d_{sz} are calculated with respect to the relative point (0,0,0).

Because of the magnetic field direction, the helix axis will be parallel to the z-axis. Due to the Lorentz force equation, positively charged particles move in the clockwise direction in the x-y plane [124], while negative charged particles move in the counter clockwise direction. The sign of d_{xy} is positive when the z-axis is inside of the track helix and negative when z-axis is outside the track helix.

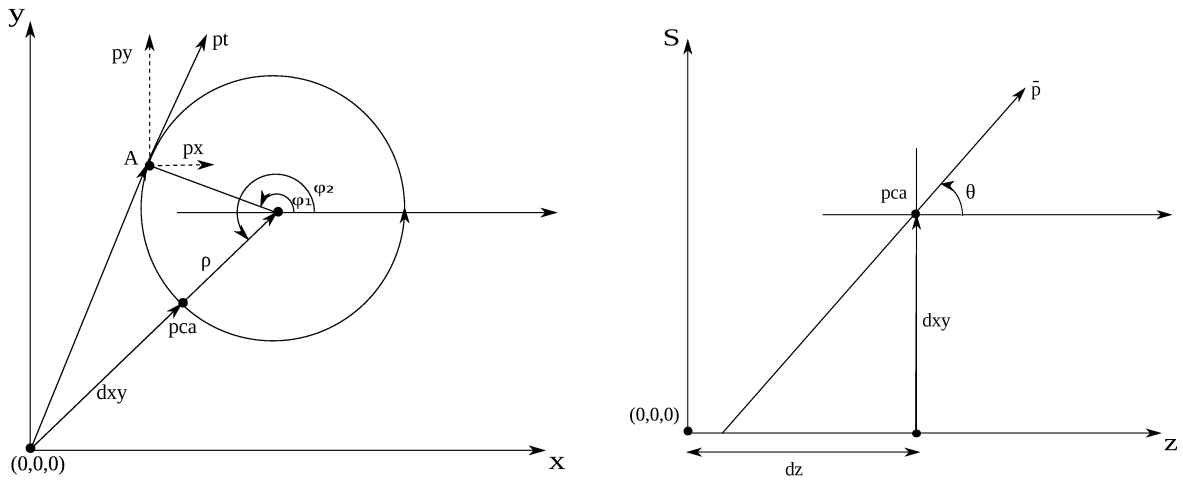

(a) x-y projection (b) s-z projection

Figure 7.15: Projection of the helix trajectory on the $x-y$ plane. A - some reference point on the track trajectory. pca - point of the colsest approach from (0,0,0) to the track circle. ϕ_1 - azimutal angle to the reference point. ϕ_2 - azimutal angle to the point of closest approach. $\phi_3 - \phi_2 = \pm\frac{\pi}{2}$ [124].

For the point of closest approach, from the triangle (see Figure 7.15(a)), one can extract the parameters in the cartesian coordinate system:

$$\begin{aligned} x_{pca} &= -d_{xy}^{pca} \cdot sin(\phi_2) \\ y_{pca} &= d_{xy}^{pca} \cdot cos(\phi_2) \\ z_{pca} &= dz_{pca} \end{aligned} \tag{7.4}$$

It is important to note that the reference point can be any point on the track, chosen for each track individually. The definitions (7.4) are valid only if the point (v_x, v_y, v_z) is the point of closest approach $(x_{pca}, y_{pca}, z_{pca})$. In any other case one has to know the transformation equations between the coordinates of the point on the track circle and the coordinates of the point of closest approach, thus in the general case [122]:

$$\begin{aligned} x_A &= x_0 - d_{xy}^{pca} \cdot sin(\phi_2) + \rho \cdot (sin(\phi_2) - sin(\phi_1)) \\ y_A &= y_0 + d_{xy}^{pca} \cdot cos(\phi_2) - \rho \cdot (cos(\phi_2) - cos(\phi_1)) \\ z_A &= z_0 + dz_{pca} + \rho \cdot tan(\lambda) \cdot (\phi_2 - \phi_1) \end{aligned} \tag{7.5}$$

In the case of the CMS experiment the helix parameters with respect to (0,0,0), thus $(x_0, y_0, z_0) = (0,0,0)$ were extracted.

The calculations for the momentum are much easier. Since we are interested in the momentum components (p_x, p_y, p_z) at (v_x, v_y, v_z) we can use the standard utility "$trackRef->parameter()$" to extract ϕ_1 from it. This will be ϕ not for the PCA but the one related to our reference point. A accordance is $\theta_1 = \theta_2 = \theta$. From the definitions of first three helix parameters and Figure 7.15, one can obtain formulas for the momentum component calculations:

$$\begin{aligned} p &= \frac{q}{\boldsymbol{qoverp}} \\ p_t &= p \cdot sin(\theta) \\ p_x &= p_t \cdot cos(\phi_1) \\ p_y &= p_t \cdot sin(\phi_1) \\ p_z &= p \cdot cos(\theta) \end{aligned} \tag{7.6}$$

Technical documentation

- To get the information about the ***magnetic field*** for each track in some point (x,y,z):

  $ESHandle < MagneticField > magfield;$
  $iSetup.get < IdealMagneticFieldRecord > ().get(magfield);$
  $constMagneticField * b = \& * magfield;$

$GlobalPointgp(x, y, z);$
$GlobalVectorbvec = b- > inTesla(gp);$

- It is possible to create a transient track collection [121] and then extract ***fivehelix*** parameters.

  $enumindexi\_transverseCurvature = 0, i\_theta, i\_phi0, i\_d0, i\_dz;$
  $doublep1 = trackRef- > parameter(i\_transverseCurvature);$
  $doublep2 = trackRef- > parameter(i\_theta);$
  $doublep3 = trackRef- > parameter(i\_phi0);$
  $doublep4 = trackRef- > parameter(i\_d0);$
  $doublep5 = trackRef- > parameter(i\_dz);$

- A very useful util is the ***TrajectoryStateClosestToPoint*** [125] function. It gives the possibility to calculate the closest distance to the track circle with respect to some chosen point. In the following tests the point (0,0,0) was chosen as the center of the global coordinate system. The usage is:

  $for(vector < TransientTrack >:: iteratorgnr\_trk\_it = general\_tr.begin();$
  $gnr\_trk\_it! = general\_tr.end(); gnr\_trk\_it + +)\{$

  $constreco :: TrackReftrackRef = (gnr\_trk\_it- > trackBaseRef()).castTo < reco :: TrackRef > ();$
  $TransientTracktransientTr = theB- > build(trackRef);$
  $GlobalPointvert(0., 0., 0.);$
  $TrajectoryStateClosestToPointtraj = transientTr.trajectoryStateClosestToPoint(vert);$

  $doublep1\_1 = traj.perigeeParameters().transverseCurvature();$
  $doublep2\_1 = M\_PI/2. - traj.perigeeParameters().theta();$
  $doublep3\_1 = traj.perigeeParameters().phi();$
  $doublep4\_1 = -1 * traj.perigeeParameters().transverseImpactParameter();$
  $doublep5\_1 = traj.perigeeParameters().longitudinalImpactParameter(); \}$

Checking the calculations

Using formula 7.5 one can calculate reference point coordinates $(x_{ref}, y_{ref}, z_{ref})$ with known helix parameters obtained from the data. From the other hand one can extact reference point coordinates directrly from the data sample. The comparison of the calculated values with values obtained from data sample is important to check understanding of the CMS helix parametrization. The $(x_{ref}, y_{ref}, z_{ref})$ coordinates the comparison is shown in the figure 7.16.

From the plots 7.16, one can see that the difference is up to $0.1(\mu m)$. This small difference means that $(x_{ref}, y_{ref}, z_{ref})$ coordinates calculated with using tracks helix parameters is correct and is in a good agreement with the original coordinates from the reference point, obtained from the CMS data. In turn this mean that helix parameterisation of the CMS detector is well understood. The small difference may come from the double precision calculations which becomes slightly worse because a lot of mathematical operations which have been done. For

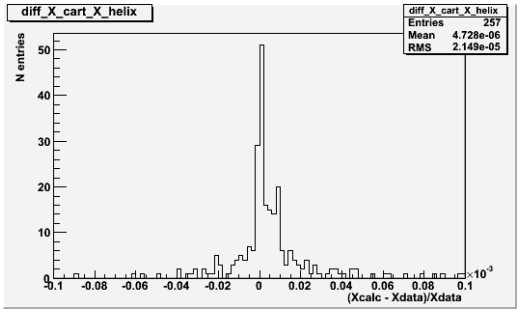

(a) v_x *checks*

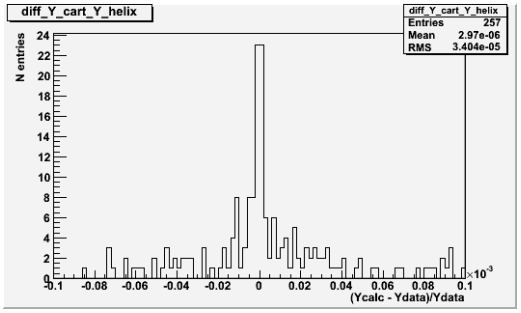

(b) v_y *checks*

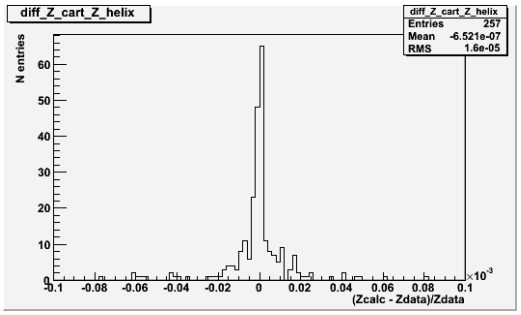

(c) v_z *checks*

Figure 7.16: Difference between the calculated reference point coordinates with formulas 7.5 and coordinates obtained from the CMS data, normalized by last. Distributions present difference for three vertex position coordinates.

the (p_x, p_y, p_z) difference is much more less, and one can say that those calculated parameters are identical with corresponding momentum components obtained from the CMS data.

Summary

The main goal of this section is to obtain the knowledge about the correct track helix parametrization in the CMS experiment. This section contains a detailed explanations about this parametrization as well as a short description of the code tools which were used. The coordinates of the reference point where calculate with using formula 7.5 and compared with corresponding coordinates obtained directly from data. Good agreement of such comparison means that the helix parameterisation of the CMS detector is well understood. The maximum difference is up to $0.1(\mu m)$ which might be explained with the double precision which is decreased after many mathematical calculations.

Appendix B: Helix parametrization at ZEUS

The two collaborations ZEUS and CMS use different track parametrizations. The ZEUS experiment has performed a lot of physics analysis, the experience of which can be used in other experiments. Especially considering the fact that there is a tendency to increase the energy of particle collisions, in the future it may be useful to consider the experimental ultrahigh energy data in the combination with data obtained from the ZEUS experiment. For all analyses which are using tracks, the main difference for many experiments is the track parametrization, which is essentially a problem when one wants to combine data from them and perform one analysis which is based on it.

A general Information

The main idea of the study described in this section was to develop a transformation tool which can convert the track parametrization from the one experiment to the other. A general tool there should be developed which converts all event parameters such as track energy, vertex and track parametrization etc. For the most common parameters such particle energy or trigger bits etc., the transformation procedure should be relatively straightforward since their meaning is common for most experiments. On the other hand, a track transformation is quite a challenge because the tracks are parameterized with a non-identical helix parametrization and the transformation of such a system with its covariant matrix is a difficult task.

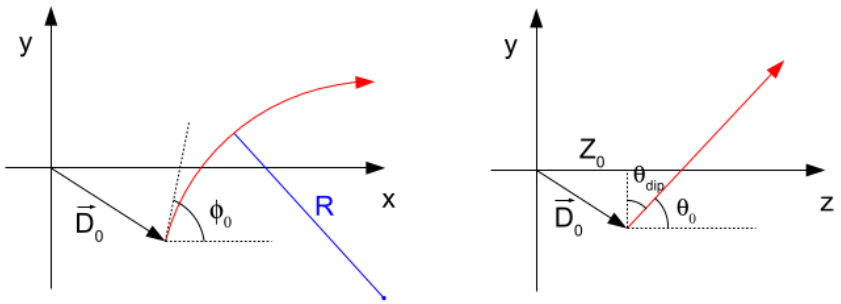

Figure 7.17: The track sketch projection on the xy and the z planes. The five track parameters (ϕ_0, Q/R, $Q \cdot D_0$, z_0, $cot(\theta_0)$) are shown. The image is taken from [113].

The CMS track helix parametrization is described in the Appendix A. The ZEUS experiment

uses five parameters which will be described in this subsection. The transformation of the CMS track parameters and their covariance matrix into the ZEUS format is shown here as well.

The five parametes (ϕ_0, Q/R, $Q \cdot D_0$, z_0, $cot(\theta_0)$) at ZEUS have a different meaning in most cases than their corresponding parameters for the CMS experiment. Most parametes are defined at the point of closest approach (PCA) which is the closest point on the track trajectory, from the center of the global coordinate system. The parameters for the ZEUS experiment have the following meaning []:

- ϕ_0 is the angle between the global x-axis in the global coordinate system and the helix momentum at the PCA.
- Q/R represents the ratio of the track charge and the radius of its helix trajectory in the xy-plane
- $Q \cdot D_0$ is the charge of the track multiplied by the projection on the xy-plane of the distance from the center of the global coordinate system to the PCA.
- z_0 is the z-coordinate of the closest distance between the PCA and the center of the global coordinate system.
- $cot(\theta_{dip})$ is the cotangen of the polar angle of the track (Fig. 7.17).

where R is the radius of the helix as already defined for the CMS experiment in Appendix A, and is shown here again to get more complete picture of the transformation process:

$$R = \frac{|p| \cdot sin(\theta)}{0.0029979 \cdot B_z}, \tag{7.7}$$

where B_z is defined in Tesla and R in cm. From the CMS track helix parametrisation (Appendix A) and the parametrisation defined above one can see that the meaning of the parameters is different. Even more, the same parameters such as polar and azimutal angles differ by an $N \cdot \pi$ offset, where N is some number which is very special for the chosen experiment. Those differences will be explained in detail in the following subsections. From the magnetic field orientation arises a connection between the track charge and its trajectory orientation. In the case were $q = 1$ the bend of the track trajectory is anticlockwise. In the case were $q = -1$ the bend of the track is clockwise in the xy plane.
Technically, the five parametes of the ZEUS tracks were taken from the TRK block of the data described in the following. There are three variables which contain all used parameters needed for the track parameter transformation between the two experiments:

- trk_helpar(5,$trk\_ntracks$), a real track's helix parameters (VCTRHL or ZTTRHL) as listed above
- trk_covmat(15,$trk\_ntracks$), a real track's covariance matrix (VCTRHL or ZTTRHL)

- *trk_helmom*(*trk_ntracks*), a real track's momentum (VCTRHL or ZTTRHL) before any vertex fitting.

The first two variables are two-dimentional arrays with 5 and 15 values for the five and 15 parameters of the track parametrization and its covariance matrix. The *trk_helmom* variable is a one-dimentional array which contains the track momentum. The "*trk_ntracks*" parameter is the track iterator. A 5×5 covariance matrix is associated to those parameters giving as diagonal elements the variance of the each parameters.

ZEUS and CMS Helix Parameters Transformation

It should be stated here that all the following transformations are valid for the CMS 2010 data and were not checked carefully for data obtained later by the CMS detector. Since some aspects of the parameterization may be changed one should briefly check the usage of it for the CMS data different from 2010. The data which was used for this study from the ZEUS detector is the data from the common ntuples, v02d.
Table 7.1 shows set of parameters mentioned above for the ZEUS and CMS experiments. To obtain a better understanding of the transformation formulas those parameters are renamed with a simpler notation.

z_1	ϕ_0
z_2	Q/R
z_3	$Q \cdot D_0$
z_4	z_0
z_5	$cot(\theta_0)$

c_1	$q/\|p\|$
c_2	λ
c_3	ϕ
c_4	d_{xy}
c_5	d_{sz}

Table 7.1: The ZEUS (left) and CMS(right) parameters with their symbols in the conversion formulas.

The transformation of the first parameter ϕ from the CMS system (c_3) into the ZEUS system (z_1) is relatively simple, taking into account that the ϕ value for the two experiments is measured in the same way but with different ϕ range. For the ZEUS experiment ϕ is defined in the range (0;2π), while for CMS it is measured in the range ($-\pi$, π). The corresponding transformation is:

$$\begin{aligned} z_1 &= c_3, \text{ for } c_3 \geq 0, \\ z_1 &= 2\pi - |c_3|, \text{ for } c_3 < 0. \end{aligned} \tag{7.8}$$

The parameter z_2 is defined via the helix radius which is not explicitly included in any of the variables for the CMS experiment. Thus the transformation was done by calculating the radius of the helix, using the formula (7.7). A track momentum value in the ZEUS system is extracted from $c_1 = q/|p|$. The z-component of the magnetic field of the CMS experiment, B_z, is extracted directly from the data and is explained in the Appendix A (with using the $ESHandle < MagneticField > magfield$ object).

The value of θ in the CMS experiment is calculated using the parameter c_2, by $\theta = \pi/2 - c_2$, where $c_2 = \lambda$ is defined in the same range for both the ZEUS and CMS experiments. Thus, since the transformation of z_5 is defined as: $z_5 = cot(\theta) = cot(\pi/2 - c_2) = tan(c_2)$.

$$z_5 = tan(c_2) \tag{7.9}$$

Let's define the helix radius with CMS paramters:

$$R = \frac{\sin(\theta) \cdot |p|}{0.0029979 \cdot B_z} = \frac{cos(\lambda) \cdot |p|}{0.0029979 \cdot B_z} \tag{7.10}$$

The transformation of the z_2 parameter with formula (7.10) is defined as:

$$z_2 = \frac{q}{R} = \frac{0.0029979 \cdot B_z \cdot q}{cos(\lambda) \cdot |p|} = \frac{0.0029979 \cdot B_z \cdot c_1}{cos(c_2)} \tag{7.11}$$

The parameter z_3 is defined as:

$$z_3 = c_4 \cdot \frac{c_1}{|c_1|}, \tag{7.12}$$

where $c_1/|c_1| = q$ and $c_4 = d_{xy} = D_0$.
The relationship between the track parameters $z_0 = d_{sz}/cos(\lambda)$ can be seen from the figures (7.17) and (7.15) of the ZEUS and CMS experiments. Thus, the parameter z_4 is defined as:

$$z_4 = \frac{c_5}{cos(c_2)} \tag{7.13}$$

For a better understanding of the covariance matrix transformation the next table will summarize all transformation formulas listed above:

$z_1:$	$z_1 = c_3,$ for $c_3 \geq 0$, $z_1 = 2\pi - \lvert c_3 \rvert,$ for $c_3 < 0$
$z_2:$	$z_2 = (0.0029979 \cdot B_z \cdot c_1)/cos(c_2)$
$z_3:$	$z_3 = (c_4 \cdot c_1)/(\lvert c_1 \rvert)$
$z_4:$	$z_4 = c_5/cos(c_2)$
$z_5:$	$z_5 = tan(c_2)$

The knowledge of the relationship between the parameters $Z = [z_1, z_2, z_3, z_4, z_5]$ and $C = [c_1, c_2, c_3, c_4, c_5]$ allows to determine a Jacobian matrix which in the general case is defined as:

$$\mathbf{J} = \left[\frac{\partial \mathbf{f}}{\partial x_1} \cdots \frac{\partial \mathbf{f}}{\partial x_n} \right] = \begin{bmatrix} \frac{\partial f_1}{\partial x_1} & \cdots & \frac{\partial f_1}{\partial x_n} \\ \vdots & \ddots & \vdots \\ \frac{\partial f_m}{\partial x_1} & \cdots & \frac{\partial f_m}{\partial x_n} \end{bmatrix}. \tag{7.14}$$

Then, the Jacobian conversion matrix of the CMS parameters $\boldsymbol{C}$ into the ZEUS parameters $\boldsymbol{Z}$

is given in the form:

$$J = \begin{bmatrix} 0 & 0 & 1 & 0 & 0 \\ z_2/c_1 & z_2 \cdot z_5 & 0 & 0 & 0 \\ 0 & 0 & 0 & 0 & c_1/|c_1| \\ 0 & z_5 \cdot z_4 & 0 & 0 & \frac{1}{cos(c_2)} \\ 0 & \frac{1}{cos^2(c_2)} & 0 & 0 & 0 \end{bmatrix}. \tag{7.15}$$

With the formula (7.14) one can define the general transformation formula:

$$Z = J \cdot C \cdot J^T. \tag{7.16}$$

Such a definition is also true for the track covariance matrix.

Since the parameterization of the covariance matrix at the ZEUS experiment was not clearly documented, a method of trial was used as well as the knowledge of the relationship between the diagonal and the side elements of the covariance matrix. The $trk\_covmat(15,i)$ array of the each track i at the ZEUS experiment contains a 15-size array with the complete information about the covariance matrix elements. What was not clearly documented is their position. For simplicity the array $trk\_covmat(15,i)$ is shown as $M_{k,i} = trk\_covmat(15,i)$, where k is defined in the range (0,14). The final form of the covariance matrix at the ZEUS experiment which can be obtained directly from the data for the chosen track i and its covariance matrix $M_{k,i}$ is given in the form:

$$Z_i^{cov} = \begin{bmatrix} M_{0,i} & M_{1,i} & M_{2,i} & M_{3,i} & M_{4,i} \\ ... & M_{5,i} & M_{6,i} & M_{7,i} & M_{8,i} \\ ... & ... & M_{9,i} & M_{10,i} & M_{11,i} \\ ... & ... & ... & M_{12,i} & M_{13,i} \\ ... & ... & ... & ... & M_{14,i} \end{bmatrix} \tag{7.17}$$

Where the left bottom part corresponding to the top right part since the covariance matrix is symmetrical.

Calculations checks

While a common data sample for the ZEUS and CMS experiment does not exist, another method to check the transformation formulas had to be developed. The idea of such check is quite simple:

- take a track collection from the CMS data sample and extract the information about the vertex to which they belong,
- transform those tracks into the ZEUS format with using transformation procedure described above,
- after the transformation, fit the track collection into vertex,
- compare the vertex position for both ZEUS and CMS vertices.

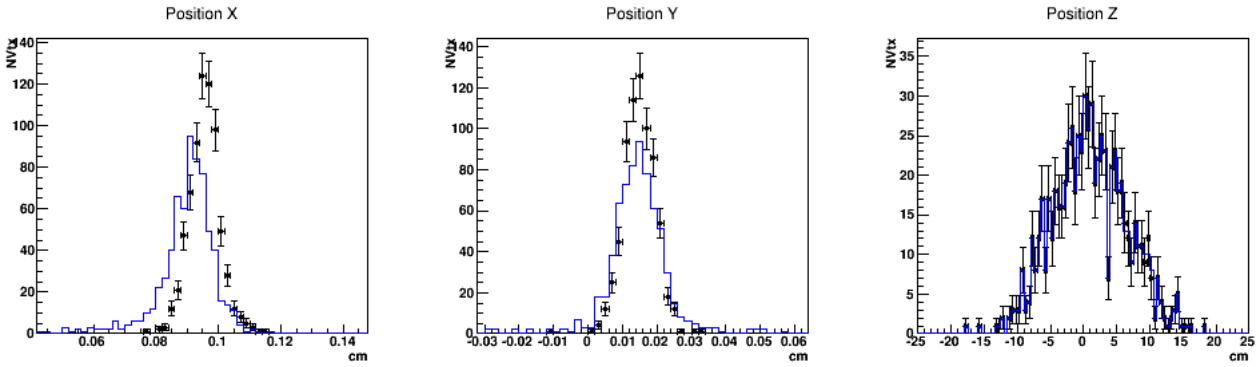

Figure 7.18: The comparison between the vertex information (X, Y, Z position). The comparison is presented the vertices (black points) extracted directly from the CMS data and the vertices parameters fitted by the ZEUS software (blue line).

This check was prepared and results is shown in the figure 7.18. For such comparison the minimum bias data sample (2010) was used. For the ZEUS vertex fit a VxLite [114] package based on the Kalman Filter [106] was used. From the figure 7.18 one can see that the z-coordinate is in very good agreement. This is because the helix transformation of the z paramter is very clear and it is not connected with the other paramteres. Vertices x and y-position has some differences up to a few hundred micrometers. This can be explained with a small differences in the vertex fitter for both experiments as well as possible small mistakes in the transformation procedure. In order to use this study with a better accuracy in future one should does additional checks which can check those two issues.

Summary

This study is done to perform a proper transformation of the track paramters from the CMS into ZEUS formats. Both formats were careful studied and a simple helix parameter transformation has been performed. Then the Jacobian matrix was calculated to perform the transformation for the track parameters and for their covariance matrices. Obtained formulas were used to transform a track collection from the CMS data into ZEUS format which then were fitted into the vertex with the ZEUS fitter "VxLite". The obtained vertex position parameters were compared with the corresponding vertices extracted from the CMS data. Both vertex fitters did not use a beam spot constraint. The result shows excellent agreement of the z-coordinate of the vertices, while the x- and y-coordinates have differences up to a few hundred micrometers. This might be explained that different fitters where used for the vertex fit or with some misunderstanding in the CMS or ZEUS track parameterization formats.

In terms of future possible data combination from different world experiments this study can be very useful as it explains the general transformation procedure step by step as well as it gives the transformation example of the CMS into the ZEUS track parameters.

Appendix C: CMS Open Data Validation

CMS Open Data are available in the same format as used in analysis by CMS physicists. A CMS-specific analysis framework is needed, and it is provided as a Virtual Machine image with the CMS analysis environment. The data can be accessed directly through the VM image [119].

The CMS Open Data were successfully validated by reconstructing dimuon events produced by quarkonium decays. The results were compared to similar results published by the CMS Collaboration [130]. The project includes the reconstruction of $D^{*\pm}$ and D^0 mesons.

The main ZEUS research for this analysis, described in sections 4-7, based on the previous analysis and was not started from the beginning. In turn, the B+ study is performed from the very beginning but was not finished. From the logical point of view, both studies may be combined and complement each other, although they were made on various experiments and with different data.

The data set used for this study is part of a "Minimum Bias" and "Muon" data sample which was released by CMS experiment as CMS Open Data. The total number of events is 16 million which were used for this analysis. J/ψ mesons were reconstructed via their decay channel $J/\psi \to \mu^+\mu^-$ (Fig. 7.19).

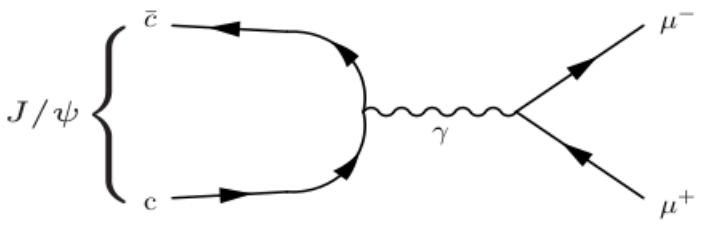

Figure 7.19: Feynmann diagram whith the dacay channel of J/ψ. The image is taken from [130].

J/ψ, B^+ Reconstruction

The goal of this study is the reconstruction of B mesons in the channel $B^+ \to J/\psi K^+$. The J/ψ reconstruction is partially based on the results obtained from the previous dimuon research [131, 130]. To isolate the $J/\psi \to \mu^+\mu^-$ decay channel, the selection criteria from the CMS

paper [134] were used. The probability of such a decay channel is $(5.96 \pm 0.03)\%$ [133]. Each muon candidate passed a transverse momentum cut which depends on the pseudorapidity: $P_T > 3.3\ GeV/c$ for $|\eta^\mu| < 1.3$, $P > 2.9\ GeV/c$ for $1.3 < |\eta^\mu| < 2.2$, and $P_T > 0.8\ GeV/c$ for $2.2 < |\eta^\mu| < 2.4$. The J/ψ candidate mass was chosen between 2.6 and 3.5 GeV/c^2, while its rapidity range is $|y| < 2.4$. The general rapidity definition is $y = \frac{1}{2} ln \frac{E+P_{||}}{E-P_{||}}$, where E is the J/ψ energy in this case and $P_{||}$ the momentum part parallel to the z-axis. For each di-muon candidate an adaptive vertex fitter [135] was used to check if they are coming from the same vertex. In addition, each muon's track has to pass a χ^2 requirement, $\chi^2_{trackfit} < 4$.

The adaptive vertex fitter uses track parameters as an input. In the analysis the global muon collection was used. To make a proper use of the fitter one should make an excelent technical conformity between the track and muon candidate. In this study such conformity was significantly improved which created the opportunity to do a better fit, and in turn - reduce the number of muon candidates which were rejected because they did not come from the same vertex. In turn this improvement increased the number of J/ψ candidates (Fig. 7.20).

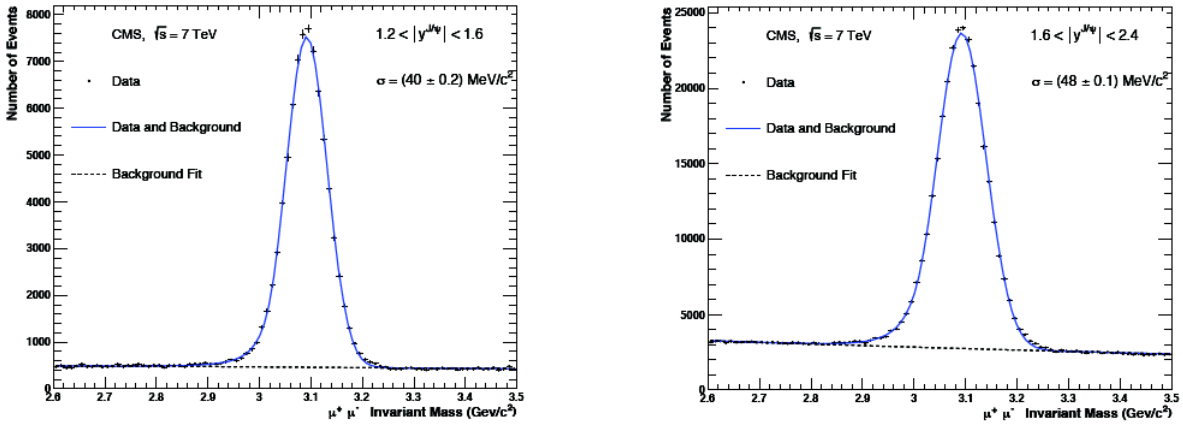

(a) (b)

Figure 7.20: Dimuon invariant mass distribution in two rapidity ranges $1.2 < |y^{J/\psi}| < 1.6$ (a) and $1.6 < |y^{J/\psi}| < 2.4$ (b). Fitted with Crystal Ball functions and an exponential (b) or polynomial (a) background. The tool to get those plots were obtained from [130].

In this study decays of the B^+ meson were reconstructed through the combination of a J/ψ meson and a kaon, K^+. For the kaon an additional requirement is applied. The decay channel studied was: $B^+ \to J/\psi K^+$ with a probability to decay of 0.1 % [132]. Figure 7.21 shows B^+ invariant distribution. For the B-meson selection the J/ψ mass window was restricted to the range (2.95 and 3.25) GeV/c^2. The B^+ meson candidate a mass range cut is (4.8, 5.7) GeV/c^2. In addition kinematic cuts for the B^+ mesons were used: $P_T > 5\ GeV/c$ and $|y| < 2.4$.
It should come from the same vertex as the J/ψ candidate or not originate from any vertex at all. This was checked by using the adaptive vertex fitter which can make the decision if the chosen track collection comes from the same vertex.

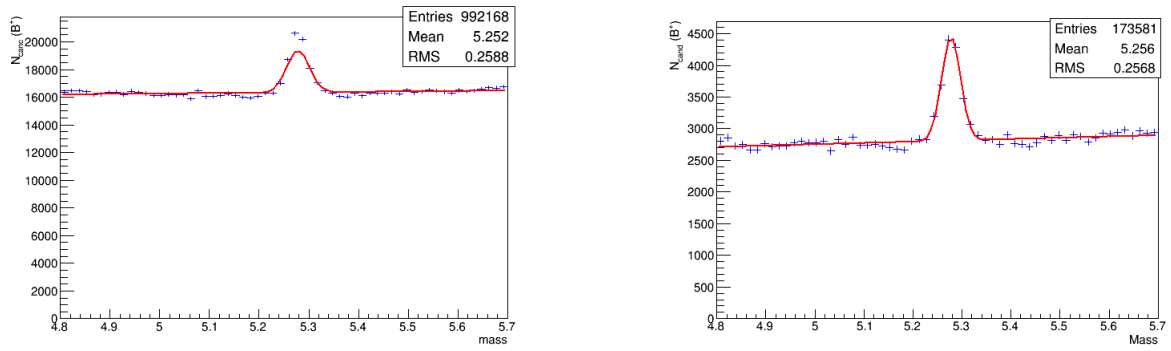

(a) (b)

Figure 7.21: Invariant mass distribution of B^+ candidates. The left distribution shows the invariant mass without decay length cut, and with cut on decay length > 0.1 mm, plot (b).

Decay Length Calculations

The decay length was calculated using the covariance matrices of the primary and secondary vertex candidates. This is done with respect to the beam spot constrained primary vertex position. Another way is the decay length reconstruction via the beam spot position. This way should include a correction of the beam slope. The decay length was calculated with formulas 3.16. Figure 7.22 shows the decay length distribution of the B candidates.

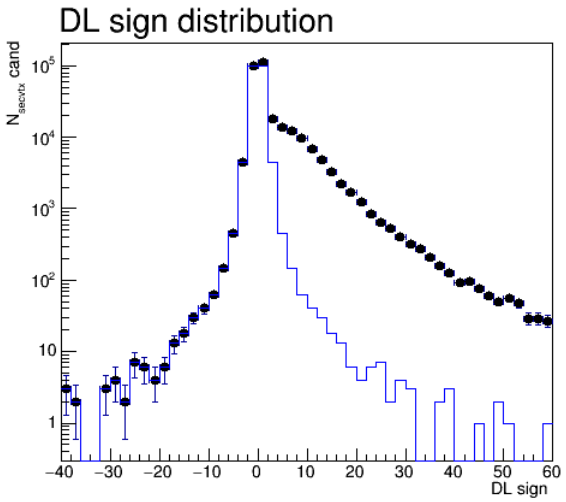

Figure 7.22: The decay length distribution of the B candidates. The distributions shows the B decay distribution which was used to clean the B signal.

Additional tools

CMS is a particle detector that is designed to register high-energy collisions in the LHC. Figure 7.23 shows a visual representation of the event with a collection of tracks. The CMS visualization tool is a very powerful software package that allows to get a better understanding about the event structure and makes it easy to check out some simple assumptions.

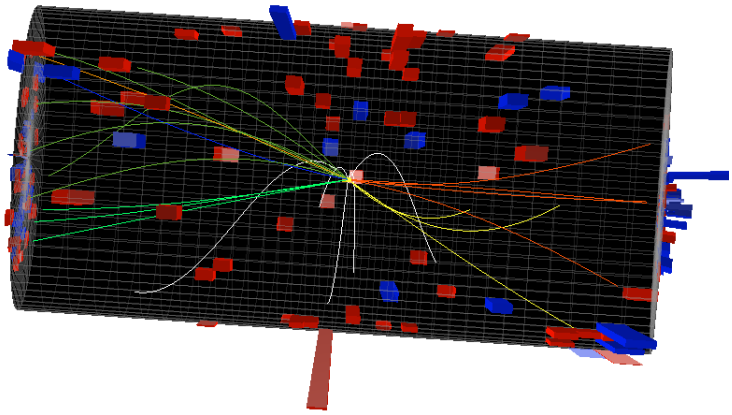

(a)

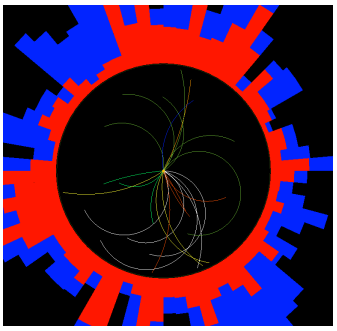

(b)

Figure 7.23: The CMS detector sketch with track collection example. The detector is shown in the $y - z$ plane (a) and the $x - y$ plane (b).

Such visual interpretation is accompanied with the information about the each single track, vertex, jet candidate and the interaction point. It contains the information about each particle's energy, particle identification, momentum and other useful information. This tool was used many times during the CMS studies described in this thesis.

Appendix D

Instantons

Instantons [136] or instanton-induced events are a source for non-isolated, both like- and unlike-sign muon pairs. In *ep* collisions instantons are produced mainly in boson-gluon fusion. Figure 7.24 shows a QCD instanton-induced event where photon fluctuates into a $q\bar{q}$ pair. One of the quarks interact then with a gluon and create instanton-induced event. An experimemtal sign of

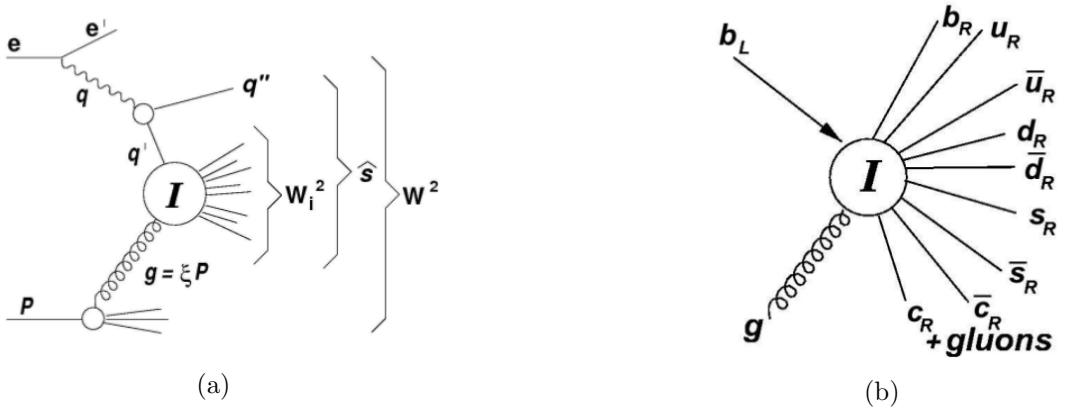

(a) (b)

Figure 7.24: QCD instanton-induced events production diagram.

instanton-induced events at HERA may be determined using event shape variables. There are the virtuality of the quark creating the instanton, the instanton band, which is the area in the $\eta - \phi$ plane in which the particles obtained after the instanton decay, sphericity and isotropy. A detailed description of these variables may be found at [99].

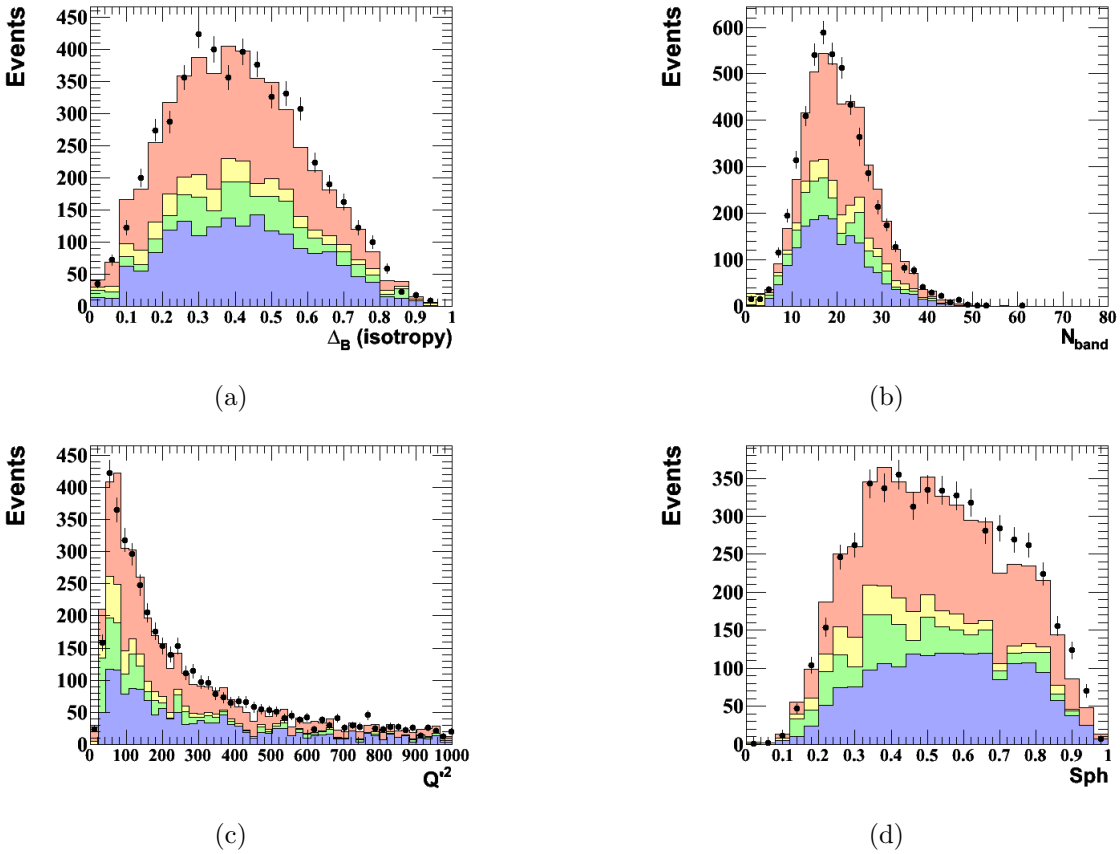

Figure 7.25: The isotropy(a), instanton band(b), quark virtuality(c) and sphericity(d) without instanton events included.

In this analysis an attempt to indicate the presence of instanton-induced events was made using insanton variables calculated from the instanton Monte Carlo HERWIG sample.
Figure 7.26 shows with different colors charm, beauty quarkonia contributions. The is indicated with the black dots. The gray area shows the instanton contribution. The shape of the instanton contribution was extracted from the HERWIG MC. The normalisation (0.5 x QCDINS) was obtained from the previous analysis [99].
An indication for the instanton-induced events would be the different shape of the distributions shown on Fig. 7.26. In such case these variables can be used for the separation of the instanton events from the beauty sample. As it is visible from the figure, the shape of instanton distribution is similar to the data and beauty contribution. During this analysis an essential bug of the previous MC simulation was found. Fixing it and further reconstruction of the shape variables shows that there is no indication for instanton-induced events in the data. Figure 7.26 shows the results after the bug fix.

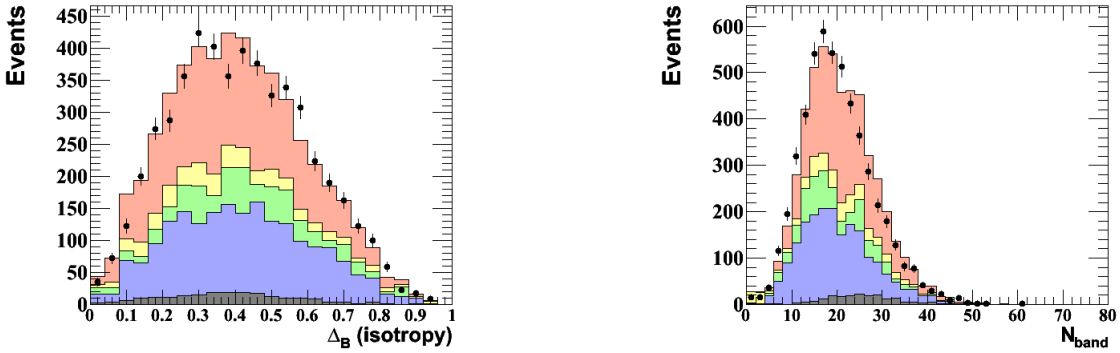

(a) (b)

(c) (d)

Figure 7.26: The isotropy(a), instanton band(b), quark virtuality(c) and sphericity(d) variables with instanton events included.

Definition of the bin contents of Fig. 3.2

x-axis number	**Finder**	**Description**
4 = quality 4		
4.2	BREMAT	inner chambers
4.4	BAC	
4.5	BAC/BREMAT + MV	not vertex assosiated or low quality muon
4.6	MPMATCH or MUFO	low probability that is mutched with track
4.7	MUFO	assosited tracks not found
5 = quality 5		
5.1	BREMAT + MV	outer chambers low probability (BREMAT)
5.2	BREMAT + MV	inner chambers (BREMAT), $\|\eta^\mu\| > 0.6$ (MV)
5.4	BAC + MV	$\|\eta^\mu\| > 0.6$
5.5	BREMAT + BAC + MV	inner chambers (BREMAT), $\|\eta^\mu\| < 0.6$ (MV)
5.6	MPMATCH/MUFO	lower quality forward muon
6 = quality 6		
6.1	BREMAT + MV	outer chambers
6.6	MPMATCH or MUFO	with tracks
6.8	MPMATCH/MUFO + MV	lower probability (MPMATCH/MUFO)
7 = quality 7		
7.2	quality 4 & 4	
7.3	quality 5 & 4	
7.4	quality 6 & 4 or quality 5 & 5	
7.5	quality 6 & 5	
7.6	quality 6 & 6	
7.7	muon chambers only	MPMATCH, MUFO or BREMAT
7.8	BAC only & 4	

Table 7.2: μ finder key bin meaning[99].

List of Figures

List of Tables

Bibliography

[1] Herb, S. W., et al. "Observation of a Dimuon Resonance at 9.5 GeV in 400-GeV Proton-Nucleus Collisions", Phys. Rev. Lett. 39 (Aug, 1977) 252255.

Chapter 1

[2] M. Gell-Mann, "A Schematic Model of Baryons and Meson", Phys.Lett. 8 (1964) 214215.

[3] "Standard Model: An Introduction". S. F. Novaes (Instituto de Fisica Teorica, UNESP), 27 Jan 2000. arXiv:hep-ph/0001283.

[4] "Handbook of Perturbative QCD." April 1993, CTEQ Collaboration, Rev.Mod.Phys. 67 (1995) 157-248.

[5] Donald H. Perkins, "Introduction to High Energy Physics". ISBN-13: 978-0521621960.

[6] A link to the SM particles table image:
"$https://en.wikipedia.org/wiki/File:Standard\_Model\_of\_Elementary\_Particles.svg$"

[7] CMS Collaboration. "Measurement of the inclusive 3-jet production differential cross section in proton-proton collisions at 7 TeV and determination of the strong coupling constant in the TeV range", The CMS Collaboration. arXiv:1412.1633.

[8] F. Halzen, A. D. Martin, "Quarks and Leptons: Introductory Course in Modern Particle Physics", John Wiley and Sons, 1984.

[9] C.G. Callan, Curtis G., Jr., Gross, David J., "High-energy electroproduction and the constitution of the electric current." Phys. Rev. Lett. 22 , 156 (1969).

[10] A. M. Cooper-Sarkar, R. Devenish, A. De Roeck, "Structure functions of the nucleon and their interpretation", Int. J. Mod. Phys. A 20, (1998) 3385.

[11] H1 and ZEUS Collaboration, "Compiled H1+ZEUS NC and CC plots for conferences", ZEUS-prel-09-001, H1prelim-09-043 (2009).

[12] J. C. Collins, D. E. Soper "The Theorems of Perturbative QCD", Ann. Rev. Nucl. Part. Sci. 37, (1987) 383.

[13] C. Patrignani et al. (Particle Data Group), Chin. Phys. C, 40, 100001 (2016). Cut-off date for this update was January 15, 2016.

[14] M. Kobayashi and T. Maskawa, Prog. Theor. Phys. 49, 652 (1973).

[15] L. Jones, H. Wyld, "Charmed-particle production by photon-gluon-fusion", Phys. Rev. D17, (1978) 759.

[16] E. Fermi, Z. Phys. 29, (1924) 315; V. M. Budnev et al., Phys. Rep. C 15, (1975) 181.

[17] C. F. von Weizsäcker, Z. Phys. 88 ,(1934) 612; E.J. Williams, Phys. Rev. 45, (1934) 729.

[18] Abramowicz, H., Abt, I., Adamczyk, L. et al. , "Combination of measurements of inclusive deep inelastic $e^{\pm}$ p scattering cross sections and QCD analysis of HERA data", Eur. Phys. J. C (2015) 75: 580.

[19] D.J. Gross; F. Wilczek (1973). "Ultraviolet behavior of non-abelian gauge theories". Physical Review Letters. 30 (26): 13431346. Bibcode:1973PhRvL..30.1343G. doi:10.1103/PhysRevLett.30.1343

[20] J.C. Collins, D.E. Soper, "The Theorems Of Perturbative QCD". Annual Review of Nuclear and Particle Science Volume 37, 1987 Collins, pp 383-409. DOI: 10.1146/annurev.ns.37.120187.002123

[21] V. N. Gribov, L. N. Lipatov, Sov. J. Nucl. Phys 15, (1972) 438.
G. Altarelli, G. Parisi, Nucl. Phys. B 126, (1977) 298.
Y. L. Dokshitzer, Sov. Phys. JETP 46, (1977) 641.

[22] M.L. Mangano, "Two lectures on heavy quark production in hadronic collisions". arXiv:hep-ph/9711337v1, 14 Nov 1997.

[23] "HERA Physics Feynman Diagram Gallery - Desy" http://www.desy.de/∼gbrandt/feyn/

[24] R. Keith Ellis. "Quantum Chromodynamics and Deep Inelastic Scattering", Adv.Ser.Direct.High Energy Phys. 26 2016 61-78, DOI: 10.1142/9789814733519_0003, 2016.

[25] CMS Collaboration, "The Electromagnetic Calorimeter Technical Design Report", CERN/LHCC **97-033** (1997). CMS TDR 4, Addendum CERN/LHCC 2002-027.

[26] The CMS home page. Detector overview.
Site located at http://cms.web.cern.ch/news/detector-overview .

[27] The CMS Collaboration. "Alignment of the CMS tracker with LHC and cosmic ray data". CMS-TRK-11-002. CERN-PH-EP/2013-037.

[28] The CMS home page. Tracker detector overview.
Site located at http://cms.web.cern.ch/news/tracker-detector .

[29] Joerg Behr (on behalf of the CMS Collaboration). Alignment procedures for the CMS silicon tracker. 2012 J. Phys.: Conf. Ser. 396 022005

[30] "Alignment of the CMS silicon Tracker using Millepede II". Journal of Physics: Conference Series 120 (2008) 032040

[31] V. Blobel, "Software alignment for tracking detectors", Nucl. Instrum. Meth. A 566 (2006) 5, doi:10.1016/j.nima.2006.05.157.

Also with the link: *https* : *//www.wiki.terascale.de/index.php/MillepedeII*.

[32] M. J. French et al., "Design and results from the APV25, a deep sub-micron CMOS front-end chip for the CMS tracker", Nucl. Instrum. Meth. A 466 (2001) 359

[33] Image source: *https* : *//en.wikipedia.org/wiki/Particle_physics*

[34] "Neutrino mass limits: robust information from the power spectrum of galaxy surveys." Antonio J. Cuesta, Viviana Niro, Licia Verde, arXiv:1511.05983

[35] "Measurement of DIS cross section at HERA", Sasha Glazov, for the H1 Collaboration, Braz. J. Phys. vol.37 no.2c Sao Paulo June 2007

[36] Diagram of an LHC dipole magnet, CERN-DI-9906025

[37] http://www.lhc-closer.es/taking_a_closer_look_at_lhc0.lhc_layout

[38] https://home.cern/about/accelerators

[39] https://pythia6.hepforge.org/

[40] https://rapgap.hepforge.org/

[41] A. Geiser, A. E. Nuncio Quiroz, "The FMNR ⊗ PYTHIA interface for Heavy Quark Production at HERA", ZEUS-NOTE 06-012 (2006)arXiv:0707.1632v1.

[42] B. Anderson et al., "Parton fragmentation and string dynamics", Physics Reports 97, (1983).

[43] Link to the main webpage: "http://petraiii.desy.de"

[44] Link to the main webpage: "http://www.desy.de/forschung/anlagen__projekte/hera/index_ger.html"

[45] Link to the main webpage: "https://flash.desy.de"

[46] Link to the main webpage: "http://www.xfel.eu"

[47] J. Andruszkow et al., Acta Phys. Polon. B 32:2025 (2001).

Chapter 2

[48] DESY web page. Image link : http://www.desy.de/~pol2000/pics/hera/hera_2002.gif

[49] DESY web page. Image link : http://www.hamburg.de/image/
/1389340/4x3/690/518/33ef6005605f54e6176d02e2e0e50c2/Vv/desy-1.jpg

[50] DESY HERMES web page. Link: http://www-hermes.desy.de/.

[51] DESY ZEUS web page. Link: https://www-zeus.desy.de/.

[52] DESY H1 web page. Link: http://h1.desy.de/.

[53] DESY HERA-B web page. Link: http://www-hera-b.desy.de/.

[54] B. Foster et al., "The design and construction of the ZEUS central tracking detector", Nucl.Instrum.Meth. A338 (1994) 254283, doi: 10.1016/0168-9002(94)91313-7.

[55] Derrick, M. et al., "Design and construction of the ZEUS barrel calorimeter", Nucl. Instrum. Meth. A309 (1991), p. 77-100.

[56] ZEUS Calorimeter Group and ZEUS Collaborations (Andresen, A. et al.), "Construction and beam test of the ZEUS forward and rear calorimeter", Nucl. Instrum. Meth. A309 (1991), p. 101-142.

[57] I.-M. Gregor, DESY, Germany for the ZEUS Calorimeter Group, "The ZEUS Uranium Calorimeter - 15 Years of Successful Operation", 2007 IEEE Nuclear Science Symposium Conference Record N13.

[58] ZEUS Coll., "The ZEUS Detector. Status Report", tech. rep., 1993, link : http://www-zeus.desy.de/bluebook/bluebook.html.

[59] E. Acerbi et al., "Thin and compensating solenoids for ZEUS detector" In "Boston 1987, Proceedings, Magnet technology" 13541357, 1987).

[60] "The ZEUS detector web page". Link : http://www-zeus.desy.de/public/zeus.php3.

[61] G. Abbiendi et al. The ZEUS barrel and rear muon detector. Nucl. Instrum. Meth., A333:342, 1993.

[62] Forward Muon Detector,
ZEUS web page link: http://www-zeus.desy.de/bluebook/ch09/chapter2_4.html

[63] Barrel and Rear Muon Detector,
ZEUS web page link: http://www-zeus.desy.de/bluebook/ch10/chapter2_4.html

[64] B. Foster, "ZEUS at HERA II." 24 Jul 2001, arXiv:hep-ex/0107066.

[65] Link to the lumi page: "http://www-zeus.desy.de/physics/lumi/"

[66] David Bailey, Richard Hall-Wilton, "Experience with the ZEUS central tracking detector". DOI: 10.1109/NSSMIC.2004.1462364

[67] David Bailey, Richard Hall-Wilton, "R. Hall-Wilton et al., "The CTD Tracking Resolution" (unpublished). ZEUS-99-024, 1999.".

[68] Jean-Luc Caron. "LHC Layout. Schema general du LHC.AC Collection. Legacy of AC. Pictures from 1992 to 2002". The link: https://cds.cern.ch/.

[69] L. Evans and P.Bryant. "LHC Machine". Journal of Instrumentation, 3(08):S08001, 2008.

[70] W. Smith et al., "The ZEUS calorimeter first level trigger", Nucl.Instrum.Meth. A355 (1995) 278294.

[71] A. Quadt et al., "The design and performance of the ZEUS central tracking detector second level trigger", Nucl.Instrum.Meth. A438 (1999) 472501.

[72] S. Bhadra et al., "The ZEUS third level trigger system", Comput.Phys.Commun. 57 (1989) 321324.

[73] An official CMS webpage link: *http://cms.web.cern.ch/news/cms-detector- design.*

[74] The ALICE experiment official webpage link: *http://aliceinfo.cern.ch/Public/Welcome.html.*

[75] The ATLAS experiment official webpage link: *https://atlas.web.cern.ch/Atlas/Collaboration/.*

[76] The CMS experiment official webpage link: *http://cms.web.cern.ch/.*

[77] The LHCb experiment official webpage link: *http://lhcb.web.cern.ch/lhcb/.*

[78] V. Veszpremi, "Operation and performance of the CMS tracker."

[79] CMS Collaboration, "The CMS experiment at the CERN LHC.", 2008, JINST 3 S08004.

[80] CMS Collaboration, "The CMS experiment at the CERN LHC.", 2008, JINST 3 S08004, Chapter 3.1.3.

[81] The CMS Collaboration. "Energy calibration and resolution of the CMS electromagnetic calorimeter in pp collisions at 7 TeV", JINST, 8:P09009, 2013.52.

[82] CMS Collaboration, "The Electromagnetic Calorimeter Technical Design Report", 1997, CERN/LHCC 9733.

[83] CMS Collaboration, "The CMS hadron calorimeter project: Technical Design Report". Technical Design Report CMS. CERN, Geneva, 1997. CERN-LHCC-97-031.

[84] CMS Collaboration, "Performance of CMS Hadron Calorimeter Timing and Synchronization using Test Beam, Cosmic Ray, and LHC Beam Data". JINST, 5:T03013, 2010.

[85] CMS Collaboration, "The CMS barrel calorimeter response to particle beams from 2 to 350 GeV/c", Eur. Phys.J.C (2009).

[86] CMS Collaboration, "Muon Technical Design Report", 1997, CERN/LHC 97-32.

[87] CMS Collaboration, "CMS Physics: Technical Design Report Volume 1: Detector Performance and Software". (2006).

[88] CMS Collaboration, "CMS The TriDAS Project Technical Design Report, Volume 2: Data Acquisition and High-Level Trigger". Technical Design Report CMS. CERN, Geneva, 2002.

Chapter 3

[89] Common Ntuple format. The link to the corresponding page: "*https://wwwzeus.mpp.mpg.de/dphep_cn.html*"

[90] ORANGE web page. Link to the corresponding page: "*http://www-zeus.desy.de/ZEUS_ONLY/analysis/orange/index.html*"

[91] "http://www-zeus.desy.de/ZEUS_ONLY/analysis/orange/release.notes/orange_ntuple.v2012a.1.html#SECVTX"

[92] https://herwig.hepforge.org/

[93] B. List (CERN) , A. Mastroberardino (Calabria U.). "DIFFVM: A Monte Carlo generator for diffractive processes in ep scattering." Conf. Proc. C980427 (1998) 396-404. The link: http://inspirehep.net/record/486059

[94] Tetsuo Abe. "A Generator for Dilepton Production in ep Collisions", GRAPE-Dilepton (version1.1), arXiv:hep-ph/0012029

[95] www.desy.de/ golubkov/Formoza/formoza/doc/

[96] H. Abramowicz, A. Caldwell and R. Sinkus, "Neural network based electron identification in the ZEUS calorimeter", Nucl. Instr. Meth. A 365, (1995) 508.
R. Sinkus and T. Voss, "Particle identification with neural networks using a rotational invariant moment representation", Nucl. Instr. Meth. A 391, (1997) 360.

[97] P. Billoir and S. Qian, "Fast vertex fitting with a local parametrization of tracks.", Nucl. Inst. Meth. A 311, 139 (1992).

[98] G.F. Hartner and C. Catterall. ZEUS-Note 12-001 "VCTRAK for HERA II".

Chapter 4

[99] D. Bot, "Measurement of beauty quark production from dimuon events with the ZEUS detector at HERA II", DESY-THESIS-2011-032.

[100] M. Klein, "Physics at HERA", edited by W. Buchmüller and G. Ingelmann, vol. 1, (1991) 71, DESY (Hamburg).

[101] Halina Abramowicz, Allen Caldwell, "HERA Collider Physics", February 7, 2008, hep-ex/9903037 , arXiv.org.

[102] David M. South and Monica Turcato, "Review of Searches for Rare Processes and Physics Beyond the Standard Model at HERA" 1605.03459v1, 11 May 2016.

[103] F. Jacquet, A. Blondel, "Proceedings of the Study of an ep facility for Europe", Ed. U. Amaldi, DESY 79/48, 391.

[104] Alexander Spiridonov, "Mathematical Framework for Fast and Rigorous Track Fit for the ZEUS Detector". DESY 08-182, December 2008.

[105] N. Tuning, "ZUFOs: Hadronic final state reconstruction with calorimeter, tracking and backsplash correction, ZEUS Internal Note ZEUS-IN-01-021"

[106] "An introduction to the kalman filter", 2007.
Link: "http://www.cs.unc.edu/sim welch/kalman/".

[107] E. Maddox. "A kalman filter track fit for the zeus microvertex detector". ZEUS-03-008, 2003.

[108] R. Früwirth, A. Strandli, "Track fitting with ambiguities and noise: a study of elastic tracking and nonlinear filters", Comp. Phys. Comm. 120, 197 (1999).

[109] A. Geiser. "GMUON - a general ZEUS muon finder", DESY Hamburg, December 28, 2006. ZEUS-06-016.

[110] I. Rubinskiy, "Measurement of the meson production cross section in ep scattering at HERA", Ph.D. Thesis, DESY-THESIS-09-014.

[111] M. Corradi, M. Turcato. "Beauty production in dijet events". ZEUS-NOTE-04-005, 2004.

[112] S. Catani, Y. L. Dokshitzer and B. R. Webber, Phys. Lett. B 285, (1992) 291.

[113] Vincent Roberfroid, "*Improvement of the Kalman Filter Fit of the ZEUS experiment*", January 19, 2014.

[114] A link to the package location:
"*http://www-zeus-data.desy.de/relnotes/release-notes.v2007a.1.html*"

Chapter 5

[115] ZEUS Collaboration, S. Chekanov et al., "Measuremants of inelastic J/ψ and ψ' photoproduction at HERA", Eur. Phys. J C 27, (2003) 173.

Chapter 6

[116] ZEUS Collaboration, S. Chekanov et al., "Measurement of beauty production from dimuon events at HERA", JHEP 02, (2009) 32.

[117] I. Bloch, "Measurement of Beauty Production from Dimuon events at HERA/ZEUS", Ph.D. Thesis, Hamburg University (2005), DESY-THESIS-05-034.

[118] LHCb collaboration, "Measurement of the $B_0 - \bar{B}_0$ oscillation frequency Δm_d with the decays $B^0 \to D^- \pi^+$ and $B^0 \to J/\Psi K^{*0}$ ". Phys.Lett. B719 (2013), pp. 318-325, arXiv:1210.6750

Appendix:

[119] A Open Data official webpage link: *http://opendata.cern.ch/research/CMS.*

[120] Many thanks to my wife Darina, that she has found a lot of information and helped me to understand the problem.

https://cmssdt.cern.ch/SDT/doxygen/CMSSW_4_2_8/doc/html/d8/df2/classreco_1_1TrackBase.html

[121] A library is the "TrackBase.h" file from the CMSSW software.
https://twiki.cern.ch/twiki/bin/view/CMSPublic/SWGuideTransientTracks

[122] Introduction to Helical Track Manipulations. *JLC Physics Group. KEK, Tsukuba 305, Japan. June, 1997.*

[123] CMS documentation from the Fermi National Laboratory.
http://cmslxr.fnal.gov/lxr/source/DataFormats/TrackReco/interface/TrackBase.h

[124] John R. Smith, Milan Nikolic, Richard L. Lander, S. Mani Tripathi. "Geometrical Discriminant for H (4l) Searches". University of California. CMS AN-2010/227. 2010.

[125] A library is the "TrajectoryStateClosestToPoint.h" file from the CMSSW software. The link is: *https://cmssdt.cern.ch/SDT/doxygen/CMSSW_4_2_8/doc/html/d3/dd3/classTrajectoryStateClosestToPoint.html*

[126] K. Nakamura et al. (Particle Data Group), "The Review of Particle Physics", J. Phys. G 37, (2010) 075021

[127] TWiki CMS page, *https://twiki.cern.ch/twiki/bin/view/CMS/TkAl1507.*

[128] TWiki CMS page, *https://twiki.cern.ch/twiki/bin/view/CMS/TkAl1507* , results are prepared by Claus Kleinwort.

[129] The official CMS experiment web page link. The CMS detector design: http://cms.web.cern.ch/news/cms-detector-design

[130] Bridget J. Sheeran. "Validation of CMS open data in dimuon systems and first results from $D^{*\pm}$ reconstruction." DESY summer student report. September 8, 2015.

[131] Irene Dutta. "DESY spring student 2015."

[132] $B^{\pm}$ decays. PDG page with link http://pdg.lbl.gov/2015/listings/rpp2015-list-B-plus-minus.pdf.

[133] K.A. Olive et al. (Particle Data Group), Chin. Phys. C, 38, 090001 (2014).

[134] CMS Collaboration. "Prompt and non-prompt J/ψ production in pp collisions at $\sqrt{s} = 7$ TeV". arXiv:1011.4193.

[135] R. Frühwirth, Wolfgang Waltenberger, Pascal Vanlaer. "Adaptive Vertex Fitting". CMS-NOTE-2007-008.

[136] M. Gibbs, A. Ringwald, F. Schrempp. "QCD-Instanton Induced Final States in Deep Inelastic Scattering." DESY 95-119, hep-ph/9506392.

[137] A minimum bias data tag:
"Cosmic70DR-TkAlCosmics0T-Peak_Pess_COSM70_PEA_V1-v1_0T_50ns_ALCARECO".
A isolated muons data tag:
"WJetsToLNu_13TeV-madgraph-pythia8-tauola_Phys14DR-TkAlMuonIsolated-PU20bx25_PHYS14_25_V1-v1_ALCARECO".
A cosmic data tag:
"Cosmic70DR-TkAlCosmics0T-Peak_Pess_COSM70_PEA_V1-v1_0and3.8T_50ns_ALCARECO".

Acknowledgements

I would like to thank all the people which have supported me during my PhD studies.

First of all I would like to thank PD Dr. Achim Geiser for his active participation and support throughout the writing of this thesis. I also want to say thank for the interesting discussion, obtaining extensive knowledge in the field of study and important clear advices. Your ideas and suggestions were always helpful and wise. Thank you for the opportunity to participate in many interesting projects.

As a part of my PhD project, I was working with the CMS tracker alignment group. I would like to thank all of you for the warm reception, interesting and productive work. In the context of the work with the CMS tracker alignment group I would also like to thank Dr. Matthias Schröder for the excellent organization of the technical team and for the opportunity to to get interesting and extensive advices.

With special affection I would like to thank my wife for exceptional support and assistance every day. Your support always helping me to turn difficult problems into the easy and find the strength to deal with them.

Many thanks for Dr. Volodymyr Aushev for the opportunity to join the ZEUS experiment. I thank all my friends for a pleasant pastime and interesting discussions.
A special acknowledgement goes to my family for the great support.

Eidesstattliche Versicherung

Hiermit erkläre ich an Eides statt, dass ich die vorliegende Dissertationsschrift selbst verfasst und keine anderen als die angegebenen Quellen und Hilfsmittel benutzt habe.

Declaration on oath

I hereby declare, on oath, that I have written the present dissertation by my own and have not used other than the acknowledged resources and aids.

Hamburg,